

DISS. ETH NO. 25584

TOWARDS EQUANT SHAPED AND
MONODISPERSED CRYSTALS - COMBINING
TEMPERATURE CYCLES AND MECHANICAL
ACTION

A dissertation submitted to attain the degree of
DOCTOR OF SCIENCES of ETH ZURICH
(Dr. sc. ETH Zurich)

presented by

FABIO SALVATORI
Chem. Eng., Politecnico di Milano

born on January 5th, 1989
citizen of Italy

accepted on the recommendation of

Prof. Dr. Marco Mazzotti (ETH Zurich), examiner
Prof. Dr. Konrad Hungerbühler (ETH Zurich), co-examiner
Prof. Dr. Zoltan Nagy (Purdue University), co-examiner

2018

Fabio Salvatori: *Towards equant shaped and monodispersed crystals - Combining temperature cycles and mechanical action*, © 2018

DOI: -

ABSTRACT

Crystallization from solution is a ubiquitous process in a wide variety of industrial fields, ranging from oil refining to the production of active pharmaceutical ingredients. Particularly in the latter case, the size and shape of the crystals produced strongly impacts all the downstream processes that lead to the production of the commercially available tablet and its effect on human body.

Therefore, it does not come as a surprise the large effort put into developing solutions that can be applied to selectively manipulate the habit and size of the particles crystallized. The main goal of this work has been the development and assessment of a new process, named the *3-stage process*, consisting of a cyclic combination of crystallization, milling, and dissolution steps, to obtain high fraction of equant shaped crystals.

The results presented in this work deal with all the aspects required for a comprehensive design and characterization of a new process, namely the measurement tools specifically designed to characterize the product properties of interest, the experimental characterization and mathematical modeling of the physical phenomena underlying the single step operations and the whole process, and the development of a strategy for the efficient investigation of process feasibility under the constraints of limited amount of information on compound properties available and reduced extent of the experimental campaign. It has been shown that:

- a new stereoscopic opto-imaging setup for the accurate reconstruction of particle morphology and the quantitative estimation of their characteristic dimensions could be used for the comprehensive experimental characterization of a continuous rotor-stator wet milling stage and for the estimation of the kinetic parameters of its characteristic mathematical model.
- a mathematical model for the 3-stage process, considering the plethora of phenomena occurring from the single crystal to the process scale and implementing physically-sound model parameters, could be used for a first in-silico assessment of process feasibility and performance,

highlighting how it could (in principle) be possible to produce crystals with the desired specifications in terms of size and shape.

- through an extensive experimental characterization of the 3-stage process, carried out according to the results obtained with the mathematical model, it was possible to confirm the feasibility of the proposed technology, showing however the strong dependence of the outcome on compound specific properties.
- mathematical models, capable of capturing the fundamental physical phenomena, can be used for the identification of characteristic process trends and can act as a guideline for process design and development.
- it is possible to identify a set of four experiments which is the cardinal core of tests required to gain a first approximation of all the possible process outcome, providing also enough information for the estimation of the kinetic parameters of the model for the 3-stage process.

The work reported in this thesis constitutes a thorough and comprehensive analysis of the 3-stage process considering the effect of process variables and compound properties on the final products, as well as the advantages and disadvantages of the implementation of the proposed technology over more traditional alternatives, along with the possible approaches for successful process design.

SOMMARIO

La cristallizzazione da soluzione è un processo onnipresente in una grande varietà di applicazioni industriali, partendo dalla raffinazione del greggio per arrivare alla produzione di composti farmaceutici. In questo caso specifico, la taglia e la forma dei cristalli prodotti influenza tutti i processi che portano alla creazione delle pastiglie disponibili sul mercato e i loro effetti sul corpo umano.

Di conseguenza, non stupisce la quantità di soluzioni sviluppate per il controllo selettivo della morfologia e le dimensioni delle particelle cristallizzate. Lo scopo principale di questo lavoro di tesi è stato lo sviluppo e la validazione di un nuovo processo, chiamato *processo a 3 stadi*, composto dalla ripetizione ciclica di stadi di cristallizzazione, macinazione e dissoluzione per ottenere particelle più squadrate.

I risultati presentati in questo lavoro trattano tutti gli aspetti coinvolti nell'accurato sviluppo e caratterizzazione di un nuovo processo, in particolare gli strumenti di misura realizzati per misurare le proprietà di interesse, la caratterizzazione sperimentale ed i modelli matematici dei fenomeni fisici alla base delle singole operazioni unitarie e del processo e lo sviluppo di una strategia per uno studio efficiente della fattibilità di processo avendo a disposizione un numero limitato di informazioni ed esperimenti. È stato mostrato che:

- un nuovo setup stereoscopico basato su tecniche di imaging per la ricostruzione della morfologia dei cristalli e la stima delle loro dimensioni caratteristiche può essere usato per una caratterizzazione esaustiva di uno stadio di macinazione in un mulino continuo con sistema rotore-statore e per la stima dei parametri cinetici del corrispondente modello matematico.
- un modello matematico per il processo a 3 stadi, che include tutti i fenomeni dalla scala della singola particella a quella dell'intero processo, può essere utilizzato per una prima valutazione della fattibilità del processo e delle sue prestazioni, evidenziando come sia in principio possibile ottenere cristalli con le specifiche richieste.

- tramite una dettagliata campagna sperimentale, basata sui risultati del modello matematico, è stato possibile confermare la fattibilità del nuovo processo, nonostante la forte dipendenza del risultato finale dalle proprietà specifiche del composto.
- modelli matematici, capaci di rappresentare la realtà fisica dei fenomeni fondamentali, possono essere sfruttati per identificare i trend caratteristici del processo e fungere da guida durante gli stadi di design e sviluppo.
- è possibile identificare un gruppo di quattro esperimenti che costituiscono l'insieme indispensabile di test richiesti per ottenere una prima approssimazione di tutti i possibili prodotti ottenibili, fornendo anche informazioni in quantità tale da permettere la stima delle cinetiche del modello.

Il lavoro esposto costituisce una caratterizzazione dettagliata dell'effetto delle variabili operative e delle proprietà del composto sul prodotto finale, nonché dei vantaggi e degli svantaggi derivanti dalla implementazione del processo a 3 stadi a scapito di alternative più convenzionali, così come degli approcci utilizzabili per il design di processo.

ACKNOWLEDGEMENTS

First and foremost, I would like to express my sincere gratitude to my supervisor Prof. Dr. Marco Mazzotti, who accepted me as his PhD student and gave me the opportunity to work in an always motivating and diverse environment. Having the chance to work with a scientist and a person like him has certainly pushed me to always go the extra mile to keep up with the high standards and expectations.

Special thanks are also due to Dr. Pirmin Hidber and Dr. Marcello Bosco (F. Hoffmann - La Roche AG), whose constant supervision, inputs, and fruitful discussions throughout the duration of this project were always of great relevance and helped me a lot in getting a glimpse of how research problems are dealt with in the industry.

I would also like to thank Prof. Dr. Konrad Hungerbühler and Prof. Dr. Zoltan Nagy who generously agreed to co-supervise this thesis.

Thanks to all the people in the SPL group, who contributed to make this experience something unique. I owe a special mention to all the people I worked with, Stefan Schorsch, Dave Ochsenbein, Thomas Vetter, Ashwin Kumar Rajagopalan, Stefan Bötschi, Byeongho Ahn, and Zoran Bjelobrk, who contributed with their work to the results reported in this thesis. Thanks also to Daniel Trottmann and Markus Huber for the realization of the experimental setups used and the measurements performed in the course of the project. Acknowledgements are also due to all the students I had the chance to supervise and work with, who helped me with their creativity and personalities in various ways.

Thanks to my friends, the new ones and the old ones. Thanks to Stefano, Ashwin, and Fede, for being by my side through thick and thin, for accepting me even when I am not the most enjoyable person in my dark days, and for always finding the time to share opinions and thoughts. Thanks also to Cristina and Francesca, I hope I managed, at least from time to time throughout the day, to release a bit of your stress with my light-hearted jokes. Thanks John, for being a friend and an office mate and for all the discussions we had, even those not necessarily related to our work. Thanks also to Pawel and Dave, for the great times we shared in the past five years. A special mention is due to Lisa, a beautiful person I am very happy I got the chance to know and be friend with. Thanks to Stefan and Pietro for being the kind of guys always open to discuss about crystal shape and more.

Thanks to Florian, Thomas, Janik, Mattheus, Marina, Miriam, Stephan, Michael, Elena, Leo, Paola, Rafa, Giuseppe, Anna, Stefania, Cristina, Francesca, Chris, Stefano. This journey wouldn't have been the same without you.

Thanks to my parents and my brother, who always loved and supported me in everything I did, motivating me to always give my best and cheering for me. You are the best parents a son could ask for. I dedicate this work to you, because all of this would have not been possible without your help.

CONTENTS

1	INTRODUCTION	1
1.1	Crystal shape manipulation	2
1.2	Measurement device: the μ -DISCO	3
1.3	Image analysis pipeline	5
1.3.1	Step B: Adaptive background subtraction	5
1.3.2	Step C: Contour extracting and contour matching	6
1.3.3	Step D: 3D reconstruction and extraction of 2D/3D features	6
1.3.4	Step E: Particle classification	8
1.3.5	Step F: nD PSSD reconstruction	9
1.4	Structure of the thesis	10
2	COMPREHENSIVE CHARACTERIZATION OF BREAKAGE PROCESSES	13
2.1	Introduction	13
2.2	Mathematical model	15
2.2.1	Crystal and particle ensemble models	15
2.2.2	Population balance equation for milling processes	16
2.2.3	Solution of the PBE	24
2.2.4	Parameter estimation	24
2.3	Materials and methods	27
2.3.1	Materials	27
2.3.2	Experimental setup	28
2.3.3	Measurement tools	28
2.3.4	Preparation of seed crystals	29
2.3.5	Experimental protocol for breakage experiments	31
2.4	Results and discussion	32
2.4.1	Experimental characterization of the process	32
2.4.2	Model validation	38
2.4.3	Effect of residence time	47
2.5	Conclusions	49
2.6	Notation	51
3	IN-SILICO PROCESS VALIDATION	53
3.1	Introduction	53
3.2	Conceptual design	55
3.3	Mathematical model	57

3.3.1	Crystal model	57	
3.3.2	Population balance equation	59	
3.3.3	Results analysis and key performance indicators	65	
3.3.4	Parametric analysis	66	
3.4	Results and discussion	66	
3.4.1	Choice of model parameters and operating conditions	66	
3.4.2	Solution of the PBE	70	
3.4.3	Identification of reference conditions and process assessment	70	
3.4.4	Effect of mass dissolved	73	
3.4.5	Effect of the rotor speed	75	
3.4.6	Effect of the number of cycles	75	
3.4.7	Parametric study of the process and heuristic optimum	77	
3.4.8	Comparison with other processes	80	
3.5	Conclusions	83	
3.6	Notation	85	
4	EXPERIMENTAL PROCESS CHARACTERIZATION	87	
4.1	Introduction	87	
4.2	Theory	89	
4.2.1	Crystal model and PBE	90	
4.2.2	Solution of the PBE	93	
4.2.3	Process performance indicators	95	
4.3	Materials and methods	96	
4.3.1	Experimental setup	96	
4.3.2	Model compound	96	
4.3.3	Experimental protocol for 3-stage process experiments	98	
4.3.4	Experimental protocol for process comparison experiments	99	
4.3.5	Operating conditions	99	
4.3.6	Measurement techniques	101	
4.4	Results and discussion	101	
4.4.1	Feasibility and experimental reproducibility	101	
4.4.2	Experimental analysis and assessment of the 3-stage process	104	
4.4.3	Heuristic optimum experiment	108	
4.4.4	Comparison with other processes	109	
4.5	Conclusions	110	

4.6	Notation	114
5	SHORTCUT APPROACH FOR PROCESS DESIGN	117
5.1	Introduction	117
5.2	Theory	119
5.2.1	Mathematical modeling of the 3-stage process	119
5.2.2	Process performance indicators	123
5.2.3	Parametric analysis	124
5.2.4	Fitting of the kinetic parameters	133
5.2.5	Estimation of growth kinetics from in-silico data	135
5.3	Materials	137
5.3.1	Experimental setup	140
5.3.2	Solubility of γ D-Mannitol	140
5.3.3	3-stage process experimental protocol and factorial design	144
5.3.4	PSSD measurement setup and protocol	144
5.4	Results and discussion	145
5.4.1	Factorial design for the 3-stage process	145
5.4.2	From the attainable region to process design	153
5.4.3	Exploration of the process design space	154
5.5	Conclusions	156
5.6	Notation	158
6	CONCLUDING REMARKS & OUTLOOK	161
6.1	Imaging techniques and particle ensemble modeling	162
6.2	Breakage of needle-like particles	163
6.3	Improvements for the 3-stage process	164
6.4	Process characterization	165
6.5	3-stage process control	166
6.6	Industrial perspective	167
	BIBLIOGRAPHY	169

INTRODUCTION

Crystals are part of everyday life, being at the basis of common products, such as ice-cream and medicines, as well as natural phenomena, like snow-fall and stalactites. The macroproperties observable are strongly dependent on the microstructure of the single crystals, since it determines how molecules are incorporated on the surface and in the crystal lattice.

Crystallization is widely used in the chemical industry due to the possibility of obtaining highly purified and favorable form of a solid in a single processing step from an impure solution, with energy requirements significantly lower than those required by distillation or other purification techniques.¹ From a process point of view, the size and shape of crystals are properties of great relevance, given their strong impact on the successful and efficient performance of the downstream processes leading to the manufacturing of the final product.²⁻⁵

Usually, the shape of a crystal, often called habit or form, can be distinguished in equilibrium and growth morphology. The first is the shape adopted by a crystal, equilibrating with the surrounding environment, aimed at minimizing the surface energy, while the latter is the shape developed when growth is the dominant phenomenon. The morphology is determined by the symmetry of the internal crystal structure and the relative growth rates of the facets of the crystal, which are related to the surface integration of molecules on the surface. In crystallization processes, operating conditions and non-idealities generally lead to the production of particles whose size and shape are determined by the growth rates attained by each facet, which might differ from one crystal to another. This means that the process conditions and the process itself can be tuned in order to selectively manipulate particle morphology and obtain crystals satisfying the required specifications.

The main goal of this thesis is the design, characterization and development of a novel process, consisting in a combination of crystallization, milling, and dissolution steps, for the selective manipulation and control of crystal size and shape combining the experimental evidence with simulations performed using physically-sound mathematical models.

1.1 CRYSTAL SHAPE MANIPULATION

Given the relevance of particle morphology in the processing of solids, throughout the years several approaches have been developed in order to obtain particles with the desired shape. The different studies reported in literature, highlight how milling represents currently the ubiquitous and most effective process to change crystals' morphology. Nevertheless, the possibility of using in-line milling has been only partially explored and without considering the morphology of the ground particles.^{6,7} Tailored cooling profiles⁸⁻¹⁰ and additive addition^{11,12} are other approaches generally used for industrial applications. Temperature cycles, where dissolution and crystallization stages are periodically repeated, have also been investigated to control the morphology of crystals,¹³⁻¹⁵ but they find limited application at the industrial scale. Processes where temperature cycles are combined with the use of additives have also been investigated,¹⁶ along with the use of additives during milling to stabilize the particles and prevent re-aggregation.^{17,18}

The development of techniques for the selective manipulation of crystal size and shape and the identification of their optimal operating conditions heavily rely on the possibility of accurately measure and predict particle morphology. To this aim, mathematical models, accurately describing the crystal habit, are a fundamental requirement. While abundant literature can be found for models and experimental procedures for the characterization of particles with a single characteristic dimension, there is a significant lack of knowledge concerning particles with non-equant shapes, with a very limited number of works focusing primarily on simulation studies.¹⁹⁻²²

In this work, we develop and investigate a combined crystallization, milling, and dissolution process aimed at producing more equant crystals and a monodispersed powder. The main idea underlying this technology is exploiting the crystallization step to recover the solute from the solution and allow crystals to grow. The particles are subsequently ground in a continuous rotor-stator wet mill to reduce selectively their length and the suspension is therefore heated, in a dedicated and separate stage, to dissolve the fines formed during the wet milling step. These three steps are repeated until the final conditions are reached. The challenges lying in the development and characterization of this process are the lack of suitable measurement tools, mathematical models, and experimental evidence to support process design. All these aspects are tackled individually and in detail in the different chapters of this thesis. In particular, in this first

chapter, an in-house built imaging based measurement setup is presented, as it constitutes the basis for all the mathematical models and experimental activities presented in this thesis.

1.2 MEASUREMENT DEVICE: THE μ -DISCO

A major challenge of imaging-based particle sizing techniques is the dependence of the observed particle size on the orientation of the particle under inspection with respect to the camera. These orientation-related issues can be mitigated by means of a multi-camera setup which provides particle projections from different angles. The previously published stereoscopic imaging setup, henceforth referred to as FTC,²³ uses a dual-projection technique capable of merging particle size information provided by two cameras into n D PSSDs. This feature yields a more accurate measurement than what single-view setups can provide.²⁴ However, the major drawback of the FTC is its bulky mechanical design ($126 \times 126 \times 90$ cm), making it vulnerable to vibrations during image acquisition. Moreover, the Xenon flashes employed required additional optics to provide collimated light; Also, a square flow channel assembled by gluing four sapphire glass windows held by a brass holder was used, making maintenance of the device cumbersome.

Based on the issues described above, a more compact version of the optomechanical setup ($80 \times 74 \times 42$ cm) was developed with the goal of overcoming the problems associated with the FTC. The smaller setup described, henceforth referred to as *dual imaging system for crystallization observation* (μ -DISCO), fits into a standard laboratory hood and is less vibration-susceptible during operation. A schematic of the new setup is shown in Figure 1.1; it consists of two monochrome CMOS cameras (Point Grey Research, Canada) in an orthogonal configuration with telecentric optics (Opto Engineering, Italy) resulting in an orthographic projection with very low spatial distortions (< 0.1 %). The camera-lens system provides a field of view (FOV) of 2.41×2.02 mm at a nominal magnification of $3.5\times$. Two high-power, telecentric LED illuminators (Opto Engineering, Italy), which emit collimated chief rays parallel to the optical axis produce high contrast silhouettes of particles passing through the flow channel. The whole setup is mounted on an optical rail cross-construction. Manual XYZ-translation stages (Newport Corporation, USA) that allow high precision alignment of the two cameras, and a rotation stage (Newport Corporation, USA) that allows orienting the parallel illumination beam, are used. A microcontroller

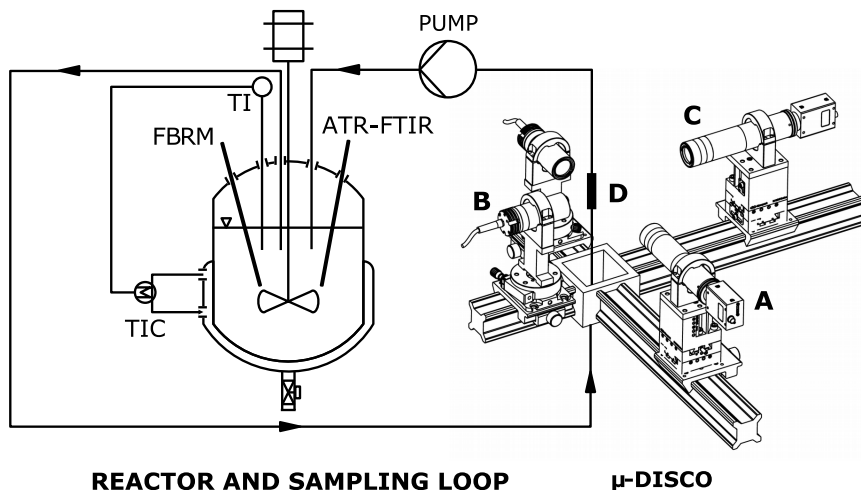


FIGURE 1.1: Schematic of the new dual imaging system for crystallization observation (μ -DISCO). The suspension flowing from the reactor through the flow channel (D) is back-light illuminated using two telecentric illuminators (B). The suspension is photographed using two digital cameras (A) with telecentric optics (C). The camera, lens and the illuminator system are mounted orthogonally on an optical rail construction.

(Atmel, USA) running in-house software provides an external trigger signal, which enables a synchronized image acquisition from the cameras.

The introduction of the new cameras allows to operate the μ -DISCO either in a *standard mode*, with a constant low frame rate (1–7 Hz), or in a *burst mode*, with higher frame rates up to 75 Hz. The burst mode is particularly useful for capturing processes with fast dynamics, such as dissolution. In standard mode, the μ -DISCO can be operated either online, that is, the image processing is performed in real-time, or offline, where the image processing is performed after the image acquisition for the entire measurement period. The cameras are connected to high-speed USB 3.0 ports and controlled with custom drivers implemented using the FlyCapture SDK (Point Grey Research, Canada).

The suspension is sampled from the reactor using a peristaltic pump (Watson-Marlow, Inc., UK) and flows through a single piece quartz square channel (FireflySci, Inc., USA) embedded in an insulated sampling loop. The cross-section of the flow channel is 2×2 mm and incorporates the two transitions between the circular tubing and the square channel at both

ends. A one-piece flow channel is superior to the old channel, because of a reduced risk of leakage and a completely eliminated risk of dissolution of the glue used to hold the channel.

1.3 IMAGE ANALYSIS PIPELINE

A multi-step, in-house developed image processing approach (illustrated in Figure 1.2) for extracting contours of particle silhouettes (Section 1.3.1 and Section 1.3.2), reconstruction of particle shapes in 3D (Section 1.3.3), and shape classification of the particles (Section 1.3.4) is presented.

In the following a brief and comprehensive description of the steps from **B** to **F** is reported for the sake of clarity and completeness.

1.3.1 Step B: Adaptive background subtraction

After the acquisition of a stereoscopic image pair, an adaptive background subtraction step^{25,26} is applied to both images in order to remove stationary content from the images such as dust, dirt or scratches on the flow cell, which tend to increase as the cell ages. The idea behind this technique is

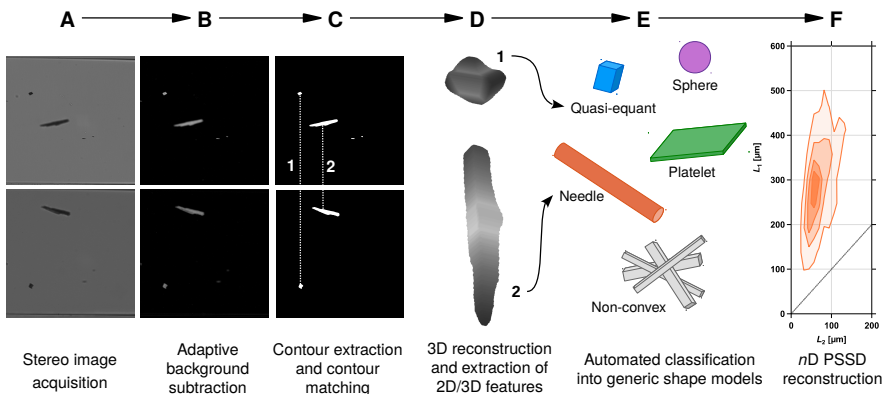


FIGURE 1.2: Illustration of the multi-step image processing approach, including the adaptive background subtraction (**B**), a contour matching algorithm (**C**), 3D shape reconstruction (**D**), and the automated shape classification of reconstructed particles (**E**). The result of this procedure is an n D particle size and shape distribution (PSSD) for each generic shape model.

to generate a foreground mask of pixels belonging to moving objects by estimating the stationary background of the scene, which can be subtracted from successive images. The subtraction of a new frame with the estimated background model results in a difference frame containing only moving objects, i.e., objects that appear new in the image.

1.3.2 *Step C: Contour extracting and contour matching*

This processing step identifies whether pixels in the image either depict a crystal or if they belong to the background. Given the difference image from the previous background subtraction step, we compute a binary image that labels every pixel as either foreground or background. Being the simplest and fastest segmentation algorithm, we use thresholding and classify all pixels by means of a global threshold $\tau \in [0, 1]$ found using a photometric calibration involving spherical latex beads (Beckman Coulter, USA) with a nominal diameter of 90 μm . It is a well-known fact that thresholding is prone to noise because the classification of each pixel is independent of its direct neighbors. Therefore, the segments might not be contiguous or contain holes. In order to cope with this problem, a median filter with window size of 5×5 pixels is applied to $G(x, y, t_k)$ after segmentation, followed by a morphological opening and closing operation with a rectangular structuring element with the size of 13 pixels.²⁷ These operations reduce noise and close thin concavities in the binary mask. In a successive step, the contour of the particle silhouettes is extracted using a boundary tracing algorithm.²⁸ Contours containing less than 50 connected pixels are considered to be below the optical resolution of the camera-lens system and are thus excluded from further analysis. Contours intersecting the image boundaries are discarded as they cannot provide an accurate size measurement of the corresponding particle. All image processing operations are implemented using the open source computer vision library OpenCV.²⁹

1.3.3 *Step D: 3D reconstruction and extraction of 2D/3D features*

The aim of this processing step is to find spatial correspondences between silhouettes on the two stereoscopic images that originate from the same crystal. The matching is performed based on conditions imposed on (i) the absolute difference in the z_w -coordinate (red axis of Figure 1.3 of the

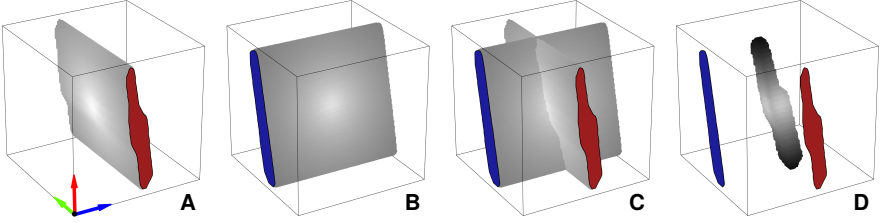


FIGURE 1.3: Volume intersection method used for the 3D reconstruction of particles being imaged by the two cameras. (A) and (B) show the volumes spanned by the two silhouettes, \mathcal{V}_A (red silhouette) and \mathcal{V}_B (blue silhouette); (C) illustrates the intersection of \mathcal{V}_A and \mathcal{V}_B ; (D) shows the final reconstructed visual hull $\mathcal{V} = \mathcal{V}_A \cap \mathcal{V}_B$.

contour centroids, and (ii) absolute or relative differences in the upper and lower z_w -coordinates of the bounding box of the contour.

In the first step, pairs of contours that satisfy the centroid threshold from the two matched stereoscopic images are checked for difference in the z_w -coordinate of the bounding box. On the one hand, if a pair of contour satisfies the threshold for absolute difference of the z_w -coordinate, it is considered to be matched. While on the other hand, if the absolute difference threshold is not met, but the relative difference threshold is satisfied, the contour pair is considered to be matched and is subjected to further image processing steps.

For the classification of crystals based on shape, a 3D volumetric model of each crystal is required from which shape attributes can be extracted and used in the context of shape classification. Shape-from-Silhouette (SFS)³⁰ is a popular technique for the shape estimation of an object from a set of calibrated silhouette images. The reconstruction obtained with this method, henceforth referred to as *visual hull* (VH), is the intersection of the projective sets (silhouette cones) obtained by unprojecting all camera-aligned silhouette images into 3D space. Since object concavities can only be recovered if they are visible in at least one of the silhouettes, the VH can be regarded as an upper bound of the actual object shape.

Due to its efficient implementation, the volume-based approach³¹ is the selected method for the reconstruction of the visual hull in this work. With the two orthogonally aligned cameras, \mathcal{V} can be computed by the volume intersection $\mathcal{V} = \mathcal{V}_A \cap \mathcal{V}_B$ of the two silhouette cones, \mathcal{V}_A and \mathcal{V}_B , each representing a discretized volume spanned by the two projected silhouettes as illustrated in Figure 1.3. A limitation of the exploited method in the given

application is the dependence of the reconstructed VH on the orientation of the particle with respect to the cameras. With only two cameras, the shape of the VH might be ambiguous, e.g., a needle-like particle cannot be distinguished from a platelet-like particle when it is oriented in a 45° -angle with respect to both cameras. This ambiguity also affects the reconstruction of flat, platelet-like particles, where certain orientations can lead to non-platelet shaped reconstructions.

1.3.4 Step E: Particle classification

The measurement of the particle size by means of imaging methods requires a size metric capable of adequately representing the characteristic size of the particle to be measured. Finding such a suitable metric requires prior 3D shape information of the particle before particle sizing is performed. In the context of this work, the task of classifying the shape of a crystal consists of assigning a generic shape model to each particle recorded by the stereoscopic camera setup, and hence categorizing crystals into shape groups that share certain geometric properties.

In general, one can distinguish between physically based morphological particle models and generic particle models. The first class of models uses crystallographic data and aims at reflecting the morphology of an ideal crystal as accurately as possible.²³ In contrast, generic particle models aim at simplifying the shape of the crystals as much as is sensible for a given application. The faces of crystals are not necessarily respected using such an approach and only the macroscopic form is considered. Following the definition of Schorsch et al.,²³ the generic model particles *sphere* and *needle* are distinguished, along with the new classes *quasi-equant*, *platelet*, and *non-convex*. Note that the non-convex class strongly resembles the class denoted by the term *agglomerate* in the work by Ochsenbein et al. to describe agglomerates of needle-like crystals.³² In this work, however, the more general term *non-convex* is used since this label is restricted not only to the agglomeration of needle-like crystals. The *non-convex* label in the context of this thesis might also include overlapping particles which exhibit non-convex shape, thus making it difficult to distinguish them from real agglomerates.

The set of generic shapes distinguished in this work is illustrated in process step E of Figure 1.2. Members of the *sphere* class are spherical objects (spheroids), which can be described with a diameter, L_1 , only. Elongated, needle-like particles are described by the *needle* class whose characteristic

dimensions are approximated by a cylindrical shape with length, L_1 , and width, L_2 , where $L_1 \gg L_2$. The class *quasi-equant* consists of regular, non-spherical particles, for which $L_1 \geq L_2 \geq L_3$ can be assumed, as for instance in the case of cuboid shaped crystals. The *platelet* class describes flat-shaped, tabular objects like platelet crystals, for which $L_1 \geq L_2 \gg L_3$ is assumed. The *non-convex* class is intended for the detection and classification of crystal agglomeration events yielding irregularly shaped particles.

Once the single particle has been assigned to its shape class, it is possible to calculate its dimensions. Two classes are considered in this thesis, the quasi-equant and the needles, as the appearance of objects of other nature has to be considered an experimental artifact.

The method for calculating L_1 and L_2 of needle-shaped particles from two orthogonal projections is identical to the one presented by Schorsch et al.³³

The sizes of quasi-equant particles are calculated based on the non-oriented bounding box enclosing the reconstructed 3D VH. The bounding box volume is calculated by $V_{\text{BB}} = abc$, where $a \geq b \geq c \geq 0$ are the length, width and height of the bounding box. For the purpose of satisfying the intuitive geometric relationship $V_{\text{VH}} = L_1 L_2 L_3$, the characteristic size is obtained by scaling the bounding box dimensions by a constant factor, i.e. $L_1 = m \cdot a$, $L_2 = m \cdot b$, and $L_3 = m \cdot c$, where $m = \sqrt[3]{V_{\text{VH}}/V_{\text{BB}}}$ and V_{VH} is the volume of the reconstructed VH.

1.3.5 Step F: nD PSSD reconstruction

The particle size and shape distribution (PSSD) can be reconstructed based on the number of descriptors chosen and is represented by a 1D, 2D, or 3D, discretized and normalized number- and volume-weighted density distributions. In order to obtain a PSSD from the sizes measured with the μ -DISCO, a binning procedure is employed along the different characteristic lengths. A linear grid with f_{L_x} bins of size ΔL_x , where $x = 1, 2$ or 3 , is used to obtain the PSSDs. Only a 2D PSSD is considered in this subsection, as it is the one used throughout the work described in this thesis. The number of particles in each bin, denoted by $N_{i,j}$ is counted and is related to the continuous distribution, $n(L_1, L_2)$ as

$$N_{i,j} = \int_{L_{2,j-1}}^{L_{2,j}} \int_{L_{1,i-1}}^{L_{1,i}} n(L_1, L_2) dL_1 dL_2 \quad (1.1)$$

The moment of a 3D PSSD can be used to evaluate the properties of interest, such as the characteristic lengths and broadness of the distribution, is defined as

$$\mu_{i,j} = \int_0^{\infty} \int_0^{\infty} L_1^i L_2^j n(L_1, L_2) dL_1 dL_2 \quad (1.2)$$

The discretized normalized number- and volume-weighted distribution, $\hat{n}_{i,j}$ and $\hat{n}_{i,j}^V$, respectively are approximated to consider the effect of the number and size of bins and are given by the following equations

$$\hat{n}_{i,j} = \frac{N_{i,j}}{\Delta L_1 \Delta L_2 \sum_{i=1}^{f_{L_1}} \sum_{j=1}^{f_{L_2}} N_{i,j}} \quad (1.3a)$$

$$\hat{n}_{i,j}^V = \frac{\bar{L}_{1,i} \bar{L}_{2,j}^2 N_{i,j,k}}{\Delta L_1 \Delta L_2 \sum_{i=1}^{f_{L_1}} \sum_{j=1}^{f_{L_2}} \bar{L}_{1,i} \bar{L}_{2,j}^2 N_{i,j}} \quad (1.3b)$$

where, $\bar{L}_{1,i}$ and $\bar{L}_{2,j}$ are the size corresponding to the bin's pivot along the two characteristic lengths, respectively. It is worth noting that the number- and volume-weighted densities, are further normalized with the mode of the respective distributions which is used for the PSSDs presented in the thesis.

1.4 STRUCTURE OF THE THESIS

This thesis aims first of all at developing all the mathematical equations required to quantitatively model every aspect of the 3-stage process, spanning from the ensemble of crystals and the single unit operations to the evolution of the size and shape of particles throughout the different cycles. Subsequently, we develop experimental protocols to perform experiments to collect accurate and reliable data, using the μ -DISCO presented in Section 1.2, that are used first to characterize the basic phenomena underlying each stage and to estimate the kinetics of the mathematical model, and then to describe the 3-stage process itself.

In Chapter 2 a comprehensive experimental and theoretical investigation for the quantitative description of the breakage of needle-like crystals of β L-Glutamic acid in a continuous rotor-stator wet mill, considering both the properties of the single crystals and the operating conditions, are carried

out. Based on the data acquired, the characteristic kinetic parameters of the model are estimated, thus obtaining a simulation platform for the quantitative prediction of product properties.

In Chapter 3 the mathematical model for the 3-stage process, capable of tracking the evolution of the whole ensemble of crystals, is presented and used for a thorough in-silico investigation of the broad design space for the assessment of process feasibility. Furthermore, the simulations are used to understand the effect of each operating conditions on the properties of the products and to make a comparison with more conventional processes for the sake of completeness.

Chapter 4 reports the results of the model-driven experimental campaign performed to investigate the outcome of the 3-stage process using β L-Glutamic acid. First, the laboratory rig is presented. Then, the operating conditions of interest are investigated by means of specifically designed sets of experiments. Finally, an experiment performed adopting heuristic optimum conditions is carried out and compared with the outcome of a single cooling stage, both with and without final milling, to highlight the benefits derived from the application of the newly developed process.

Chapter 5 reports in detail an experimental protocol for the thorough characterization of the outcome of the 3-stage process when it is applied to a compound for which only the solubility is known. First, a set of experiments, constituted by the minimum possible number of tests, is identified by analyzing process simulation results and performed using γ D-Mannitol. Based on these four experiments, the achievable region, constituted by all the possible process outcomes, is identified and used to estimate the characteristic kinetic parameters of the model for further process development.

Finally, Chapter 6 reports conclusions on the whole work and an outlook concerning the different aspects considered.

Please note that this is a thesis by published works and, as such, the contents of the different chapters coincide with that published in a number of peer reviewed journals.³⁴⁻³⁷ Each chapter can be viewed as a standalone piece of work, for which all the necessary definitions are provided within the corresponding section.

EXPERIMENTAL CHARACTERIZATION AND MATHEMATICAL MODELING OF BREAKAGE OF NEEDLE-LIKE CRYSTALS IN A CONTINUOUS ROTOR-STATOR WET MILL

2.1 INTRODUCTION

Crystallization is of key importance in the fine and pharmaceutical industry, where the active pharmaceutical ingredients are recovered from a solution. The crystals thereby produced are further processed to manufacture the tablets available on the market. The type and amount of downstream processes employed strongly depends on the morphology of the crystallized particles. Furthermore, the impact of shape is particularly relevant on the filterability and compactability of the produced powder, for example by affecting its mechanical and chemical stability. Particularly in the pharmaceutical industry, needle-like crystals are highly undesirable products of the crystallization step, since they are characterized by very poor flowability and are inclined to the formation of significant amounts of fines when treated. Along with the shape also the polydispersity of product properties heavily influences the processing of the powder. Several authors³⁸⁻⁴⁰ highlighted how the performance of filtration processes depends on the particle habit and the crystal size distribution. It is in this framework that several efforts were made in the last years in order to find operating conditions and process strategies that could help in properly manipulating the shape of crystals. An accurate tuning of the morphology of particles and their distribution might in fact be helpful to better operate the downstream processes, thus eventually allowing to significantly reduce the duration of the whole manufacturing process.

Nowadays a large majority of processes in the pharmaceutical and food industry include a stage where mechanical action is applied in order to reduce the particle size and to obtain more equant crystals. Breakage is

Salvatori F. and Mazzotti M., Experimental characterization and mathematical modeling of breakage of needle-like crystals in a continuous rotor-stator wet mill, *Crystal Growth & Design*, 2018, – (-), XXX-XXX.

mainly performed in different types of mills and is viewed as part of the downstream process. To reduce heating, thus possible decomposition, of the solid particles, wet milling devices, where the whole particles suspension flows through the grinding chamber, are used. Given their importance in industrial applications, a lot of effort has been made by several authors to characterize different aspects of grinding processes, such as the effect of milling on crystals properties, i.e. surface properties or loss in crystallinity.^{41,42} Others^{22,43,44} propose mathematical models to improve the understanding of the underlying mechanisms of particles breakage and therefore to obtain a better control on the outcome of this process.

Population balance equations (PBE)⁴⁵ allow, under specific mixing assumptions for the particle slurry, to describe the time evolution of the whole ensemble of crystals. These models include specific terms to describe the different phenomena occurring during crystallization, from nucleation to agglomeration. The main advantage of this approach is the possibility of achieving a good compromise between simplicity and detailed characterization of the fundamental mechanisms. Several examples of this model, as well as of correlations for the description of the kinetic parameters in the population balance equation, are available in the literature.^{46,47} Currently most of the models available are not considering the evolution of shape of crystals during breakage, also due to the limited amount of suitable enhanced imaging devices commercially available. Nevertheless, in the past few years, several efforts have been made to characterize particle morphology by means of other descriptors, such as roundness, or to improve the daughter distributions to better characterize fragments distribution.⁴⁸⁻⁵⁰

It is in this framework that we aim at developing a new morphological population balance equation model, capable of tracking the evolution of the size and shape of the single crystals and to quantitatively simulate the particle size and shape distribution, a feature hardly achieved before, of the product powder under a broad range of operating conditions, in a continuous rotor-stator wet mill. To this aim, new constitutive equations are developed to correctly take into account and to model the physics underlying the different phenomena occurring in the process. These equations include those needed to describe how fast the particles are breaking, as well as those describing the formation of new fragments, particularly their number, size, and shape. The equations presented in this work consider the evidence already collected for the effect of size and shape in the models available in literature and further build on it to quantitatively describe the macroscopic physics of grinding processes. The population balance

equation developed is based on measurable quantities, i.e. the sizes of the crystals, instead of hardly quantifiable properties of the particles.

The development of the new mathematical model is based on a thorough experimental characterization of the system, where several properties of the products are analyzed. A detailed experimental campaign is carried out performing different sets of experiments aimed at investigating the effect of the different operating conditions on the product properties. The results collected can be used at first for an understanding of the process and then as a training set for the quantitative estimation of the model parameters.

The chapter is organized as follows. In Section 2.2 the theoretical bases of the model we developed to describe breakage of needle-like particles and the fitting procedure used to estimate the parameters characteristic of said model are reported. Section 2.3 describes the materials and the experimental procedure adopted in the laboratory activity required to validate the proposed model. In Section 2.4 the outcome of the extensive experimental campaign aimed at investigating the effect of different operating conditions on the milled crystals will be reported and analyzed in detail. In Section 2.5 conclusions and final remarks regarding the obtained results will be presented.

2.2 MATHEMATICAL MODEL

In this work, a mathematical model for the quantitative description of the breakage of needle-like crystals in a continuous rotor-stator wet mill is proposed, based on morphological population balance equations (MPBEs),⁴⁵ which describe the evolution of the multidimensional crystal distribution of an ensemble of crystals under the action of different mechanisms.

2.2.1 *Crystal and particle ensemble models*

The description of the crystalline size and shape by means of a mathematical model with a reduced number of features is of great interest for a quantitative description of crystallization processes. The model adopted for the single crystal should be able to capture the characteristic multi-faceted nature of the crystals themselves while enabling feasible computational burden in the context of process simulations. To comply with these requirements and in line with the quality and the type of data collected with the μ -DISCO, an in-house developed stereoscopic dual-camera imaging setup described in detail in Section 2.3.3, the generic particle model, as

suggested by Schorsch et al.²³ and following the implementation of Rajagopalan et al.,⁵¹ is adopted. Here, needle-like crystals are assumed to be cylinders with length L_1 and width L_2 . Based on the values exhibited by the individual particles, the particle size and shape distribution of the ensemble $n(L_1, L_2)dL_1dL_2$ is calculated. For a better visualization, the function $n(L_1, L_2)dL_1dL_2$ is plotted in the L_1L_2 -plane as contour lines, along which the function $n(L_1, L_2)$ attains constant value.

2.2.2 Population balance equation for milling processes

The possibility of tracking the evolution of the size and shape of an ensemble of crystals subject to different mechanisms is required for the model-based design and optimization of crystallization processes aimed at tuning product properties. In this framework, the morphological population balance equations represent a vital tool. Unfortunately, only a small number of works^{46,48,49} focuses on breakage of complex-shaped crystals, due to the difficulties in describing the size and shape of the particles and their fragments and to the lack of established measurement tools providing quantitative and accurate information on the particle morphology of ensembles of crystals.

The morphological population balance equation that we use to describe a continuous rotor-stator wet mill at steady-state, in the case of perfectly segregated flow (i.e. the grinding chamber is assumed to be a tubular apparatus), constant supersaturation, and isothermal conditions, reads as:³⁴

$$\frac{\partial n(L_1, L_2, \tau)}{\partial \tau} = B_1 + B_2 - D \quad (2.1)$$

$$B_1 = \int_{L_1}^{\infty} K_1(x, L_2)n(x, L_2, \tau)g_1(L_1, x)dx \quad (2.2)$$

$$B_2 = \int_{L_2}^{\infty} K_2(L_1, y)n(L_1, y, \tau)g_2(L_2, y)dy \quad (2.3)$$

$$D = K_1(L_1, L_2)n(L_1, L_2, \tau) + K_2(L_1, L_2)n(L_1, L_2, \tau) \quad (2.4)$$

$$n(L_1, L_2, \tau = 0) = n_0(L_1, L_2) \quad (2.5)$$

Here, it is assumed that particles can break only along one characteristic dimension during each breakage event, in line with the assumption of breakage in two fragments only. Simultaneous fracture along both L_1 and L_2 can be correctly described by two subsequent breakage events along one and along the other single dimension. In Equation 2.1, $n(L_1, L_2, \tau)$ is the number density crystal size and shape distribution, defined on the

internal coordinates L_1 and L_2 , corresponding to the characteristic particle descriptors, at the residence time τ . The term D appearing on the right hand side of the equation is called the *death term*, representing the number of particles of size L_1 and L_2 broken per unit time, while B_1 and B_2 are the so-called *birth terms* corresponding to the formation of crystals of size L_1 and L_2 through the breakage of larger particles along L_1 and L_2 , respectively. The quantities K_1 and K_2 are the *breakage frequencies*, alas the number of breakage events occurring along each characteristic dimension per unit time, while $g_1(L_1, x)$ and $g_2(L_2, y)$ are the *daughter distributions*, describing, according to the mechanism of the breakage event, the size and shape of the newly formed fragments. Specific mathematical models, along with a thorough analysis of the effect of the different parameters appearing in each of them, are derived for the constitutive equations appearing in these terms in the following sections.

Two different approaches can be adopted to this aim. The first would require the quantitative description of solid and fracture mechanics at the scale of the individual crystals. The second approach, which is adopted in this work, uses empirical relationships that capture the key physical effects and trends. This type of equations allows to include characteristic features of the fundamental mechanisms underlying breakage events, while reducing the modeling effort.

2.2.2.1 Breakage frequency

The rate at which particles are broken depends not only on the conditions at which grinding is carried out, but also on the crystal morphology. To capture this, the constitutive equations presented in this work for the breakage frequencies are the product of three terms as follows:

$$K_1 = o_1(\mathbf{z})f_1(L_1)h_1(\Phi) \quad (2.6)$$

$$K_2 = o_2(\mathbf{z})f_2(L_2)h_2(\Phi) \quad (2.7)$$

The functions depend on the following vector of model parameters:

$$\mathbf{p} = [p_{11}, p_{12}, p_{13}, p_{14}, p_{21}, p_{22}, p_{23}, p_{24}] \quad (2.8)$$

The function $o_j(\mathbf{z})$ depends on the set of operating conditions of the process, that we identify with the vector \mathbf{z} , consisting for instance of the suspension density. In this work, the only operating condition considered in \mathbf{z} is the rotor speed θ , while the effect of the suspension density ρ_S is

assumed to be negligible in the range investigated, hypothesis that will specifically be verified in Section 2.4.1.2. The proposed functional form is:

$$o_j(\mathbf{z}) = p_{j1} E_M = p_{j1} \left(\frac{1}{2} m_M v^2 \right) = p_{j1} m_M (\theta r_M)^2 \quad (2.9)$$

where the function $o_j(\mathbf{z})$ represents the fraction of kinetic energy transferred from the rotor to the crystals thus causing the particles to break, while m_M is the mass of the rotor, r_M is its radius, and p_{j1} is a fitting parameter (i.e. it accounts for non-idealities, fraction of energy transferred from the mill to the crystals, etc.).

The function $f_j(L_j)$ appearing in Equations 2.6 and 2.7 takes into account the effect of the length of crystals on their fracture. Due to the higher stresses generated in larger particles when a force is applied, it is intuitive to assume that the breakage frequency must be directly proportional to the size L_j of the crystals.⁵² However, the breakage of particles becomes less and less favorable the smaller the particle is. Below a certain dimension, typically called *grinding limit*, the breakage no longer occurs. In order to take into account both these effects the suggested functional form is:

$$f_j(L_j) = \left(\frac{L_j}{L_{\text{ref},1}} \right)^{p_{j2}} \left(1 + \exp \left(- \frac{L_j - p_{j3}}{L_{\text{ref},2}} \right) \right)^{-1} \quad (2.10)$$

where $L_{\text{ref},1} = 1000 \mu\text{m}$ and $L_{\text{ref},2} = 1 \mu\text{m}$. While on the one hand the choice of these values is arbitrary, on the other it reduces numerical problems when implemented in the model for process simulations.

Other than size, also the aspect ratio of the particle, i.e. $\Phi = L_1/L_2$, plays a crucial role in determining its breakage frequencies; the function $h_j(\Phi)$ in Equations 2.6 and 2.7 takes this into account. In particular, it is obvious that particles with the same length L_1 will break more (less) likely lengthwise the thinner (thicker) they are, i.e. the larger (smaller) is their aspect ratio Φ . To account for these effects, the functional form chosen for $h_1(\Phi)$ is monotonically increasing with Φ , but reaches a finite value as Φ reaches very large values:

$$h_1(\Phi) = \frac{\Phi}{\Phi + p_{14}} \quad (2.11)$$

Similarly we define $h_2(\Phi)$ as:

$$h_2(\Phi) = \frac{p_{24}}{\Phi + p_{24}} \quad (2.12)$$

By combining the three terms defined above, Equations 2.6 and 2.7 can be recast as:

$$K_1 = p_{11} m_M (\theta r_M)^2 \left(\frac{L_1}{L_{\text{ref},1}} \right)^{p_{12}} \left(1 + \exp \left(-\frac{L_1 - p_{13}}{L_{\text{ref},2}} \right) \right)^{-1} \frac{\Phi}{\Phi + p_{14}} \quad (2.13)$$

$$K_2 = p_{21} m_M (\theta r_M)^2 \left(\frac{L_2}{L_{\text{ref},1}} \right)^{p_{22}} \left(1 + \exp \left(-\frac{L_2 - p_{23}}{L_{\text{ref},2}} \right) \right)^{-1} \frac{p_{24}}{p_{24} + \Phi} \quad (2.14)$$

Figure 2.1 shows the effect of parameters p_{12} , p_{13} , and p_{14} in Equation 2.13. The parameter p_{12} determines not only how strongly the breakage frequency depends on the length L_1 of the crystal, but also the type of dependence, as observed in Figure 2.1 (a). The parameter p_{13} determines, along with its functional form, a range of sizes L_1 centered in $L_1 = p_{13}$, below which breakage no longer occurs; Figure 2.1 (b) shows the effect of this parameter on the value of K_1 . The parameter p_{14} determines the shape of the crystal for which, given the length-to-width ratio Φ , the breakage along L_1 becomes unfavored when compared to that along L_2 , as shown in Figure 2.1 (c). Figure 2.1 (d) and (e) show possible contour lines for the breakage frequencies K_1 and K_2 , respectively, in the $L_1 - L_2$ plane. The shape of these contour lines, as well as the value of the breakage frequencies, can be adapted in order to quantitatively describe the experimental evidence by fitting the values of the different parameters appearing in Equations 2.6 and 2.7 to a set of dedicated data.

2.2.2.2 Daughter distributions

The daughter distribution $g_j(L_j, x)$ is the function that, according to the breakage physics, describes the size distribution of the fragments formed after the breakage of a crystal of initial size x . In the model developed in this work, breakage along each characteristic dimension occurs according to the corresponding underlying daughter distribution. Each daughter distribution function for a cylindrical particle is subject to the two following constraints, as reported here for both g_1 and g_2 :

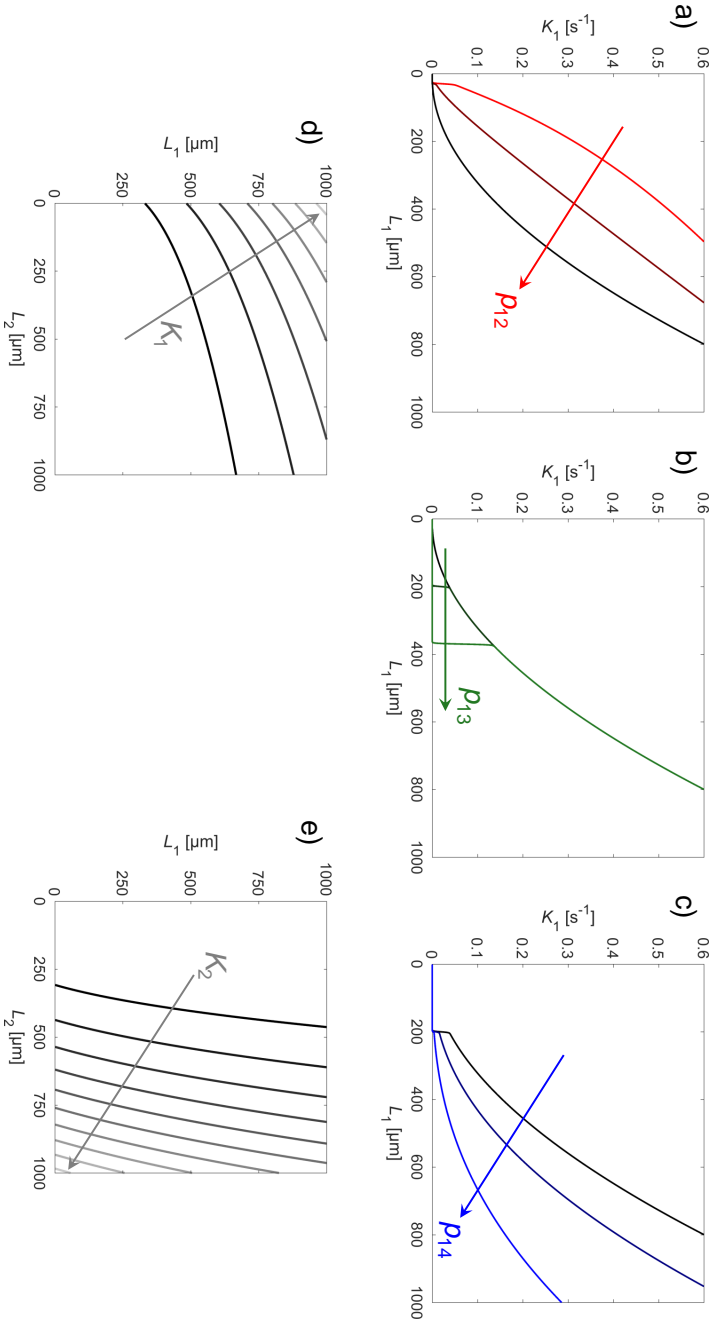


FIGURE 2.1: Effect of different parameters on the breakage frequency K_1 . The arrows are used to point towards increasing values of the corresponding quantity of interest. In (a), the effect of parameter p_{12} , determining the functional dependence of K_1 on size L_1 , is shown. Panel (b) illustrates the influence of the grinding limit p_{13} . In panel (c), the effect of increasing values of p_{14} is reported. Finally, panels (d) and (e) show as contour curves the breakage frequencies K_1 and K_2 as functions of sizes L_1 and L_2 .

$$\int_0^x g_1(L_1, x) dL_1 = 2 \quad (2.15)$$

$$\int_0^x L_1 g_1(L_1, x) dL_1 = x \quad (2.16)$$

$$\int_0^y g_2(L_2, y) dL_2 = 2 \quad (2.17)$$

$$\int_0^y L_2^2 g_2(L_2, y) dL_2 = y^2 \quad (2.18)$$

Equations 2.15 and 2.17 impose the number of fragments formed when a particle undergoes a breakage event, assumed equal to two in this work. Equations 2.16 and 2.18 impose that the length x and the cross sectional area y^2 of the mother particle are preserved, thus ensuring that the volume of the formed fragments is equal to the volume of the broken particle. Note that from Equation 2.18 the width of the particles is not preserved under breakage, i.e. $\int_0^y L_2^2 g_2(L_2, y) dL_2$ is larger than y .

In this work, three different types of daughter distributions are proposed. For the sake of clarity, we start focusing on g_1 , for which Figure 2.2 illustrates three different types of behavior. Figure 2.2 (a) shows the daughter distribution for cleavage, where, due to the breakage event, two particles of approximately equal size are formed. The equation chosen to describe such a distribution is a Gaussian function with mean μ equal to half of the size of the mother particle η .

$$g_1(L_1, \eta) = \frac{2}{\sqrt{\pi}\sigma \operatorname{erf}\left(\frac{\eta/2}{\sigma}\right)} \exp\left(-\left(\frac{L_1 - \eta/2}{\sigma}\right)^2\right) \quad (2.19)$$

The standard deviation σ strongly impacts the shape of the daughter distribution; the higher the value of this parameter, the easier the breakage of crystals in points further from the center. For very large values of σ , the resulting distribution is a constant function, corresponding to equal probabilities of breaking the mother crystal anywhere along its length, as shown in Figure 2.2 (c). Lower and lower values of σ , on the other hand, represent grinding processes where breakage occurs more and more favorably around the center of the crystal, eventually having a perfectly symmetric fracture of the mother particle into two fragments of the same size, as shown in Figure 2.2 (b).

The uniform breakage distribution and the perfectly symmetric cleavage distribution can also be modeled directly and not as the limit of the ge-

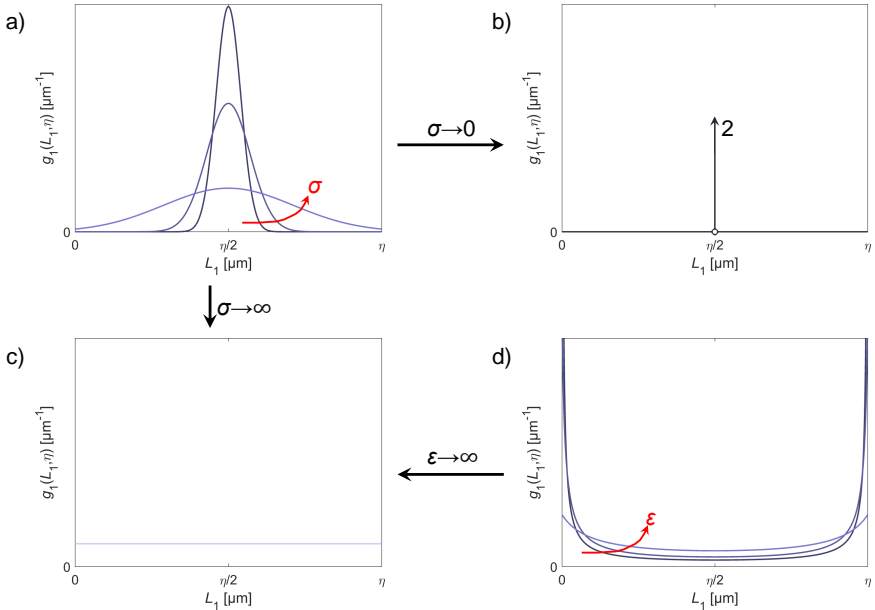


FIGURE 2.2: Exemplary daughter distribution functions for different breakage mechanisms. In panel a) the Gaussian bell is used to describe cleavage around the center of the crystal of size η . Decreasing the variance σ leads to the formation of crystals that are more and more symmetric. For values of σ approaching zero, the Gaussian function collapses on the Delta Dirac distribution, where two fragments of equal size are formed, as shown in panel b). On the other hand, for σ approaching infinity, the crystal can be broken in any point, as described by the constant function reported in panel c). In panel d), the daughter distribution describing attrition is plotted. The higher the value of the parameter ϵ , the higher the probability of detaching splinters from points far from the particle tip. Eventually, when ϵ approaches infinity, the random breakage distribution shown in panel c) is obtained.

neral Equation 2.19 for σ approaching infinity and zero, respectively. The corresponding functional form for the former is:

$$g_1(L_1, \eta) = \frac{2}{\eta} \quad (2.20)$$

and for the latter:

$$g_1(L_1, \eta) = 2\delta(L_1 - \eta/2)dL_1 \quad (2.21)$$

where we use the Delta Dirac distribution, $\delta(L_1 - \eta/2)$ centered in $\eta/2$.

Another possible breakage mechanism is attrition, where small fragments are detached at the corners of the crystal. In this work, the equation chosen to model this phenomenon is

$$g_1(L_1, \eta) = \frac{1}{\log\left(\frac{\eta+\varepsilon}{\varepsilon}\right)(L_1 + \varepsilon)} - \frac{1}{\log\left(\frac{\eta+\varepsilon}{\varepsilon}\right)(L_1 - \eta - \varepsilon)} \quad (2.22)$$

The parameter ε can be used to choose the maximum size of the fragment: as shown in Figure 2.2 (d), increasing this parameter leads to larger size of fragment; on the limit of ε approaching infinity, Equation 2.22 approaches the uniform distribution of Equation 2.20.

The equations presented here for g_1 , must be reformulated for g_2 , thus obtaining:

$$g_2(L_2, \eta) = \frac{4L_2}{\sqrt{\pi}\sigma\text{erf}\left(\frac{\eta^2/2}{\sigma}\right)} \exp\left(-\left(\frac{L_2^2 - \eta^2/2}{\sigma}\right)^2\right) \quad (2.23)$$

$$g_2(L_2, \eta) = \frac{4L_2}{\eta^2} \quad (2.24)$$

$$g_2(L_2, \eta) = 4L_2\delta\left(L_2^2 - \frac{\eta^2}{2}\right) \quad (2.25)$$

$$g_2(L_2, \eta) = \frac{2L_2}{\log\left(\frac{\eta^2+\varepsilon^2}{\varepsilon^2}\right)(L_2^2 + \varepsilon^2)} - \frac{2L_2}{\log\left(\frac{\eta^2+\varepsilon^2}{\varepsilon^2}\right)(L_2^2 - \eta^2 - \varepsilon^2)} \quad (2.26)$$

However, if the cross sectional area L_2^2 is considered as an internal coordinate instead of L_2 , the same daughter distributions for the length L_1 can be extended to describe the same breakage mechanisms also along this dimension.

2.2.3 Solution of the PBE

The morphological population balance equation is solved on a grid consisting of 201 and 101 points for the internal variables L_1 and L_2 , respectively. In order to ensure the preservation of the mass and of the number of fragments after breakage, the fixed pivot scheme suggested by Kumar et al.⁵³ has been implemented. The set of ordinary differential equations obtained by discretizing the population balance equation in the L_1 and L_2 directions is integrated over time using the Matlab ODE15 solver.

2.2.4 Parameter estimation

The estimation of the model parameters has been performed by fitting the model outcome to the results of a dedicated experimental campaign performed according to the protocol described in Section 2.3.5; its results are reported in Section 2.4.1.3. In the following, a detailed description of the fitting procedure and of the method adopted for the estimate of the confidence intervals is reported.

2.2.4.1 Objective function and optimization routine

The parameter estimation performed in this work is based on the maximum likelihood estimate, which consists in finding the set of parameters, identified by the vector \mathbf{p}^* , maximizing the probability of obtaining the measured set of experimental data. Assuming that the independent variables are deterministic, that the errors are distributed with zero mean and a specific variance, and that the errors in the different measurements are independent and uncorrelated, the maximum likelihood estimate of the vector of parameters \mathbf{p} is the vector minimizing the following function:

$$F(\mathbf{p}) = \frac{N_E}{2} \sum_{i=1}^{N_O} \ln \sum_{j=1}^{N_E} \left(\frac{y_{ij} - \hat{y}_{ij}(\mathbf{p})}{y_{ij}} \right)^2 \quad (2.27)$$

In Equation 2.27, N_E represents the total number of experimental measurements, N_O is the number of considered outputs, y_i represents a specific property of the measured particle size and shape distribution for the i -th experiment that needs to be fitted, while $\hat{y}_i(\mathbf{p})$ is the corresponding model estimation according to the set of parameters \mathbf{p} .

The quantification of the kinetic parameters requires the minimization of a nonlinear, nonconvex equation. The solution of such a problem is not trivial,

given the possible presence of several local minima. Therefore, both a robust optimization routine, capable of avoiding these attractors, and a good first-guess value for the model parameters are required. To this aim, the Matlab genetic algorithm routine provided by the Matlab optimization toolbox has been used. The population size chosen is 100, while the crossover fraction adopted is 0.70. The algorithm is seeded by providing individuals obtained by combination of random values of the different optimization variables by latin hypercube sampling. After 10 generations the algorithm is reseeded providing an initial population where 50 % of the individuals is randomly picked from the last population of the previous run and 50 % is randomly generated according to the aforementioned method. This allows to span the largest domain of the parameter space by preserving at the same time the winning traits identified in the previous run of the algorithm. Simulations are performed on a Computer with an Intel(R) Xeon(R) CPU E5-2687W v3 @ 3.10 GHz processor, 20 cores, and 32 GB of RAM.

Two cautionary remarks are worth making. First, despite the possibility of robustly identifying a minimum for Equation 2.27, there is no guarantee that the said minimum is the global minimum of the function. Then, the identified set of parameters can be used to estimate the outcome of a grinding process within the investigated range of operating conditions (interpolation), but there is no guarantee that the predictions of the model can be extrapolated to different conditions.

2.2.4.2 Confidence intervals estimation

The confidence intervals estimated together with the optimal set of parameters \mathbf{p}^* provide an indication of the overall quality of the fitting as well as of the uncertainty associated to each estimated parameter value. They are usually estimated for a specified level of confidence, which corresponds to the probability of obtaining a value for the parameters in the specified intervals using repeated samples. To this aim, the Jacobian of the model with respect to the estimated parameters can be used to get an estimate of the confidence intervals. The general formulation of the Jacobian matrix is

$$\mathbf{J} = \left[\frac{\partial f_i}{\partial x_j} \right] \quad \text{with } i, j = 1, \dots, n \quad (2.28)$$

The element J_{ij} of the Jacobian is the derivative of the function f_i with respect to the variable x_j . If the set of variables \mathbf{x} is equal to the vector of parameters \mathbf{p} and the function \mathbf{f} is the vector of model output $\hat{\mathbf{y}}$, the element

J_{ij} of the Jacobian corresponds to one of the sensitivity equations of the model. The diagonal of the measurement error covariance matrix \mathbf{S} can be approximated by the weighted sum of the residuals

$$S_{ii} \approx \sigma_i^2 = \frac{1}{N_E} \sum_{j=1}^{N_E} (y_j - \hat{y}_j(\mathbf{P}^*))^2 \quad (2.29)$$

By linearizing the non-linear equation and by assuming normally distributed errors, the positive semidefinite parameter covariance matrix \mathbf{V} can be estimated using the Jacobian matrix as

$$\mathbf{V} \approx (\mathbf{J}^T \mathbf{S} \mathbf{J})^{-1} \quad (2.30)$$

The matrix can be used to identify the hyperellipsoidal parameters confidence region. Such hyperellipsoid is defined for the confidence level α and can be used to get an approximation of the confidence interval for the j -th parameter:

$$C_{ij} = \sqrt{V_{jj}} t_{1-\alpha/2}^{N-k} \quad (2.31)$$

Here, $t_{1-\alpha/2}^{N-k}$ represents the value of the t -statistics with $N - k$ degrees of freedom at a confidence level α . The estimated confidence intervals should be considered in light of the uncertainty introduced with the linearization hypothesis, but provide nevertheless qualitative information on how well the parameters are estimated.

2.2.4.3 Fitted outputs

In order to determine the set of kinetic parameters appearing in Equations 2.13 and 2.14, it is necessary to identify the set of outputs to be fitted. Despite the interest in tracking the evolution of the entire crystal ensemble, using the whole particle size and shape distribution as a fitted output is practically impossible, given the high computational burden required in this case. Therefore, it is more convenient to use the moments of the distribution to evaluate the average sizes, which are the fitted quantities. The μ_{ij} -cross moment of the particle size and shape distribution $n(L_1, L_2, \tau)$ is defined as

$$\mu_{ij}(\tau) = \int_0^\infty \int_0^\infty L_1^i L_2^j n(L_1, L_2, \tau) dL_1 dL_2 \quad (2.32)$$

However, the μ -DISCO cannot measure reliably particles whose size is below approximately $L_{\min} = 10 \mu\text{m}$. Therefore, in the model, this value is

Fitted properties	Experimental	Simulated
$L_{1,N}$	μ_{10}/μ_{00}	$\hat{\mu}_{10}/\hat{\mu}_{00}$
$L_{2,N}$	μ_{01}/μ_{00}	$\hat{\mu}_{01}/\hat{\mu}_{00}$
$L_{1,V}$	μ_{22}/μ_{12}	$\hat{\mu}_{22}/\hat{\mu}_{12}$
$L_{2,V}$	μ_{13}/μ_{12}	$\hat{\mu}_{13}/\hat{\mu}_{12}$
$\sigma_{1,N}$	$\sqrt{\mu_{20}/\mu_{00} - (\mu_{10}/\mu_{00})^2}$	$\sqrt{\hat{\mu}_{20}/\hat{\mu}_{00} - (\hat{\mu}_{10}/\hat{\mu}_{00})^2}$
$\sigma_{2,N}$	$\sqrt{\mu_{02}/\mu_{00} - (\mu_{01}/\mu_{00})^2}$	$\sqrt{\hat{\mu}_{02}/\hat{\mu}_{00} - (\hat{\mu}_{01}/\hat{\mu}_{00})^2}$

TABLE 2.1: Average quantities fitted in this work

used as the lower integration limit to evaluate the moments corresponding only to the portion of the simulated particle size and shape distribution in the size range measurable by the device.

$$\hat{\mu}_{ij}(\tau) = \int_{L_{\min}}^{\infty} \int_{L_{\min}}^{\infty} L_1^i L_2^j n(L_1, L_2, \tau) dL_1 dL_2 \quad (2.33)$$

In order to capture the features of the whole population, both the number and volume based average L_1 and L_2 are used, while $\sigma_{1,N}$ and $\sigma_{2,N}$, which are the number based variance of the distribution in directions L_1 and L_2 respectively, can be used as a validation of the capability of the model of correctly describing the whole particle size and shape distribution. Table 2.1 reports the equations and the moments required to evaluate all the described quantifiers.

2.3 MATERIALS AND METHODS

2.3.1 Materials

Deionized and microfiltered (pore size of the filter 0.22 μm) water was obtained using a Milli-Q Advantage A10 device (Millipore, Zug, Switzerland). L-Glutamic acid monosodium salt mono-hydrate (NaGlu, Sigma Aldrich, Switzerland, purity $\geq 99\%$), hydrochloric acid (HCl, Sigma Aldrich, Switzerland, $\geq 37\%$) and L-Glutamic acid ($\text{C}_5\text{H}_9\text{NO}_4$, Sigma Aldrich, Switzerland, purity $\geq 99\%$) were used as delivered. Ethanol (EtOH, Merck KGaA, Darmstadt, Germany, purity $> 99.5\%$) has been used as delivered. L-Glutamic acid exhibits two known polymorphs that can form in water, the metastable

α form and the thermodynamically stable β form, which are monotropically related.⁵⁴ As reported by Pertzoff,⁵⁵ the solubility of L-Glutamic acid in ethanol is extremely low, being approximately 0.06 grams per kilogram of ethanol.

2.3.2 Experimental setup

A scheme of the setup used to carry out the milling experiments is reported in Figure 2.3. The plant consists of a crystallizer, a rotor-stator wet mill (IKA Magic Lab) equipped with the MK/MKO module, and a filtration funnel. The crystallizer, a jacketed glass vessel with a volume of 2 liters, is equipped with a thermostat for the control of the temperature of the suspension. A peristaltic pump allows to precisely set the flow rate of the suspension through the mill. The grinding chamber is also equipped with a thermostat to avoid changes in the temperature of the flowing suspension. A vacuum filter, operated continuously throughout the experiment, is placed immediately after the outlet section of the grinding chamber in order to filter and recover the particles, thus minimizing the risk of possible undesired dissolution.

2.3.3 Measurement tools

In order to quantitatively measure the particle size and shape distribution, the μ -DISCO, an optomechanical setup, has been used for the analysis of the final powder. The setup consists of two cameras, that can capture pictures with a frame rate ranging from 5 fps to 75 fps, arranged in an orthogonal

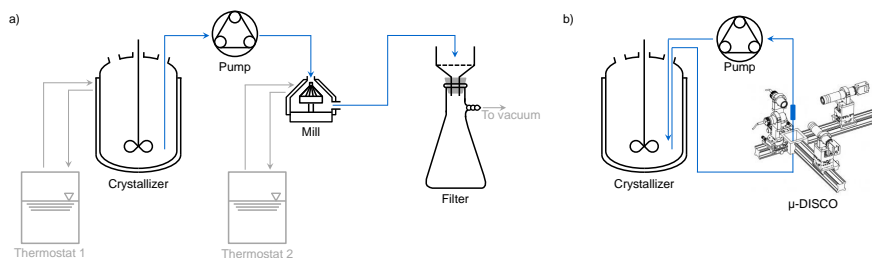


FIGURE 2.3: In panel (a), a sketch of the setup used throughout the experimental campaign is shown. Panel (b) shows a skematization of the measurement setup.

configuration. The suspension of crystals flows in a quartz channel placed between the two cameras. The use of this device, described in details by Rajagopalan et al.,⁵¹ allows for the reconstruction of multi-dimensional particle size and shape distributions starting from two orthogonal projections of the same object. The crystals, whose size spans from 10 to 2,000 μm , are subsequently classified, based on their reconstructed volume, into different classes. The classification in the needle and cuboid classes is based on the covariance-sphericity, $C_\lambda = L_3/L_1$ and the covariance-linearity, $F_\lambda = (L_1 - L_2)/L_1$, with a threshold of approximately 0.1 and 0.78 respectively. In the case of needles, $L_3 = L_2$. In this work, only the classes of needles and cuboids are considered for the reconstruction of the particle size and shape distribution of the ensemble of crystals. The cuboid particles, originally measured using three characteristic dimensions, are described as needles exploiting their volume and biggest dimension to evaluate the corresponding L_1 and L_2 values. The choice of neglecting the remaining classes for the reconstruction of the particle size and shape distribution in this case stems from the evidence that, due to the absence of types of particles other than needles and cuboids, as confirmed by visual inspection, the appearance of objects of different nature in the shape analysis must be considered an experimental artifact. The μ -DISCO device allows to measure and characterize around 30,000 crystals within a measurement interval of fifteen minutes.

Due to the high velocity of the fluid inside the channel, leading to blurred images, associated with the flow rate of 0.98 L/min used throughout the experimental campaign, measurements are performed offline using a suspension prepared mixing 1000 g of saturated ethanol solution and 1 g of crystals. A schematic of the measurement setup is reported in Figure 2.3 (b).

2.3.4 Preparation of seed crystals

The experimental activity described in this work involves the use of different populations of crystals, for a total of six different starting distributions of particles.

The first population of crystals (Seeds 1) consists of L-Glutamic acid seeds produced by pH-shift transformation, according to the procedure illustrated by Scholl et al..⁵⁶ A different population of L-Glutamic acid crystals (Seeds 2) has been obtained by combining equal weight amounts of crystals belonging to population Seeds 1 milled at 5,000 rpm, 10,000 rpm,

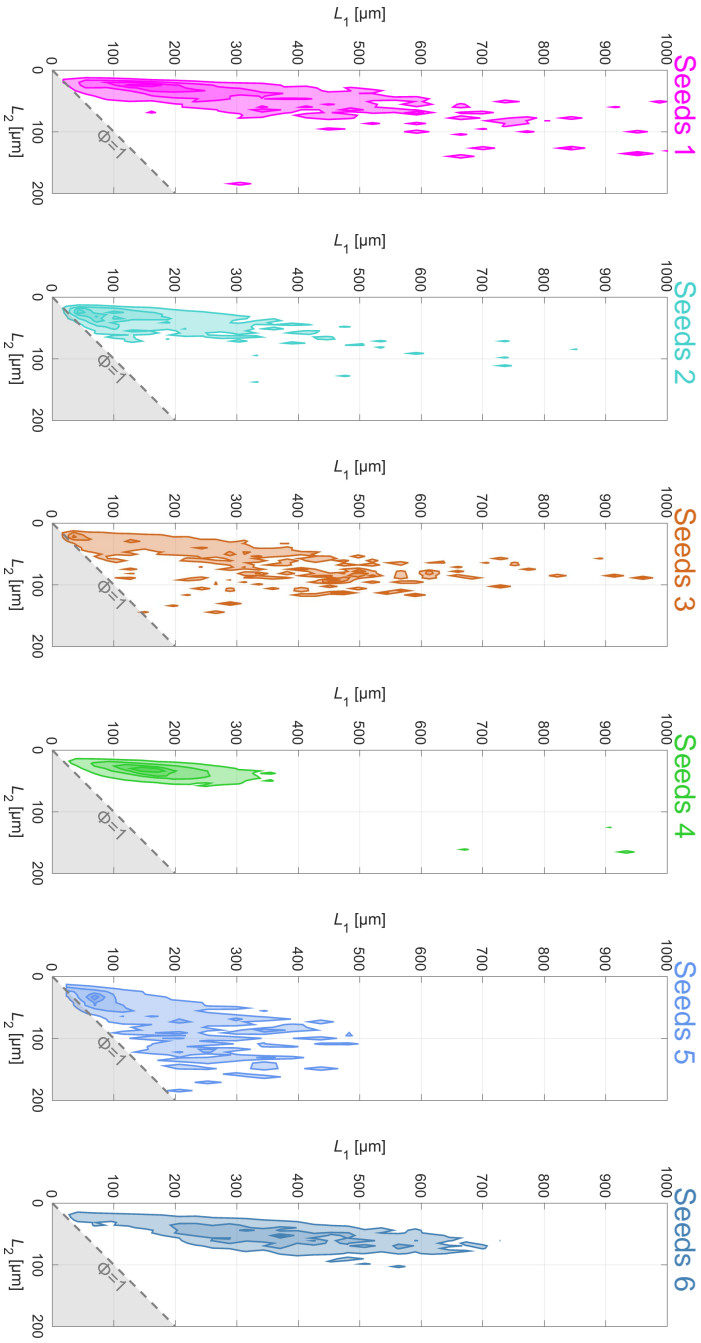


FIGURE 2.4: Particle size and shape distribution of the six populations of crystals used as seeds during the experimental activity.

15,000 rpm, 20,000 rpm, and 25,000 rpm. Seeds 3 have been obtained by growing the seeds obtained via pH-shift transformation by slowly cooling a suspension of crystals (suspension density: 15 g/kg_w) from 50 °C to 25 °C. A fourth population (Seeds 4) has been produced by applying three temperature cycles to the crystals of population Seeds 1. A mass of 102.1 g of crystals have been added to 1,979.6 g of a saturated solution of β L-Glutamic acid in water at 25 °C. For each cycle, the suspension is heated to 30 °C at a rate of 0.1 °C/min and kept at the final temperature for 3 hours. The suspension is then cooled back to 25 °C at the same rate and kept at the final temperatures for 12 hours. An additional population of crystals (Seeds 5) has been produced by suspending 40 grams of Seeds 1 crystals per kilogram of water in a saturated solution of LGA in water at 50 °C. The suspension is heated to 52 °C at a rate of 0.1 °C and after three hours cooled to 47 °C at the same rate. After 14 hours the cycles are performed two more times until the suspension is cooled to 25 °C at 0.1 °C/min. After 14 hours the crystals are filtered. For all the different processes described above, the final products have been filtered and dried in an oven at 45 °C for 24 hours. The last seed population (Seeds 6) has been obtained by sieving Seeds 1 (mesh grid 90 μ m) and keeping the finer fraction. Figure 2.4 shows the different particle size and shape distributions for each of the seed population produced according to the methods described above.

2.3.5 *Experimental protocol for breakage experiments*

A saturated solution of β L-Glutamic acid in ethanol is prepared by addition of an excess of solute in the crystallizer at a temperature of 25 °C. The solution is filtered after 24 hours and approximately 1 kg of it is replaced in the crystallizer at 25 °C. Crystals of the desired population of seeds are then added in order to obtain a suspension with the desired density, varying between 0.25 % (typical of very soluble drugs) and 5 % (typical of industrial processes). The tubes and the grinding chamber are filled with clear ethanol solution. The mill is then turned on, so that its speed is constant and at the desired value. Subsequently the slurry is pumped from the crystallizer through the mill at the maximum flow rate provided by the pump, namely 0.98 L/min, so as the residence time in the grinding chamber τ is 5.16 s. The milling device is equipped with a dedicated thermostat to allow for an accurate control of the suspension temperature, thus avoiding its possible rapid increment hence the undesired dissolution of crystals during grinding. The rotor speed is controlled as enabled by the manufacturer and

varied between 5,000 rpm and 25,000 rpm. The outlet stream is filtered in order to recover the ground crystals, that are subsequently dried in a ventilated oven at 45 °C for 24 hours.

2.4 RESULTS AND DISCUSSION

In the following, the results obtained in the course of a comprehensive characterization of the continuous wet milling process are reported and discussed. The first section deals with the experimental characterization of said stage, while the second part focuses on the modeling activity and its results. A third section deals with the validation of the fluid dynamics included in the model by direct comparison of simulation results and experimental measurements.

2.4.1 *Experimental characterization of the process*

The experimental campaign carried out in this work is aimed at characterizing the wet grinding process of β L-Glutamic acid by investigating different operating conditions and their impact on the process outcome. A first set of experiments has been performed in order to assess the experimental reproducibility. Then, two sets of tests have been run to investigate the effect of the suspension density and of the milling intensity on the final properties of the products. The analysis of the results presented in this section allows to get a deep understanding of the effect and importance of the different operating conditions, and it constitutes the basis for the validation of the model and the estimation of its kinetic parameters.

2.4.1.1 *Assessment of experimental repeatability*

In order to assess the repeatability of the experimental procedure, crystals from the population Seeds 1 and Seeds 2 have been milled at 5,000 rpm and 25,000 rpm respectively. The experiments have been performed two and three times and the conditions adopted are reported in Table 2.2, along with the corresponding results in terms of average size of the products. Figure 2.5 shows the particle size and shape distributions for each set of experiments. The small discrepancy between the average sizes and the overlapping of the different distributions demonstrates the repeatability of the experiments under different operating conditions.

Repeatability assessment					
Exp ID	τ [s]	θ [rpm]	m_{EtOH} [g]	m_{LGA} [g]	$\rho_s \left[\frac{g_{\text{LGA}}}{g_{\text{EtOH}}} \right]$
Seeds ₁	-	-	-	-	-
FIT ₁	5.16	5,000	970.0	9.68	1.00 %
FIT _{1R}	5.16	5,000	1000.17	10.01	1.00 %
Seeds ₂	5.16	-	-	-	-
FIT ₁₀	5.16	25,000	870.15	8.71	1.00 %
FIT _{10R}	5.16	25,000	858.93	8.83	1.03 %
FIT _{10B}	5.16	25,000	735.76	7.65	1.04 %

TABLE 2.2: List of the experiments and the corresponding operating conditions used to assess experimental repeatability

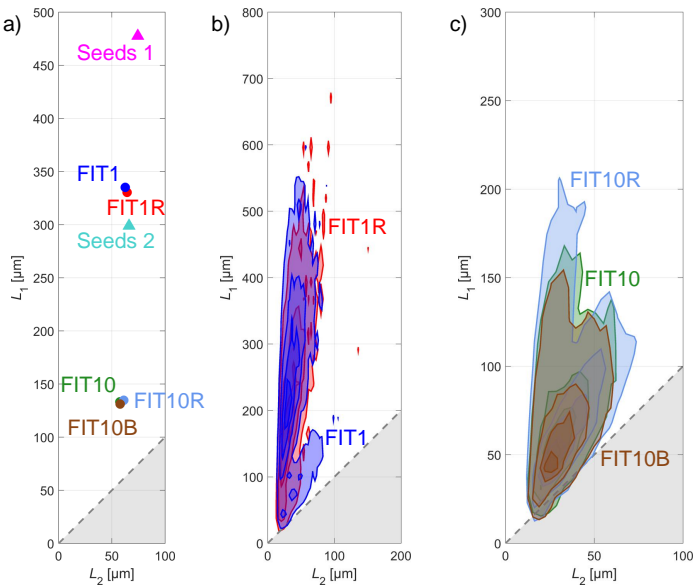


FIGURE 2.5: Experimental results obtained during the campaign aimed at assessing repeatability. In panel (a), the volume-weighted average sizes of the seeds (triangles) and the products (circles) are shown. Panels (b) and (c) show the comparison among the different particle size and shape distributions for the two subsets of experiments.

2.4.1.2 *Effect of suspension density*

As reported in Table 2.3, a series of experiments at different suspension densities, ranging from approximately 2 to 50 grams of crystals per kilogram of solvent, has been performed to check the possible influence on breakage of the mass of particles in suspension. The results of this first set of tests are illustrated in Figure 2.6, in terms both of average sizes and of PSSDs. The comparison highlights how the amount of mass suspended has no significant impact on the average size, as measured at the end of the experiment, since no clear trend could be observed. Furthermore, the overlapping of the distributions, reported for experiments MASS₁ and MASS₄, as well as for experiments MASS₅ and MASS₈, assesses the limited influence of this operating parameter within the range of values explored. In agreement with this observation, no effect of the mass suspended needs to be included in the constitutive equation for the breakage frequency.

Exp ID	Effect of mass suspended				
	τ [s]	θ [rpm]	m_{EtOH} [g]	m_{LGA} [g]	$\rho_s \left[\frac{\text{g}_{\text{LGA}}}{\text{g}_{\text{EtOH}}} \right]$
Seeds ₁	-	-	-	-	-
MASS ₁	5.16	5,000	952.2	2.48	0.26 %
MASS ₂	5.16	5,000	958.7	4.90	0.51 %
FIT ₁	5.16	5,000	970.0	9.68	1.00 %
MASS ₃	5.16	5,000	925.7	18.5	2.00 %
MASS ₄	5.16	5,000	950.1	46.8	4.92 %
MASS ₅	5.16	10,000	885.1	2.18	0.25 %
MASS ₆	5.16	10,000	898.5	4.55	0.51 %
FIT ₂	5.16	10,000	1001.75	10.06	1.00 %
MASS ₇	5.16	10,000	875.0	17.7	2.02 %
MASS ₈	5.16	10,000	852.1	42.9	5.03 %

TABLE 2.3: List of the experiments and the corresponding operating conditions used to investigate the effect of the suspension density

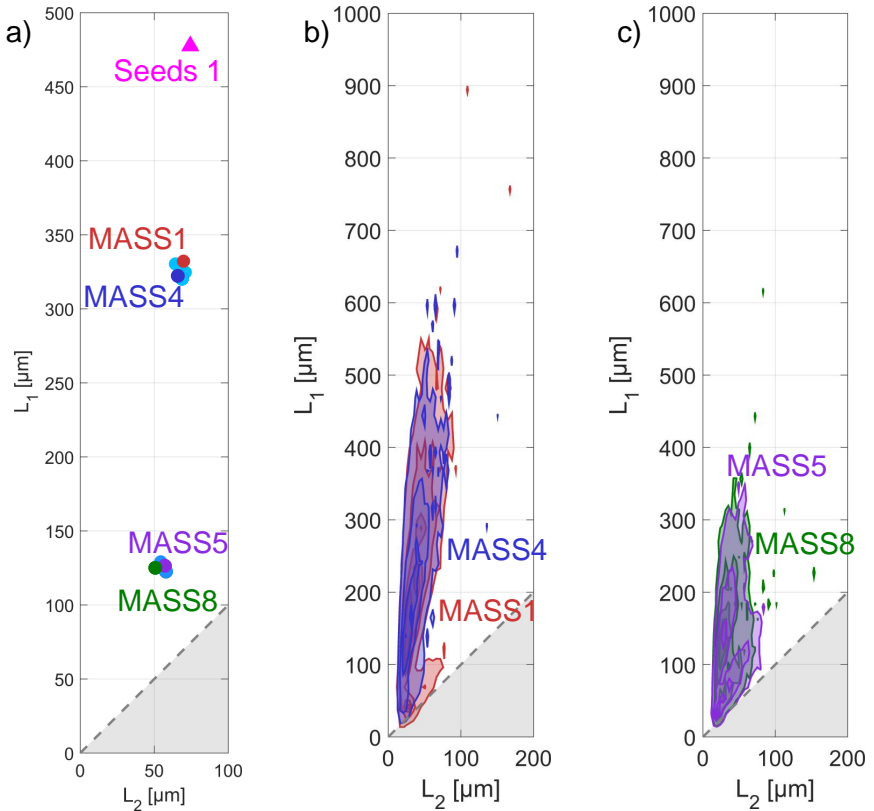


FIGURE 2.6: Results of the experimental campaign aimed at investigating the effect of the suspension density ρ_S on the properties of the final products. Panel (a) reports the volume-weighted average sizes of the seeds (fuchsia triangle) and of the powder obtained after milling (circles). Panel (b) and (c) show a comparison between the particle size and shape distributions of experiments MASS1 and MASS4 and experiments MASS5 and MASS8 respectively.

2.4.1.3 *Effect of milling intensity*

Table 2.4 reports the set of 5 experiments used to investigate the effect of the rotor speed θ , in the range from 5,000 to 25,000 rpm, on the final product properties. The results of this experimental campaign are illustrated in Figure 2.7.

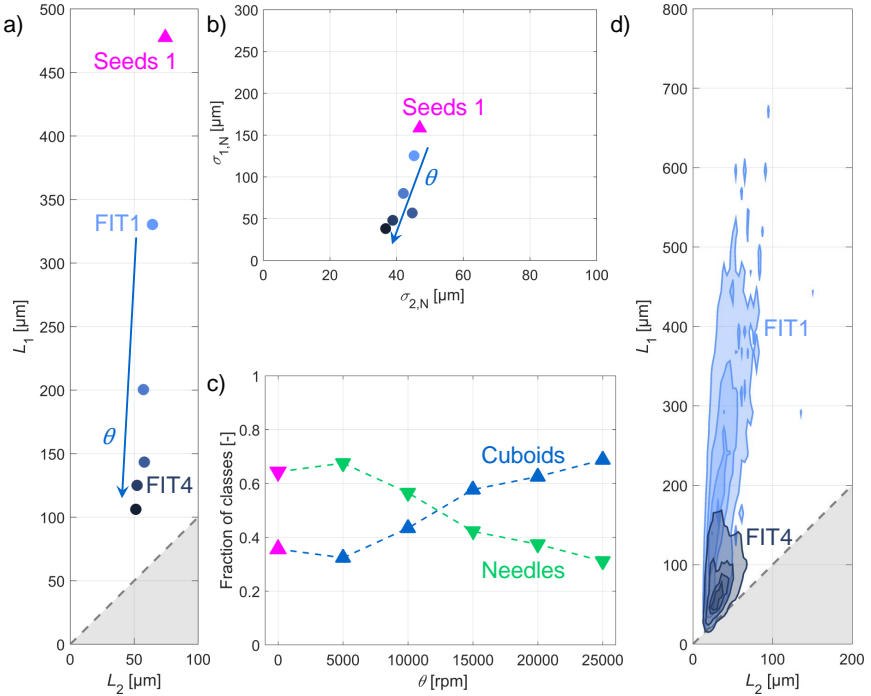


FIGURE 2.7: Results of the experimental campaign aimed at investigating the effect of the rotor speed θ on the properties of the final products. Panel (a) shows the volume-weighted average sizes of the seeds (fuchsia triangle) and of the powder obtained after milling (circles). The rotor speed increases along the direction identified by the arrow and stressed by the increasing darkness of the markers. Panel (b) reports the corresponding variances of the populations for each experiment. In (c) the fraction of particles classified as cuboids and needles is shown as a function of the rotor speed θ ($C_\lambda=0.1$). Finally, panel (d) reports the comparison between the particle size and shape distributions for experiments FIT1 and FIT4.

Effect of rotor speed θ and fitting experiments						
Seeds	Exp ID	τ [s]	θ [rpm]	m_{EtOH} [g]	m_{LGA} [g]	$\rho_s \left[\frac{\text{g}_{\text{LGA}}}{\text{g}_{\text{EtOH}}} \right]$
Seeds 1	FIT1	5.16	5,000	970.00	9.68	1.00 %
Seeds 1	FIT2	5.16	10,000	1001.75	10.06	1.00 %
Seeds 1	FIT3	5.16	15,000	987.40	9.95	1.01 %
Seeds 1	FIT4	5.16	20,000	951.20	9.69	1.02 %
Seeds 1	FIT5	5.16	25,000	934.50	9.65	1.03 %
Seeds 2	FIT6	5.16	5,000	925.81	9.37	1.012 %
Seeds 2	FIT7	5.16	10,000	786.13	7.88	1.00 %
Seeds 2	FIT8	5.16	15,000	788.35	7.88	1.00 %
Seeds 2	FIT9	5.16	20,000	808.53	8.10	1.00 %
Seeds 2	FIT10	5.16	25,000	870.15	8.71	1.00 %
Seeds 3	FIT11	5.16	5,000	669.70	6.73	1.00 %
Seeds 3	FIT12	5.16	10,000	656.10	6.58	1.00 %
Seeds 3	FIT13	5.16	15,000	646.60	6.53	1.01 %
Seeds 3	FIT14	5.16	20,000	726.30	7.31	1.00 %
Seeds 3	FIT15	5.16	25,000	713.70	7.20	1.01 %
Seeds 4	FIT16	5.16	5,000	824.26	8.24	1.00 %
Seeds 4	FIT17	5.16	10,000	806.53	8.25	1.02 %
Seeds 4	FIT18	5.16	15,000	784.75	7.88	1.00 %
Seeds 4	FIT19	5.16	20,000	845.20	8.77	1.04 %
Seeds 4	FIT20	5.16	25,000	840.95	8.67	1.03 %

TABLE 2.4: List of the experiments and the corresponding operating conditions used to investigate the effect of the rotor speed and to estimate the kinetic parameters

In Figure 2.7 (a) the effect of increasing rotor speed θ on the average sizes of the products is shown. The reduced variation in the average width L_2 in comparison with that of the length L_1 suggests that crystals are mainly broken lengthwise. In Figure 2.7 (b) the evolution of the broadness of the distribution along L_1 and L_2 is shown for the different experiments. For increasing values of θ , the particles not only attain a more compact morphology, but they also become more uniformly distributed with reduced variation between their sizes. This evidence is supported also by Figure 2.7 (c), where an increment in the fraction of cuboids and a decrease in the percentage of needle-like crystals can be observed. Finally, Figure 2.7 (d) shows a comparison between the whole particle size and shape distribution for experiments FIT1 and FIT4, through a more comprehensive visualization of the effects above. This analysis on the effect of the rotor speed is of great importance, since the model should be able to capture each of the characteristic trends emerged in this set of experiments.

2.4.2 Model validation

In this section, the results obtained during the previous experiments are combined with new sets of experimental runs to create a large and robust training data set for the estimation of all model parameters. By using the procedure reported in Section 2.2.4.1, it is possible to assess the validity of the model and subsequently use it for quantitative prediction of process outcome and for process control.

2.4.2.1 Estimation of model parameters

All the kinetic parameters appearing in Equations 2.13 and 2.14 can be estimated by fitting the simulations results to the experimental data. For the sake of simplicity, in the following, physically sound values are imposed to some of the parameters by considering general mechanical properties of the milling device and of the crystals. Therefore only a subset of the original kinetic parameters needs to be estimated via minimization of the error function defined by Equation 2.27.

PARAMETERS CHOSEN VIA THEORETICAL CONSIDERATIONS As discussed in Section 2.2.2.1, parameters p_{13} and p_{23} account for the fact that crystals cannot be ground below a certain size, i.e. they represent the grinding limit. Despite the general consensus on the existence of such limit, experimental evidence thereof is rather scarce. This size depends on the

properties of the crystalline structure⁵⁷ as well as on the type of device used. As reported by Luciani et al.,⁵⁸ in the case of the IKA Magic Lab device used in this work the grinding limit is approximately 30 μm . To assess this, we also performed a test where crystals from population Seeds 1 were milled for 24 h at 26,000 rpm. The average of the mean sizes obtained at the end of this experiment was approximately 29 μm (detailed results are here not shown for the sake of brevity), in line with what observed in the cited work. A reference rounded value of 30 μm has therefore been used in this work, also considering the variability among the available data.

Rather than considering the mechanical properties or the complex and imperfect crystalline structure of the crystals, a physically-sound value for parameters p_{14} and p_{24} can be obtained through considerations involving the angular mass of the particles. Figure 2.8 shows two cylinders, and for each of them the axes corresponding to the two characteristic dimensions are highlighted. The moment of inertia is proportional to the mass of the particle and is an indication of how the mass is distributed around the considered axis. Since the breakage of the particle in the grinding chamber of a continuous rotor-stator wet mill occurs due to particles being accelerated and pressed through the tight gap between the rotor and the stator, the angular mass can be used to determine whether this mechanism is more likely to break the particle along one or the other axis. More specifically, when the crystal lattice is isotropic, the cleavage occurs on a

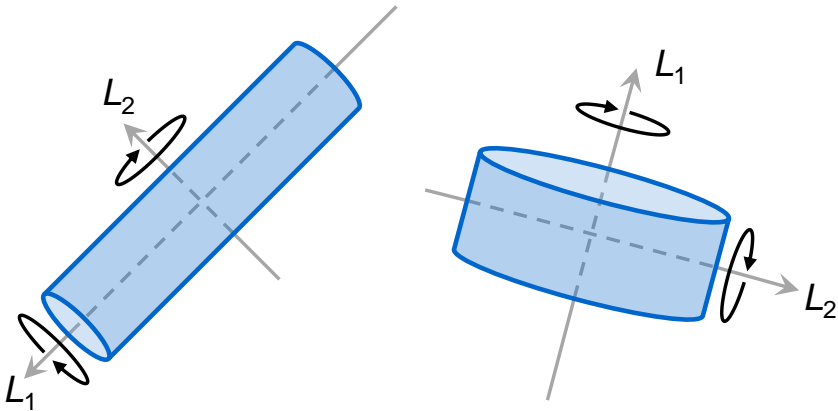


FIGURE 2.8: Example of two cylinders with their corresponding axes of inertia as considered in this work.

plane perpendicular to the axis whose angular mass is smaller. By enforcing the condition:

$$I_{L_1} = \frac{1}{2}mL_2^2 = \frac{1}{12}m(3L_2^2 + L_1^2) = I_{L_2} \quad (2.34)$$

where m is the mass of the cylindrical particle, one obtains a value for the aspect ratio $\Phi = L_1/L_2$ at which the two angular masses are the same along the two directions, namely $\Phi = \sqrt{3}$. In order to obtain the same values of h_1 and h_2 for $\Phi = \sqrt{3}$, one must choose $p_{14} = p_{24} = \Phi = \sqrt{3}$. Concerning the daughter distribution, since in the mill used throughout the experimental campaign breakage can occur due to both attrition and cleavage, the model for uniform fracture defined by Equation 2.20 has been adopted for both characteristic dimensions.

PARAMETER ESTIMATED VIA ERROR MINIMIZATION In order to quantitatively estimate the kinetic parameters p_{11} , p_{21} , p_{12} , and p_{22} the set of experiments reported in Table 2.4 has been performed. For each experiment, the particle size and shape distribution of the products has been measured and the average sizes have been calculated. The results are reported in Figure 2.9, where the experiments have been concatenated for a better visualization. Here, the triangles, representing specific average properties of the seeds as calculated by the grinding model using the estimated parameters, are stacked over the circle corresponding to the properties of the products at the end of the experiment reported on the horizontal axis. For each batch of seeds, five experiments, identified by the same background color in the different panels, have been performed at different milling intensities ranging from 5,000 rpm to 25,000 rpm. Figure 2.9 shows in panels (a)-(d) the number- and volume-weighted average sizes used for the fitting, while in panels (e) and (f) shows the number-weighted broadness of the particle size and shape distribution in direction L_1 and L_2 respectively. The latter quantities are not used for the parameter estimation but can be used as indicators of the model capability of fitting the population of crystals as a whole. As it can be seen in the plots, the experimental measurements are satisfactorily described.

The simulated number-weighted average width L_2 exhibits a maximum when the rotor speed θ increases, which is an unexpected behavior. This evidence can be justified considering that the daughter distribution for L_2 does not guarantee the conservation of the total width of the particles, in line with the type of measurement collected with the μ -DISCO. The presence of

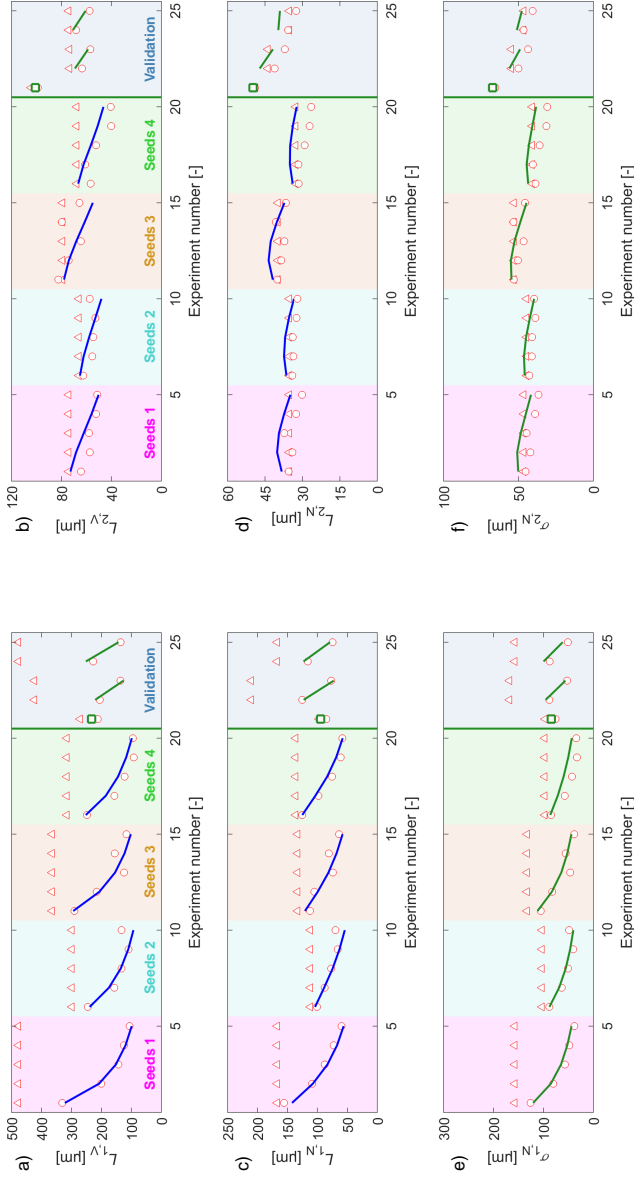


FIGURE 2.9: Results of the experimental campaign aimed at estimating the kinetic parameters of the developed model. The experiments are divided in five subsets, four of which used for parameter fitting (Seeds 1 to Seeds 4) and one for prediction (Validation). The red triangles represent the seeds used both for the experiments and as an input to the model. The red circles correspond to the average sizes of the products as measured by the μ -DISCO. The solid lines represent the outcome of the model in the optimum at the end of the fitting procedure. The green squares correspond to the results of the model simulations in the fully predictive mode. Panels (a) and (b) show respectively the volume-weighted average length and width. In panels (c) and (d) the number-weighted average sizes are plotted. Finally panels (e) and (f) report the number-weighted variances for both characteristic dimensions.

this maximum, however, cannot be easily verified experimentally, because the difference between maximum and average L_2 value is very small, namely of the same order of magnitude of the error committed when measuring the size of the crystals, i.e. $1 \mu\text{m}$.

Particularly interesting are the results reported in Figure 2.9 (e) and (f) concerning the broadness of the distribution. This average quantity is in fact not used to estimate the kinetic parameters, but the fitted average sizes appear in its defining equation. Nevertheless, since also moments of higher order not appearing in the objective function are used to evaluate the variance of the distribution, this property can be used as a first indicator of the possibility of fitting the whole population using only the four average sizes. Given the good agreement between the simulated values and the experimental ones, the use of the average length and width alone to capture the whole population can be considered as a satisfactory solution.

Figure 2.10 shows, as blue circles in (a), the sizes of all the particles that have been measured before and after milling. Such a plot helps in identifying the range of sizes L_1 and L_2 , over which the model parameters have been estimated and should be regarded as accurate. In particular, the corresponding size and shape training region has been highlighted with the light blue area corresponding to the convex hull of the cloud of points experimentally observed. In panel (b) a visualization of how particles of size L_1 and L_2 are more prone to fracture is provided. The breakage frequencies K_1 and K_2 can be seen as the two components of a vector \mathbf{K} , representing the breakage velocity along the corresponding characteristic sizes. In agreement with this definition, the stream lines, which are instantaneously tangent to the breakage vector \mathbf{K} , are reported, thus providing an indication of how, given the sizes of a particle, a crystal is expected to break and thus how its morphology is expected to change. In the region corresponding to both L_1 and L_2 below $100 \mu\text{m}$, the streamlines are converging to a single line and then approaching zero.

Table 2.5 reports the estimated values of parameters p_{11} , p_{12} , p_{21} , and p_{22} along with the corresponding 95% confidence intervals. The uncertainties on these parameters are reduced, but the ones for the kinetic parameters of the breakage frequency K_2 are larger than those on parameters p_{11} and p_{12} . This evidence can be justified considering the size data available for L_2 and used for fitting. As shown in Figure 2.10 (a), the range exploited is 10 to $50 \mu\text{m}$, which has a considerably low variability when compared to that investigated in the case of L_1 . Furthermore, the value of the grinding limit in the real milling device and that used in the model are of the same

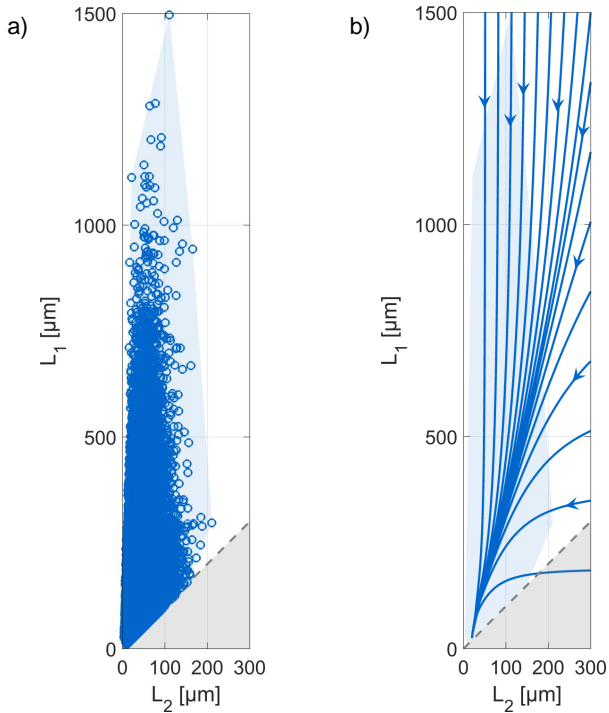


FIGURE 2.10: Range of validity of the estimated parameters. In panel (a), the sizes of each one of the particles measured during all the performed experiments is reported as a blue circle, with the resulting convex hull corresponding to the pale-blue region, which should be regarded as the validity range of the estimated parameters. Panel (b) shows the streamlines for the breakage vector \mathbf{K} in the $L_1 L_2$ -plane, highlighting, for each combination of characteristic sizes, how likely it is to break a particle along one of its axis.

order as magnitude of the width of the crystals milled, thus leading to small variations in L_2 hence to more uncertainty in its estimated value.

Parameter values and 95% confidence intervals	
Parameter	Estimated value
$p_{11} \left[\frac{\text{s}}{\text{kg}\cdot\text{m}^2} \right]$	16.06 ± 0.04
$p_{12} [-]$	1.907 ± 0.001
$p_{21} \left[\frac{\text{s}}{\text{kg}\cdot\text{m}^2} \right]$	105.06 ± 6.90
$p_{22} [-]$	1.964 ± 0.026

TABLE 2.5: Estimated values for the kinetic parameters and their confidence intervals

MODEL VALIDATION Figure 2.9 reports five verification experiments. The verification experiments have been performed by using both completely new populations of crystals, namely populations Seeds 5 and Seeds 6, under operating conditions previously adopted in the fitting experiments, as well as crystals from population Seeds 1 milled with new values of rotor speed chosen within the range explored previously, i.e. 5,000 rpm to 25,000 rpm (see Section 2.4.1.3). Table 2.6 reports the detailed conditions applied for this set of five runs. The model adopting the set of parameters identified through fitting can correctly describe the average sizes of the ground crystals, hence enabling the use of the model for prediction. Figure 2.11 shows the experimental and simulated populations for experiments VER2 and VER4 in panel (a) and (b) respectively. In both cases the good overlapping between simulated and experimental populations confirms the excellent predictions granted by the developed model, which is therefore capable of capturing the complex features of the particle size and shape distributions and of its evolution. In order to obtain a quantitative estimation of the quality of the predictions, the mean absolute error for each of the fitted average quantities and for each set of experiments is reported in Figure 2.12. For all of the four average sizes, the mean absolute error for the prediction experiments is in the same order of magnitude of that committed during fitting, thus demonstrating the good quality and reliability of the model also for predictions.

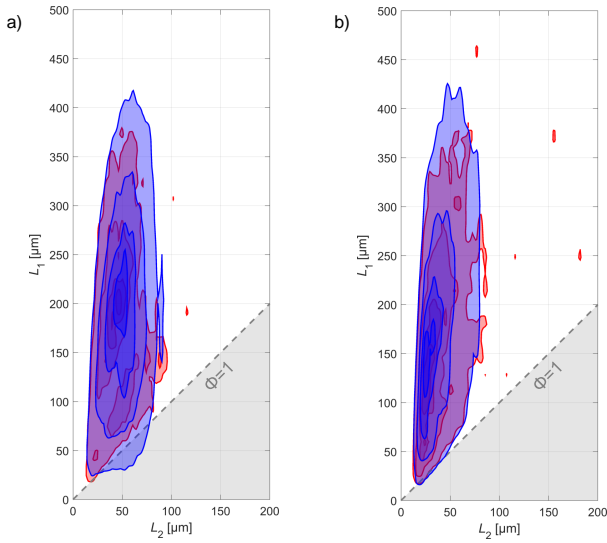


FIGURE 2.11: Comparison among the particle size and shape distribution obtained by simulations (blue) and experimentally (red) for experiments VER2 and VER4.

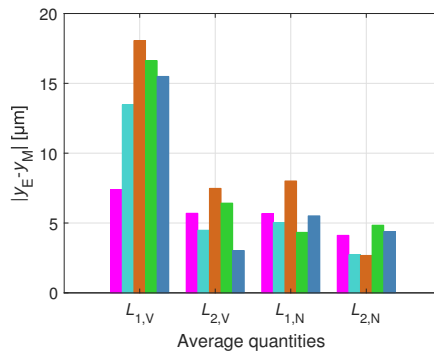


FIGURE 2.12: Histogram plotting the difference among the simulated and experimental fitted quantity for the fitting and validation experiments. Each bar corresponds to each one of the five subsets identified in Figure 2.9 (Seeds1 = fuchsia, Seeds2 = cyan, Seeds3 = orange, Seeds4 = green, Validation = blue).

Effect of rotor speed θ and verification experiments						
Seeds	Exp ID	τ [s]	θ [rpm]	m_{EtOH} [g]	m_{LGA} [g]	$\rho_s \left[\frac{g_{\text{LGA}}}{g_{\text{EtOH}}} \right]$
Seeds 5	VER1	5.16	25,000	840.95	8.67	1.03 %
Seeds 6	VER2	5.16	10,000	716.60	7.20	1.00 %
Seeds 6	VER3	5.16	20,000	702.30	7.12	1.01 %
Seeds 1	VER4	5.16	8,000	628.39	6.35	1.01 %
Seeds 1	VER5	5.16	17,000	637.00	6.40	1.00 %

TABLE 2.6: List of the experiments and the corresponding operating conditions used for model validation

2.4.2.2 Prediction of the fraction of needles and cuboids

The results obtained throughout the experiments reported in Table 2.4 have also been exploited to identify a value for the aspect ratio to discriminate among cuboids and needles in the simulation results. Each one of the 1,383,017 particles measured by the μ -DISCO was used as a basis for training a decision tree model to distinguish the two crystal classes. In particular, the covariance-sphericity $C_\lambda = 1/\Phi = L_2/L_1$ in combination with the *fitctree* Matlab function was used to generate a decision tree model from the provided set of data. For more details about the procedure used, the readers can refer to Rajagopalan et al.⁵¹ The only node identified by the algorithm corresponds to $C_\lambda = 0.39$, the threshold below which a particle is considered to be a needle and above which the crystal is assumed to be a cuboid. The measured particles are then reclassified according to this criterion and the resulting confusion matrix is reported in Figure 2.13 (a). Each row of the matrix represents the number of crystals assigned by the algorithm to a specific particle morphology, while each column represents the actual habit of the same object as identified by the μ -DISCO. The name is due to its immediate visualization of the cases where the algorithm confuses two classes.⁵⁹ The elements on the main diagonal of this matrix, highlighted in green in Figure 2.13 (a), represent particles whose morphology is correctly identified by the model. As it can be seen, the error committed by the classification method is acceptable, namely only 6.4 % of all the measured crystals is wrongly classified.

The value of $\Phi = 1/C_\lambda \approx 2.5$ is subsequently used to estimate the number of cuboids and needles obtained at the end of each simulation;

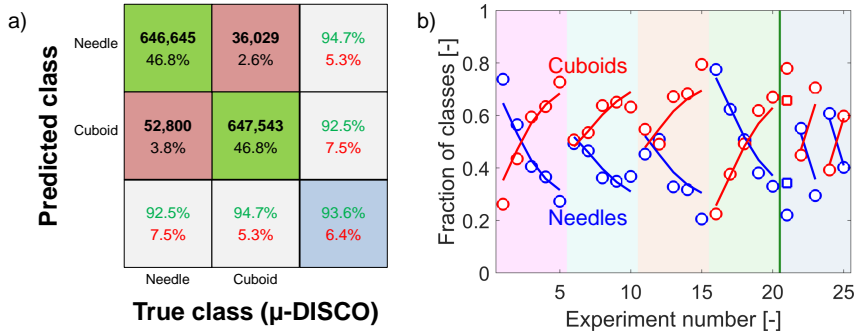


FIGURE 2.13: In panel (a), the confusion matrix obtained by construction of a decision tree based on 1,383,017 particles measured is reported. In panel (b) the comparison between model prediction (solid lines and squares) and experimental results (circles) for the fraction of needle (blue) and cuboid (red) classes in each of the experiments is reported.

the corresponding results are reported in panel (b) of Figure 2.13, where they are compared with the experimental data. It is clear how the model manages to correctly capture the trends describing the amount of particles belonging to the different classes. Despite the good quantitative agreement between the model and the experiments, in some cases, as for example experiments FIT₁₅ and VER₁, the discrepancy between the two is more than 15 % of the measured value. Nevertheless, the quantitative information obtained is of great interest, since it can provide an indication of whether the milling stage significantly impacted the shape of the crystals or whether its effect on the morphology of the particles was not relevant.

2.4.3 Effect of residence time

In this last part of the work, we focus on the effect of the residence time in the grinding chamber τ . By comparing the experimental measurements with the results of simulations performed using the parameters estimated in the previous section, we can assess once again the predictive performance of the model and verify the validity of the assumption about the fluid dynamics, on which the model is based. To this aim, four experiments have been performed under the conditions reported in Table 2.7. Figure 2.14 shows the number-weighted average length and width as a function of the residence time τ . As proven by the good agreement with the simulation outcome, the

model can predict both qualitatively and quantitatively the trends measured experimentally. Thus, the proposed model for the continuous rotor-stator wet mill can also be used as a tool to predict the outcome of grinding stages where different residence times in the milling chamber are applied, as well as a process where several grinding stages are performed in series or where more than a single passage in the mill is required. However, it is evident from the presented results, that residence times in the grinding chamber below five seconds have not been experimentally investigated. First, this limitation is a consequence of the maximum flow rate that can be applied by the volumetric pump in our experimental setup. Secondly, the flow rates required to achieve reduced residence times in the mill would be so high that crystals might be broken in an uncontrolled way by the pump itself and the results obtained would not be representative of the milling action only.

Effect of residence time					
Exp ID	τ [s]	θ [rpm]	m_{EtOH} [g]	m_{LGA} [g]	$\rho_s \left[\frac{\text{g}_{\text{LGA}}}{\text{g}_{\text{EtOH}}} \right]$
Seeds1	-	-	-	-	-
FIT3	5.16	15,000	987.4	9.95	1.01 %
TAU1	6.60	15,000	735.8	7.65	1.04 %
TAU2	7.92	15,000	732.0	7.49	1.02 %
TAU3	11.61	15,000	646.3	6.77	1.05 %

TABLE 2.7: List of the experiments and the corresponding operating conditions used to investigate the effect of the residence time

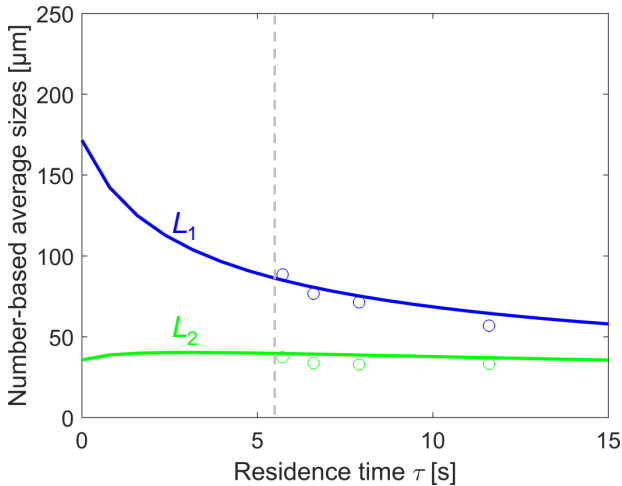


FIGURE 2.14: Results of the experimental campaign aimed at investigating the effect of residence time τ on the ground powders. The blue circle represent the experimental average size L_1 , while the green ones the average width L_2 . The blue and green solid lines correspond respectively to the simulated average length and width.

2.5 CONCLUSIONS

This work presents a comprehensive characterization of the grinding of β L-Glutamic acid crystals carried out using a commercially available continuous rotor-stator wet mill. The model of the process is based on a morphological population balance equation for which novel constitutive equations have been developed, considering not only the operating conditions at which the process is carried out, but taking also into account the characteristic geometric properties of the particles. These equations, based on the combination of empirical observation and physical concepts, can be used to describe the breakage of needle-like crystals, but can be extended to other compounds, morphologies, and types of mill by choosing the appropriate functional forms for the different terms of the breakage frequencies K_1 and K_2 . One of the main advantages of the proposed model is, in fact, the possibility of constructing a breakage frequency function as the product of three specific functions describing each characteristic feature of the breakage mechanism. Therefore the model can be tailored to describe different types of mills just by providing the correct formulation for the function

$o_i(\mathbf{z})$ in Equations 2.6 and 2.7, whereas the functions $f_i(L_i)$ and $h_i(\Phi)$, considering the geometrical properties of the crystals, can be reformulated in order to extend the application of the model to particles with different geometries. Both functions should be recast in order to correctly include the effect of the characteristic sizes of the different crystal morphologies (i.e. platelets, cuboids) to which the model should be extended, as well as the geometrical and morphological properties associated to their shape. Furthermore, in order to apply the model to compounds with significantly different mechanical properties, which are here embedded in parameters p_{11} and p_{21} , a dedicated function should be introduced. The results and the analysis reported in this paper can therefore be seen as a benchmark and starting point for the further development of a generally valid model capable of quantitatively describe the breakage of crystals with non-equant morphologies in a milling device.

In order to characterize the system and to develop a model for process design and control, an extensive experimental campaign consisting of different sets of tests, has been designed and performed. At first, an experimental characterization of the system for the thorough understanding of the effect of the operating conditions on the product properties, involving the repeatability and reproducibility assessment, has been carried out. The data set available has been expanded, eventually consisting of twenty-five runs performed with different seeds populations and under several operating conditions, and has been used to first estimate the kinetic parameters and to consequently assess the possibility of using the model in a predictive manner. Finally, the effect of the residence time has been investigated and exploited to validate the fluid dynamics assumptions on which the model relies. The morphological population balance, along with its constitutive equations, developed in this work proves to be a fundamental tool for the quantitative prediction of the properties of interest of the product crystals, thus constituting a milestone for a better understanding and characterization of continuous wet milling processes and a first step towards their optimal design and control, beyond the specific and successful case of β L-Glutamic acid studied in this work.

2.6 NOTATION

L_i	crystals characteristic dimension i	$[\mu\text{m}]$
n	number density function	$[\mu\text{m}^{-2} \text{kg}^{-1}]$
B	birth term in the PBE	$[\mu\text{m}^{-2} \text{kg}^{-1} \text{s}^{-1}]$
D	death term in the PBE	$[\mu\text{m}^{-2} \text{kg}^{-1} \text{s}^{-1}]$
K_i	breakage frequency for dimension i	$[\text{s}^{-1}]$
g_i	daughter distribution of the fragments along the i -th dimension	$[\mu\text{m}^{-1}]$
\mathbf{z}	vector of operating conditions	$[-]$
m_M	mass of the rotor	$[\text{kg}]$
r_M	average radius of the rotor	$[\text{kg}]$
\mathbf{p}	vector of breakage frequency parameters	$[\text{varies}]$
F	objective function	$[-]$
N_E	total number of experimental observations	$[-]$
N_O	number of considered outputs	$[-]$
y_i	characteristic property of the measured particle size and shape distribution for the i -th experiment	$[\mu\text{m}]$
$\hat{y}_i(\mathbf{p})$	characteristic property of the estimated particle size and shape distribution for the i -th experiment	$[\mu\text{m}]$
\mathbf{J}	Jacobian matrix of the model	$[\text{varies}]$
\mathbf{S}	measurement error covariance matrix	$[\mu\text{m}^2]$
\mathbf{V}	positive semidefinite parameter covariance matrix	$[\text{varies}]$
C_{ij}	confidence intervals for parameter p_{ij}	$[\text{varies}]$
$t_{1-\alpha/2}^{N-k}$	t -statistics with $N - k$ degrees of freedom with a confidence level α	$[-]$
$L_{1,N}$	number-weighted average length	$[\mu\text{m}]$
$L_{2,N}$	number-weighted average width	$[\mu\text{m}]$
$L_{1,V}$	volume-weighted average length	$[\mu\text{m}]$
$L_{2,V}$	volume-weighted average width	$[\mu\text{m}]$

τ	residence time in the mill	[s]
θ	rotor angular velocity	[rps]
Φ	aspect ratio	[-]
σ	standard deviation of the daughter distribution	[μm]
η	size of the mother particle	[μm]
$\delta(L_i)$	Dirac's delta function	[μm^{-1}]
ε	daughter distribution parameter	[μm]
μ_{ij}	cross moment ij of the PSSD	[varies]
ρ	density of the crystalline phase	[kg m^{-3}]
$\sigma_{1,N}$	number-weighted standard deviation in L_1 direction	[μm]
$\sigma_{2,N}$	number-weighted standard deviation in L_2 direction	[μm]

MANIPULATION OF PARTICLE MORPHOLOGY BY CRYSTALLIZATION, MILLING, AND HEATING CYCLES - A MATHEMATICAL MODELING APPROACH

3.1 INTRODUCTION

The ever-growing demand for high quality products and the strict requirements on solid formulations are nowadays driving more and more the interest of the crystallization community towards new aspects of the particulate processes. Basic properties of everyday commodities, especially those in powder form, do in fact strongly depend on the size and shape of the single particles. Especially in the pharmaceutical industry, the morphology of crystals is of crucial importance, due to its large influence on the bio-availability of the commercialized drugs, as well as on the processability of the intermediates. Several authors^{38,39,60,61} have in fact highlighted how the dimensions of the single crystals and their variability in terms of particle size distribution (PSD) affect the filterability of the powder obtained at the end of a crystallization stage.

A large effort has been therefore put in developing and designing techniques that would allow to control the shape of the crystals precipitated from solution. In particular, it is possible to identify two different types of approach, one aimed at directly controlling the morphology of crystals during crystallization and another aimed at changing the habit of the particles after the crystallization stage.

The use of different solvents, as well as additives, belongs to the first type of approaches.⁶²⁻⁶⁶ This technique relies on the molecular interactions at the basis of crystal growth. According to Wulff's rule in fact, crystal morphology is dominated by the facets exhibiting the lowest surface energy and the slowest growth. Since these characteristics are determined by the functional groups present at the solid interface, the modification of these properties by using engineered compounds can be exploited. Furthermore, the influence

Salvatori F. and Mazzotti M., Manipulation of particle morphology by crystallization, milling, and heating cycles - A mathematical modeling approach, *Industrial & Engineering Chemistry Research*, 2018, - (-), XXX-XXX.

of a third compound in solution can eventually hinder nucleation events. The strict specifications on product purity, particularly concerning pharmaceutical products, strongly limit the type of solvents and additives that can be used in the manufacturing of the active pharmaceutical ingredients. Traces of these compounds might be incorporated in the crystal lattice or might not be properly removed from the collected powder, resulting in their assimilation in the human body. In order to avoid the drawbacks related to the presence of undesired compounds in the crystallization environment, another applicable technique is based on the use of temperature cycles.^{67,68} Several studies have been performed to understand the effect of thermal cycles on the morphology of crystals and dedicated theories and mathematical models were also developed.⁶⁹ However, thermal cycles allow to reach an attainable region that might exclude the target size and shape relevant for the process under considerations.^{70,71}

For all these reasons, it is current industrial practice to intend shape manipulation as part of the downstream processes. Among the different unit operations subsequent to crystallization, milling is the one that is ubiquitously present. The size reduction is accomplished by inducing mechanical stress in the crystals and thus breaking them. For this reason, a wide variety of devices, ranging from jaw crushers to ball mills, has been developed to address the different process requirements. However, one of the typical drawbacks of milling is the undesired heating of solid particles, which could eventually lead to degradation and amorphization of the products.⁴¹ Wet milling devices are a solution to this problem; the particles are processed in suspension, reducing therefore the risk of large temperature changes. Furthermore, the shift from batch to continuous manufacturing promoted the development of continuous grinding devices. Nevertheless, the problem connected to the modification of crystal surface and structure has not completely been solved with the introduction of wet milling. Moreover, the formation of fine fragments during breakage is an additional drawback, since their presence in the final products has a strong and negative impact on compaction and filter cake properties.

In this theoretical work, a new process to control and manipulate crystal shape is proposed, analyzed, and discussed. Such a process is a combination of cooling crystallization with thermal cycles and intermediate milling. While the aim of the grinding step is that of directly manipulating the size and shape of crystals, the main objective of the cyclic dissolution and crystallization consists in the removal of fine and amorphous material to favor the growth of larger undissolved crystals. Since the focus is on

process synthesis and design, and not on a specific substance, a parametric analysis has been carried out using physically realistic data, rather than data applicable to a specific system (which are anyways not available in the literature). Estimating model parameters and validating the model through experiments are both beyond the scope of this work, but are part of a forthcoming research program.

This chapter is organized as follows. Section 3.2 introduces a possible combination of the three stages and a detailed description of the process, along with the goals of the single steps and those of the combined cycle. In Section 3.3 the mathematical model used to simulate the process is presented; this model allows to describe the key physical phenomena, occurring at the crystal scale, and at the same time to characterize both the single unit operations and the full process. The model is then used to perform a first assessment of the feasibility of the process and then a thorough study of the effect of different operating conditions on the product properties; the outcome of this investigation is extensively reported in Section 3.4. In Section 3.5 conclusions will be drawn.

3.2 CONCEPTUAL DESIGN

In this work we target the crystallization from solution of substances that typically crystallize with a needle-like shape. The approach to avoid needles is that of developing a combined crystallization, milling, and dissolution process aimed at producing more equant crystals. We consider a process, whose overall goal is to recover the crystallizing substance from a solution at high concentration and (relatively) high temperature, by using seeds and cooling the system to a low temperature. More specifically, there are two main objectives at two different scales. The first is defined at the particle scale and consists in obtaining more equant crystals, as well as to avoid the presence of amorphous material. In particular, the production of more equant crystals can be achieved both by increasing their width and by reducing their length. The second goal is defined for the ensemble of particles and consists in the production of a monodispersed powder, thanks to the removal of the undesired fines. Based on these considerations it is straightforward to design a process consisting of a repeated sequence of three steps, where the dissolution stage immediately follows the grinding step, where the fines are formed. Moreover, crystallization should be performed immediately before the grinding stage, since milling is the step aimed at controlling the shape of the crystals grown in the crystallizer. The very

first step in the process should be crystallization, by cooling of the initial saturated solution, which typically comes from an upstream synthesis stage. Concerning the very last stage of the process, both crystallization and dissolution could be considered, but not milling, as it would lead to the presence of fines in the product. In this work, crystallization is also used as the last process step.

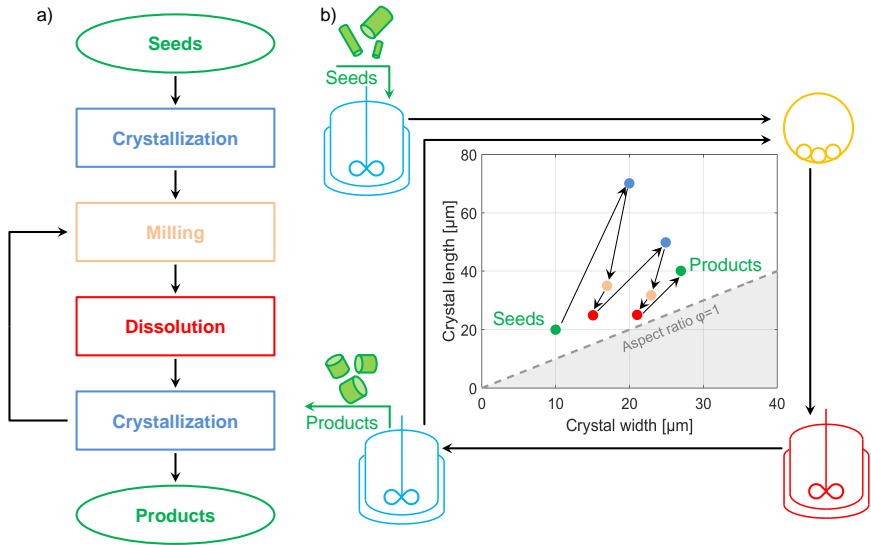


FIGURE 3.1: Visualization of the different stages involved in the process. In a) the block diagram shows the sequence of unit operations as performed during the 3-stage process. In b), the evolution of length and width of a crystal throughout a process consisting of three cycles is illustrated qualitatively to better highlight the objectives of the different stages and of the whole process.

Figure 3.1(a) shows a block diagram with the sequence of the unit operations as they are performed during the cycles. Once the main objectives and the structure of the process have been defined, it is necessary to determine the goals that should be achieved during each stage.

During crystallization, the objective is to increase the width of the crystals to the maximum extent allowed by mass and kinetic constraints. The occurrence of agglomeration, breakage, and nucleation phenomena should hence be avoided. To this aim, low cooling rates and reduced agitation are required. Moreover, seeds are added in the first crystallization stage,

to further avoid nucleation events. This choice of operating conditions, however, will not affect in any way the growth kinetics, hence it won't prevent crystals from growing as needles. The milling stage should directly manipulate the shape of the crystals by breaking them. Crystals should be broken mainly lengthwise to exploit at best the size reduction. Phenomena like attrition, which would lead to the formation of a large amount of fines, or fracture along the longest dimension are highly undesired, as their outcome significantly deviates from the desired objectives. Finally, dissolution should be performed so that the fines are completely dissolved, while the increase of solute concentration thus generated will be recovered in the following crystallization stage. Figure 3.1(b) shows the possible evolution of the average sizes of an exemplary particle throughout the cycles.

Once the process and its goals have been defined, a feasibility study is required to assess the potential of the proposed technology. A fast, yet thorough, screening of the process features and trends can be performed by mathematical simulations. The advantage of this approach lies in the possibility of reproducing the outcome of a large amount of experiments in a limited amount of time.

3.3 MATHEMATICAL MODEL

The process developed in this work involves different unit operations and several rather complex phenomena. The mathematical model stands out as a powerful tool for a thorough and fast investigation of the applicability of the technology. To accomplish this task, the model should be able to describe at the same time particle-scale phenomena as well as plant-scale unit operations. Another fundamental requirement is the capability of tracking the size and shape of the ensemble particles. Population balance equations (PBE) are the natural choice for the description of particulate processes. The flexibility of this model stems from the possibility of including fundamental phenomena and to adapt them to achieve an accurate description of the different unit operations. At the basis of the PBEs, irrespectively of the process described, lies the necessity of defining a model for the single crystals and their ensembles.

3.3.1 *Crystal model*

The crystalline structure of a particle, due to its complexity, has been object of several studies. In particular, the identification of models capable of

describing particles by means of a reduced number of parameters is of extreme interest. The use of convex polytopes is one of the available models for faceted, convex crystals.⁷² Despite the detailed rendition of particles morphology, the computational burden required to describe an ensemble of particles, each described with such level of detail, is too high for the simulation of entire processes.

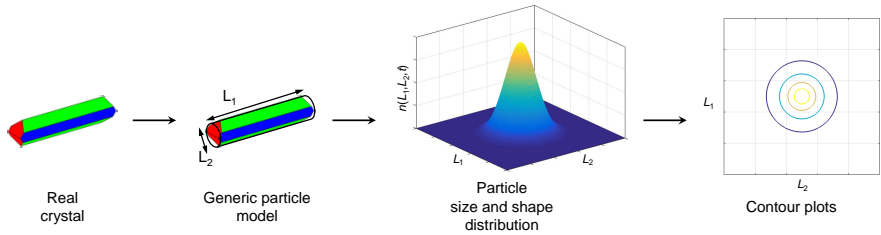


FIGURE 3.2: Visualization of the steps required to create a particle size and shape distribution starting from single crystals. The real, faceted, convex particle is approximated, according to the generic particle model, to a cylinder of length L_1 and width L_2 . Once these two quantities are evaluated for all the particles in suspension, the particle size and shape distribution is reconstructed by assigning each crystal to the discretized internal coordinates space. In order to better visualize the information in a quantitative manner, contour plots are used instead of a 3-D rendition of the surface. The isolines plotted in the L_1L_2 -plane represent the curves where the distribution attains a constant specific value.

A valid alternative is the generic particle model as proposed by Schorsch et al.²³ Particles are described by means of polyhedra, an approach that ensures reasonable accuracy with a reduced number of characteristic sizes. Furthermore, this allows for a less computationally intensive description of the ensemble of particles, a key feature for the model. In order to consider the morphology of a crystal, the minimum number of sizes that should be considered is two. For elongated particles, i.e. needle-like crystals, the reference shape chosen and adopted in this work is the cylinder, characterized by a length L_1 and a width L_2 , as illustrated in Figure 3.2.

Based on the value of the characteristic sizes of each crystal in the particles ensemble, it is possible to reconstruct the particle size and shape distribution of crystals, $n(L_1, L_2)dL_1dL_2$, which represents the number of particles with size $L_1 \in [L_1; L_1 + dL_1]$ and $L_2 \in [L_2; L_2 + dL_2]$ per unit mass of solvent. A convenient way to visualize particle size and shape distributions are

contour plots, in the L_1L_2 -plane, along which, the function $n(L_1, L_2)$ has a constant value. Four isolines are used in all the figures, in order to provide the necessary amount of information while allowing at the same time for easy readability.

3.3.2 Population balance equation

The generic formulation of a population balance equation for a well-mixed batch crystallizer is given by Ramkrishna[45].

$$\frac{\partial}{\partial t} n(t, \mathbf{x}) + \nabla_{\mathbf{x}} \cdot [\mathbf{G}(t, \mathbf{x}, \mathbf{z}) n(t, \mathbf{x})] = B(t, \mathbf{x}, \mathbf{z}) - E(t, \mathbf{x}, \mathbf{z}) \quad (3.1)$$

Here, $n(t, \mathbf{x})$ is the number density function representing the crystal population, defined on a set of internal coordinates \mathbf{x} , e.g. the characteristic sizes L_1 and L_2 , and \mathbf{G} is the vectorial field describing the rate of change of the internal coordinates, e.g. the growth rates, which is a function of the properties \mathbf{z} (temperature, supersaturation, pH, etc.) of the continuous phase surrounding the crystals. The terms $B(t, \mathbf{x}, \mathbf{z})$ and $E(t, \mathbf{x}, \mathbf{z})$ represent the birth and death of particles, respectively, due to breakage and agglomeration events. Obviously, the constitutive equations used to describe \mathbf{G} , B , and E depend also on the very nature of the crystalline material considered.

The population balance equation can be tailored to describe the different stages of the process by defining appropriate functional forms for the different terms appearing in Equation 3.1.

3.3.2.1 PBE for crystallization

Under the assumption of cylindrical particles and absence of agglomeration and breakage, the population balance equation for a well-mixed batch crystallizer can be recast as:

$$\frac{\partial n}{\partial t} + \frac{\partial (G_1 n)}{\partial L_1} + \frac{\partial (G_2 n)}{\partial L_2} = J \delta(L_1) \delta(L_2) \quad (3.2)$$

$$n(L_1, L_2, t = 0) = n_0(L_1, L_2) \quad (3.3)$$

The boundary condition of the partial differential equation will be discussed in Section 3.3.2.4. Nuclei are assumed to be point-like entities when they appear, therefore they are formed at a rate J with characteristic sizes $L_1 = L_2 = 0$, as to the right hand side of Equation 3.2. Equation 3.3 represents the initial condition of Equation 3.2, describing the population of

crystals at the beginning of the crystallization, that is either the particle size and shape distribution of the seeds in the case of the first cycle, or that obtained at the end of the dissolution step throughout the rest of the process. The population balance equation has to be coupled with a material balance for the solute in solution, which under the assumption of constant volume can be written as follows:

$$\frac{dc}{dt} = -k_V \rho \frac{d\mu_{12}}{dt} \quad (3.4)$$

$$c(t=0) = c_0 \quad (3.5)$$

In Equation 3.4 k_V represents the volume shape factor, which is equal to $\pi/4$ for cylinders, while ρ is the density of the solid phase; μ_{12} represents the cross moment of the particle size and shape distribution, according to the following general definition of the moments of a 2D distribution:

$$\mu_{ij}(t) = \int_0^\infty \int_0^\infty n(L_1, L_2, t) L_1^i L_2^j dL_1 dL_2 \quad (3.6)$$

The expression used to model the growth rate G_i depends on the prevailing growth mechanism. In the current work an empirical correlation is used.

$$G_i = k_{G,i1} \exp\left(-\frac{k_{G,i2}}{T}\right) (S-1)^{k_{G,i3}} \quad \text{with } S > 1 \quad (3.7)$$

S is the supersaturation, which, in the case of either mild non-idealities or negligible effect of the composition on the activity coefficient of the solute, is defined as the ratio between the concentration of solute in solution and its solubility at the temperature T :

$$S = \frac{c}{c^*(T)} \quad (3.8)$$

The nucleation term J must take into account primary, both homogeneous and heterogeneous, as well as secondary nucleation. Expressions for primary nucleation can be derived from the classical nucleation theory. Concerning secondary nucleation, given the uncertainties on its mechanisms,

different models have been proposed in the literature. In this work, the equation proposed by Mersmann⁷³ is used.

$$J = J_{\text{Sec}} + J_{\text{Hom}} + J_{\text{Het}} \quad (3.9)$$

$$J_{\text{Hom}} = k_{\text{Hom},1} \exp\left(-\frac{k_{\text{Hom},2}}{\ln^2 S}\right) \quad (3.10)$$

$$J_{\text{Het}} = k_{\text{Het},1} \exp\left(-\frac{k_{\text{Het},2}}{\ln^2 S}\right) \quad (3.11)$$

$$J_{\text{Sec}} = k_{\text{Sec},1} \epsilon^{k_{\text{Sec},2}} m_S^{k_{\text{Sec},3}} \bar{G}^{k_{\text{Sec},4}} \quad (3.12)$$

In Equation 3.12, m_S is the suspension density, \bar{G} is the average growth rate, calculated as $(G_1 + G_2) / 2$, while ϵ is the power input of the crystallizer evaluated as shown in Equation 3.13:⁵⁶

$$\epsilon = \frac{N_p d_1^5 \omega^3}{V} \quad (3.13)$$

Here, N_p is the power number for the impeller, which is equal to 0.6 in the case of a four blade impeller,⁷⁴ d is the diameter of the stirrer, ω its rotational speed and V the volume of the reactor.

Note that in the original work by Mersmann,⁷³ only particles described by a single characteristic length, L , were considered, hence the growth rate appearing in Equation 3.12 was defined unambiguously as $G = dL/dt$. In our case, and being consistent with the empirical character of Equation 3.12, we have made the empirical choice of using the arithmetic average to define \bar{G} in the used equation. With this, we are not claiming this is the perfect choice; however, we assume that such choice does not have a major impact on the results of the whole study.

3.3.2.2 PBE for milling

In the currently available literature, little is reported concerning morphological population balance equations for complex phenomena such as breakage and agglomeration.^{46,48,49} In the framework of the development and characterization of the 3-stage process, a mathematical model for the breakage, that could consider also the morphology of the particles, had to be created. The population balance equation for a continuous rotor-stator wet mill, which is described as a plug-flow tubular apparatus (i.e. under conditions of

perfectly segregated flow), operated at steady-state, under the assumption of constant temperature and supersaturation, reads as follows:

$$\frac{dn}{d\tau} = B_1 + B_2 - E \quad (3.14)$$

$$B_1 = \int_{L_1}^{\infty} K_1(x, L_2)n(x, L_2, \tau)g_1(L_1, x)dx \quad (3.15)$$

$$B_2 = \int_{L_2}^{\infty} K_2(L_1, y)n(L_1, y, \tau)g_2(L_2, y)dy \quad (3.16)$$

$$E = K_1(L_1, L_2)n(L_1, L_2, \tau) + K_2(L_1, L_2)n(L_1, L_2, \tau) \quad (3.17)$$

$$n(L_1, L_2, \tau = 0) = n_0(L_1, L_2) \quad (3.18)$$

Note that τ represents the residence time along the tubular apparatus, and that no material balance for the solute is needed (see Equation 3.4) because breakage does not impact the concentration in solution. Equation 3.15 describes the formation of fragments of size (L_1, L_2) due to the fracture of a longer parent crystal of size (x, L_2) , while Equation 3.16 is its equivalent in the L_2 direction. Equation 3.17 is used to describe the breakage of a crystal of size (L_1, L_2) . The terms $K_1(L_1, L_2)$ and $K_2(L_1, L_2)$ are the breakage frequencies, whose aim is to model the rate of breakage of the crystals. The functions $g_1(L_1, x)$ and $g_2(L_2, y)$ represent the daughter distributions, which are functions used to describe the size distribution of fragments formed in a specific breakage event.

The functional form adopted for the breakage frequency must take into account both the size and shape of the particles undergoing fracture, as well as being physically consistent with experimental evidence. The equations implemented in this work to model the breakage frequency are:

$$K_1 = k_{0,1}f_1(L_1)h_1(\Phi) \quad (3.19)$$

$$K_2 = k_{0,2}f_2(L_2)h_2(\Phi) \quad (3.20)$$

Such equation contains three different terms, each one of them allowing to take into account different characteristics of the grinding process. The factor k_0 is used to model the intensity of the stress applied to the particle leading to the breakage event, hence it takes into account the operating conditions under which the mill is operated. It is proportional to the energy provided by the mill to the liquid slurry, and a possible functional form for this quantity is reported in Equation 3.21.

$$k_{0,i} = k_{M,i1}(E_M)^{p_2} = k_{M,i1} \left(\frac{1}{2}m_M v^2 \right)^{k_{M,i2}} = k_{M,i1} \left(\frac{1}{2}m_M (\theta r_M)^2 \right)^{k_{M,i2}} \quad (3.21)$$

Here, m_M is the mass of the mill rotor, while θ and r_M are respectively its rotational speed and its radius.

The term $f_i(L_i)$ in Equations 3.19 and 3.20 is used to take into account the dependency of the breakage rate on the particle size, the position at which stress is applied and the grinding limit. The functional form proposed and adopted in this work is reported for both characteristic dimensions in Equations 3.22 and 3.23:

$$f_1(L_1) = L_1^{k_{M,13}} \left(1 - \exp \left(- \left(\frac{L_1}{k_{M,14}} \right)^{k_{M,15}} \right) \right) \quad (3.22)$$

$$f_2(L_2) = L_2^{k_{M,23}} \left(1 - \exp \left(- \left(\frac{L_2}{k_{M,24}} \right)^{k_{M,25}} \right) \right) \quad (3.23)$$

The parameters $k_{M,13}$ and $k_{M,23}$ are used to take into account the effect of the different stresses generated by a force applied on the particle; $k_{M,i4}$, $k_{M,i5}$, and their corresponding exponential functions are used to model the grinding limit.

The function $h_i(\Phi)$ takes into account the effect of the shape of crystals on their breakage. In particular, the aspect ratio Φ is used as a measure of the particle morphology.

$$\Phi = \frac{L_1}{L_2} \quad (3.24)$$

The longer the particle, the higher the value of the aspect ratio and the easier it is to break a particle along a plan perpendicular to L_1 . Based on these considerations, the suggested functional form is as follows.

$$h_1(\Phi) = \frac{\Phi}{k_{M,16} + \Phi} \quad (3.25)$$

$$h_2(\Phi) = \frac{1}{k_{M,26}\Phi + 1} \quad (3.26)$$

Introducing the aforementioned functions in Equations 3.19 and 3.20, the resulting expressions for K_1 and K_2 are:

$$K_1 = k_{M,11} \left(\frac{m_M (\theta r_M)^2}{2} \right)^{k_{M,12}} \left(1 - \exp \left(- \left(\frac{L_1}{k_{M,14}} \right)^{k_{M,15}} \right) \right) \frac{L_1^{k_{M,13}} \Phi}{k_{M,16} + \Phi} \quad (3.27)$$

$$K_2 = k_{M,21} \left(\frac{m_M (\theta r_M)^2}{2} \right)^{k_{M,22}} \left(1 - \exp \left(- \left(\frac{L_2}{k_{M,24}} \right)^{k_{M,25}} \right) \right) \frac{L_2^{k_{M,23}}}{k_{M,26}\Phi + 1} \quad (3.28)$$

The mechanism underlying breakage, according to the type of mill considered, is assumed to be cleavage. In this type of fracture, the mother particle is ruptured into two smaller fragments of similar size. The equations used to model this type of breakage are:

$$g_1(L_1, x) = A_1 \exp\left(-\frac{(L_1 - x)^2}{B_1^2}\right) \quad (3.29)$$

$$g_2(L_2, x) = A_2 \exp\left(-\frac{(L_2 - x)^2}{B_2^2}\right) \quad (3.30)$$

The value of the parameters A_i has to ensure that both the number of fragments and the mass of the mother particles are preserved; the parameters B_i measure how broad the distribution of fragments is.

3.3.2.3 PBE for dissolution

The model for a batch well-mixed dissolution stage has the same form of the one presented in Section 3.3.2.1 for cooling crystallization.

$$\frac{\partial n}{\partial t} + \frac{\partial (D_1 n)}{\partial L_1} + \frac{\partial (D_2 n)}{\partial L_2} = 0 \quad (3.31)$$

$$n(L_1, L_2, t = 0) = n_0(L_1, L_2) \quad (3.32)$$

The PBE needs to be coupled with its initial condition, i.e. Equation 3.32, and with the boundary condition which is discussed in Section 3.3.2.4. The mass balance for the solute, reported in Equation 3.4, is used to ensure mass conservation. In Equation 3.31, D_1 and D_2 are the dissolution rates for the two characteristic dimensions and have a negative value. The kinetics used in this work are those suggested by Eisenschmidt.⁷⁵

$$D_i = -k_{D,i1} \exp\left(-\frac{k_{D,i2}}{T}\right) (1 - S)^{k_{D,i3}} \quad \text{with } S < 1 \quad (3.33)$$

3.3.2.4 Boundary conditions for crystallization and dissolution

Boundary conditions for the PBEs of Equations 3.2 and 3.31 must be assigned on the boundary of the $L_1 - L_2$ space domain, which is defined by $L_1 = 0$ or $L_2 = 0$, and by L_1 or L_2 becoming infinitely large. In fact, for first order PDEs, they have to be assigned on the portion of the boundary that belongs to the domain of dependence of the points in the 3D domain with $t > 0$, $L_1 > 0$, and $L_2 > 0$. Such portion corresponds to $L_1 = 0$ or $L_2 = 0$ in

the case of growth, and to L_1 and L_2 becoming infinitely large in the case of dissolution. In both cases $n(L_1, L_2, t)$ must be equal to zero on the relevant part of the boundary of the $L_1 - L_2$ plane.

3.3.3 Results analysis and key performance indicators

The advantage of an in-silico approach for the assessment of the process lies in the possibility of having access to all the properties of the system. Despite the great interest in the distributions of crystals as a whole, it is convenient to limit the analysis to a few key properties. The μ_{ij} moments of the population (see Equation 3.6) can be used to this aim. Each moment is in fact proportional to relevant quantities, such as the total number of particles suspended and their volume, as well as their total length and width. Furthermore, the ratios between the moments μ_{ij} can be used to calculate the average sizes of the particles and the broadness of the distribution in terms of standard deviation $\sigma_{1,V}$. Table 3.1 gives an overview of the average properties considered and used in this work.

Average quantities	
Volume weighted \bar{L}_1 :	μ_{22}/μ_{12}
Volume weighted \bar{L}_2 :	μ_{13}/μ_{12}
Volume weighted $\sigma_{1,V}$:	$\sqrt{\mu_{32}/\mu_{12} - \bar{L}_1^2}$
Volume weighted Φ :	$\mu_{21}\mu_{12}$

TABLE 3.1: Performance indicators used in this work.

Through these quantities, it is possible to quantitatively define the specifications on the products. In the current work, a minimum value for the average width \bar{L}_2 and a maximum value for the average length \bar{L}_1 are defined together with an upper limit for the aspect ratio. These conditions identify a portion of the L_1L_2 -plane, referred to as *target region*. If the point with coordinates given by the average sizes belong to this region, then the product satisfies the constraint on the morphology of the particles.

Concerning the broadness of the distribution, the value of $\sigma_{1,V}$ has to be kept as low as possible for the sake of the homogeneity of the final powder.

The presence of fines in the final product can be evaluated by calculating the total number of particles per unit mass of solvent with sizes L_1 and L_2 below a threshold value λ using the following formula:

$$F(t) = \int_0^\lambda \int_0^\lambda n(L_1, L_2, t) dL_1 dL_2 \quad (3.34)$$

A key feature of the process is the productivity P , defined as the ratio between the mass of crystals recovered at the end of the cycles and the total process time.

$$P = \frac{m_R}{t_T} \quad (3.35)$$

3.3.4 Parametric analysis

The aim of the work is to assess the feasibility of the cyclic process and to investigate the effect of the different operating conditions on the key performance indicators. A simple, yet thorough, approach to this problem is the parametric analysis, which is based on a broad set of simulations performed by combining different values for all the process variables, thus enabling to explore the entirety of the design space. This type of analysis allows to get a deep insight on the characteristic features and trends of the process, as well as to explore how to improve and optimize the process performance.

3.4 RESULTS AND DISCUSSION

3.4.1 Choice of model parameters and operating conditions

The model presented in Section 3.3 is intended as a tool to investigate the feasibility of the proposed process and its main features. However, the lack of information in open literature concerning the kinetics for all the phenomena occurring in the different stages of the cycles does not allow to study the application of the designed process to a specific compound. Therefore, the values adopted for the parameters appearing in the different kinetics equations are borrowed from different compounds, if available, and are chosen so as the physics at the basis of the model is correct and consistent. Table 3.2 gives an overview of the values of the parameters used in this work.

In particular, the implemented parameters for homogeneous and heterogeneous primary nucleation are those for L-glutamic acid estimated by

Crystallization			Milling		
Parameter	L_1	L_2	Parameter	L_1	L_2
$k_{G,i1}$ [$\mu\text{m s}^{-1}$]	2400	58	$k_{M,i1}$ [s^{-1}]	5×10^{-4}	5×10^{-4}
$k_{G,i2}$ [K]	2400	2400	$k_{M,i2}$ [-]	1.75	1.75
$k_{G,i3}$ [-]	3.7	2.5	$k_{M,i3}$ [-]	2	1
$k_{\text{Hom},1}$ [$\# \text{kg}_{\text{w}}^{-3} \text{s}^{-1}$]	1.3×10^{24}		$k_{M,i4}$ [μm]	20	20
$k_{\text{Hom},2}$ [-]	163		$k_{M,i5}$ [-]	9	9
$k_{\text{Het},1}$ [$\# \text{kg}_{\text{w}}^{-3} \text{s}^{-1}$]	1.4×10^5		$k_{M,i6}$ [-]	10	1
$k_{\text{Het},2}$ [-]	10		Heating		
$k_{\text{Sec},1}$ [-]	1.4×10^{20}		Parameter	L_1	L_2
$k_{\text{Sec},2}$ [-]	0.6		$k_{D,i1}$ [$\mu\text{m s}^{-1}$]	0.818×10^6	0.136×10^6
$k_{\text{Sec},3}$ [-]	0.75		$k_{D,i2}$ [K]	3572	3223
$k_{\text{Sec},4}$ [-]	2		$k_{D,i3}$ [-]	1	1

TABLE 3.2: Model parameters used in this work.

Scholl et al.,⁷⁶ while those for growth have been obtained by refitting the experimental evidence collected for L-glutamic acid by Ochsenbein et al.⁷⁷ with the size independent growth model reported in Equation 3.7. The parameters for dissolution are those of potassium dihydrogen phosphate as reported by Eisenschmidt et al.⁷⁵ The values adopted for the breakage kinetics have been obtained by visual fitting of dedicated simple breakage experiments performed by us using a suspension of L-glutamic acid crystals in water.

Along with the parameters characteristic of the kinetics of the system, the model includes a set of variables representing the operating conditions of the process. The variety of unit operations involved in the cycles inherently leads to a broad design space. A thorough analysis of the different stages helps in the identification of the sensible ranges of values for the operating conditions of the process.

The process has to be operated between the initial temperature T_0 and the final temperature T_F , thus recovering the desired amount of mass m_F . Being the first step a seeded crystallization stage, it is necessary to define the type of seed crystals fed, both in terms of particle distribution and mass. The crystallization stages have to be characterized in terms of temperature profile and cooling rate β_C . Heating rates and heating ramps have also to be defined for the heating stage, with a further decision variable represented by the amount of mass dissolved m_D . Concerning the milling, the residence time in the grinding chamber τ and the rotor speed θ are the characteristic operating conditions.

Given the large amount of process variables, it is of crucial importance to reduce the degrees of freedom of the process to the minimum extent by applying some design rules of thumb, wherever possible. For example, the initial and final temperature of the process are determined by the synthesis stage and by the solubility curve respectively; these values are also used to determine the differences between the final temperatures of the cooling stages. The seeds, in terms of both distribution and mass, impact the evolution of the system during cooling. Generally, the seeds are produced by milling, being therefore a very fine powder, and the mass added is about 1% of the total mass recovered. Considering the cooling rate, its value is based on a trade-off, between avoiding undesired nucleation while not reaching a long cooling time. The heating ramp chosen is such that it is as fast as possible, to reduce the duration of the dissolution stage. Table 3.3 lists all the operating conditions and their values adopted during simulations. In the current work, particular attention is put on the effect of the number of

Process		Stages	
Condition	Set point	Crystallization	
Initial temperature T_0	50 °C	Condition	Set point
Final temperature T_F	25 °C	Temperature drop ΔT_C	$(T_0 - T_F)/C$
Seed mass m_0	0.1 g/kg _w	Cooling rate β_C	0.1 °C/min
Seed PSSD n_0	Gaussian	Milling	
	$\mu_1 = 100 \mu\text{m}$	Condition	Set point
	$\mu_2 = 50 \mu\text{m}$	Residence time τ	5 s
	$\sigma_{1,V} = 5 \mu\text{m}$	Rotor speed θ	Varying
	$\sigma_{2,V} = 5 \mu\text{m}$	Dissolution	
Number of cycles C	Varying	Mass dissolved m_D	Varying
Solubility $c^*(T)$	$3.37e^{0.036T[^\circ\text{C}]}$ g/kg	Heating rate β_H	1 °C/min

TABLE 3.3: Operating conditions characterizing the process as a whole and the single stages.

cycles, C , the rotor speed, θ , and the amount of mass dissolved during each dissolution stage, m_D .

Concerning the specifications on the products, the values adopted are $400\ \mu\text{m}$, $130\ \mu\text{m}$, and 3 for $L_{1,\text{max}}$, $L_{2,\text{min}}$, and Φ_{max} respectively. The values chosen for $L_{2,\text{min}}$ and Φ_{max} are such that the final average width L_2 of the crystals is at least twice the initial one by retaining at the same time a compact morphology. A value of $\lambda = 20\ \mu\text{m}$ has been chosen as the threshold value to identify fines.

3.4.2 *Solution of the PBE*

In order to solve the population balance equation for crystallization and dissolution, a high resolution finite volume method was used. The multidimensional partial differential equation is discretized in the space domain thus obtaining a set of ordinary differential equations. As highlighted by Gunawan,⁷⁸ high resolution methods exploit flux limiters across boundaries interface to smoothen possible discontinuities. The resulting algorithm exhibits an increased stability allowing at the same time for high accuracy and limited computational burden. The van Leer flux limiter is used in this work.⁷⁹

The population balance equation for the milling stage is solved applying the fixed pivot method as suggested by Kumar,⁵³ which allows for strict preservation of number and volume of the crystals.

For the sake of simplicity, the same spatial grid has been adopted for both the high-resolution and the fixed pivot method, namely 500 points for dimension L_1 and 300 for L_2 . The computational time required by the breakage simulations varies with the milling intensity applied, ranging from 2 seconds to some minutes using an Intel[®] Core[™] i7-4770 CPU @ 3.40 GHz processor with 16.0 GB RAM.

3.4.3 *Identification of reference conditions and process assessment*

When designing a new process, it is necessary to identify some reference conditions for the investigated variables and use this as a starting point for the ensuing analysis of the design space. In the current work, the reference set of values for the different variables is reported in Table 3.4.

Figure 3.3 illustrates the outcome of the simulation at these operating conditions.

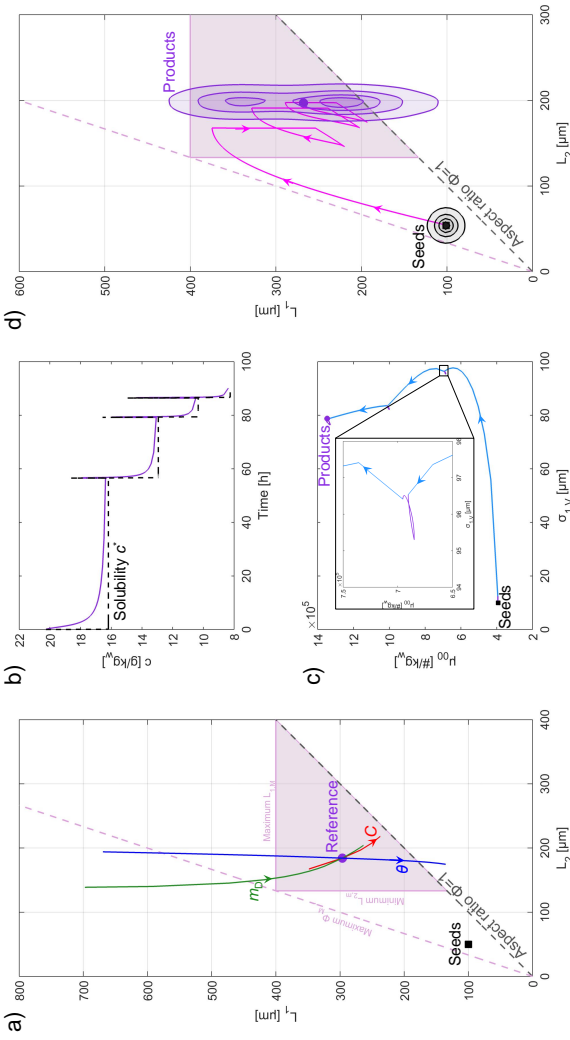


FIGURE 3.3: Results of simulation for the assessment of process feasibility. In (a), the average sizes of the products are shown. The black square corresponds to the average sizes of the seeds used in the first crystallization stage, while the purple dot corresponds to the outcome of the reference experiments described in Section 3.4.3. Along the blue, red, and green line are the average sizes of the distributions obtained by changing the rotor speed θ , the number of cycles C , and the mass dissolved m_D respectively. In (b) the concentration and the solubility profiles throughout the cycles in the case of the reference simulation are shown. In (c) the evolution of the μ_{00} cross-moment, proportional to the number of particles suspended, as a function of the variance of the distribution $\sigma_{1,v}$, related to the broadness of the distribution in the L_1 direction, is shown. The blue part of the curve highlights the evolution of these two properties during the milling stages. In (d), the particle size and shape distributions of both the seeds and the products in the case of the reference simulation are shown.

Variable	Reference operating condition
Number of cycles, C :	4
Rotor speed, θ :	7,000 rpm
Mass dissolved, m_D :	40%

TABLE 3.4: Values adopted as a reference for the investigated operating conditions.

In particular, Figure 3.3(a) clearly shows how the average sizes of the products, represented by the purple marker, belong to the acceptance region, satisfying therefore the specifications imposed on the morphology of the crystals. These results suggest that the process could in principle be used to selectively manipulate the size and shape of the particles. In order to gain a better insight into the properties of the final product, the seeds and the final distributions can be compared as shown in Figure 3.3(d). Here, it is immediately clear that, despite providing the possibility of obtaining particles with the desired morphology, the process has led to a distribution of products much broader than the one of the original seeds. Such behavior is due to two different causes, namely nucleation during cooling and breakage of crystals during milling. In Figure 3.3(b) the concentration and saturation profile throughout the stages of the process are illustrated. The spikes correspond to increases in solute and equilibrium concentration, which are due to the dissolution stage, lasting only few minutes due to its fast kinetics. Figure 3.3(c) shows the evolution of the μ_{00} moment, proportional to the number of crystals, with respect to the volume weighted standard deviation $\sigma_{1,V}$, which is an indicator of the broadness of the distribution. The blue segments of the curve are those representing the evolution of the two quantities during the three milling stages. The trends suggest that the milling stage is the step that determines the number of crystals suspended, as well as the broadness of the distribution. This is due to the breakage of crystals, which doesn't occur always at the center of the particles hence it forms fragments of different dimensions. Process feasibility is further investigated by analyzing the effect of single operating variables on the final product. To this aim, Figure 3.3(a) shows the outcome of simulations performed by varying the rotor speed θ from 3,000 rpm to 14,000 rpm (blue line), the number of cycles C from 2 to 6 (red line), or the amount of mass dissolved during the dissolution stage m_D (green line) from 0% to 99%. The variety of products obtained, whose properties meet process specifications, requires a thorough understanding of the effect

of the single process variables on the most important features of the final ensemble of crystals.

3.4.4 *Effect of mass dissolved*

The mass dissolved represents an important variable in determining the performance of the process and the quality of the final products. In order to assess this, simulations were performed varying the mass of crystals dissolved from 0% to 99% for three different values of rotor tip speed, namely 4,000, 7,000, and 10,000 rpm, and for a process consisting of 4 cycles. Figure 3.4 shows the increment in average width of the crystals as a function of the number based fraction of fines in the products for the different values of m_D . The curves obtained for $\theta = 7,000$ and $\theta = 10,000$ rpm exhibit a minimum, whose position varies with the rotor speed θ . The trend can be justified considering that, despite being able to remove a larger amount of fines by increasing the amount of mass dissolved, the high supersaturations generated in the following crystallization stage are mostly consumed by nucleation events, due to the reduced number of particles suspended. This would therefore lead to a decrease in the average L_2 . By further increasing the amount of mass dissolved, the number of particles constituting the ensemble gets drastically reduced and only a small amount of the suspended crystals overcomes the dissolution stage. By doing so, the increasing amount of solute mass recovered during the following crystallization stage, due to the smaller total crystal surface available, leads to bigger particles. The trend exhibited by the curve obtained at the lowest value of rotor tip speed is different. At a reduced milling intensity a large amount of fines are not produced; therefore, dissolution leads to the reduction of the size of the particles, without removing crystals from the suspension. However, secondary nucleation events occur anyways and fines are still present in the final products. The effect of the mass dissolved on the broadness of the distribution, $\sigma_{1,V}$, is directly proportional to the amount of fines formed, which increases with the amount of mass dissolved. For high values of m_D , since the ensemble of crystals is almost completely dissolved during the dissolution step, the value of the different key performance indicators will converge to a single point, which corresponds to crystallization from a clear solution. For the sake of comparison, Figure 3.4(c) illustrates the outcome of two simulations performed at a rotor speed θ of 7,000 and 10,000 rpm and a fraction of mass dissolved of 50%, where the minimum is located, and of 90%.

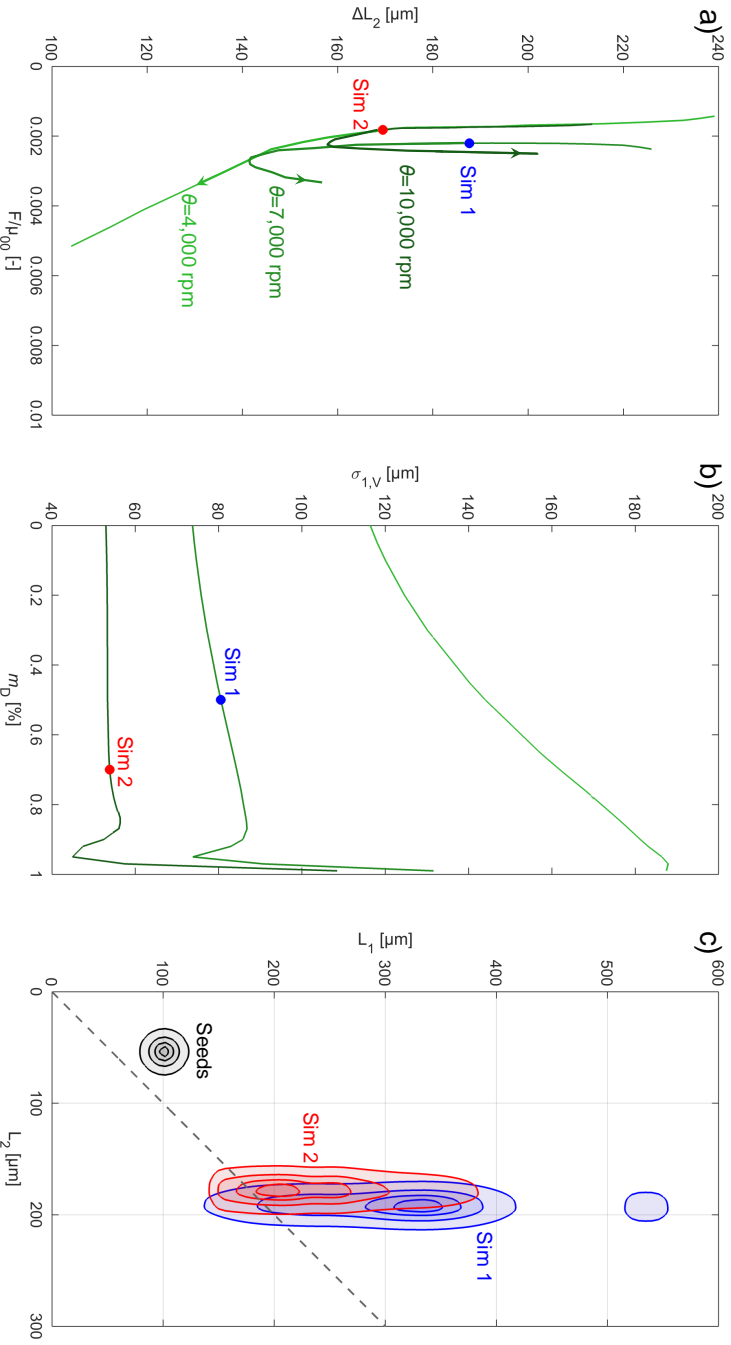


FIGURE 3-4: Results of the simulations performed to investigate the effect of the mass dissolved m_D . Simulations have been carried out assuming a constant number of 4 cycles and three different rotor speeds θ . The number based fraction of fines at the end of the process is reported. The broadness of the distribution of fines at the end of the process is reported. A comparison between two selected simulations, in terms of their particle size and shape distributions, is reported in (c).

3.4.5 *Effect of the rotor speed*

The effect of different milling intensities is investigated by considering a range of rotor speeds θ from 3,000 to 14,000 rpm; this is done for three different number of cycles, namely 4, 5, and 6. In Figure 3.5(a), the difference between the final and initial average ΔL_2 is reported as a function of the average final aspect ratio Φ . For increasing rotor speeds θ , the average aspect ratio steeply decreases until an asymptotic value is reached. Furthermore, higher values of θ lead to higher energy input, which favors the breakage of crystals also along the L_2 dimension. In Figure 3.5(b), ΔL_2 is plotted as a function of the broadness of the distribution $\sigma_{1,V}$. At first, for increasing values of θ , an increase in $\sigma_{1,V}$ can be observed. This can be explained by considering that, for low values of the rotor speed, the population at the end of the milling stage is constituted of both broken and unbroken particles, since the energy input provided by the rotor is not sufficient to efficiently break all the crystals. However, as θ further increases, the PSSD obtained after milling is more and more compact. The previous conclusions can be verified by comparing in Figure 3.5(c) the two populations obtained at 5,000 rpm, plotted in red, and at 10,000 rpm, in blue.

3.4.6 *Effect of the number of cycles*

Figure 3.6(a) and Figure 3.6(b) show the average sizes and the $\sigma_{1,V}$, respectively, obtained by incrementing the number of cycles, C , for a value of rotor speed of 4,000, 7,000, and 10,000 rpm. Increasing the number of cycles leads to a larger value of average L_2 for the products and improves the morphology of the particles by reducing L_1 . At the same time, the repeated milling stages allow for an effective breakage of the crystals, thus leading to more compact crystal distributions, as shown by the decreasing value of $\sigma_{1,V}$ throughout the cycles. However, it is possible to notice, by comparing two adjacent points along the curves at constant rotor speed in the figure, that the beneficial effect on these properties becomes less pronounced with each increment in the number of cycles. The reason for this is a combination of different causes, the influence of which is hard to quantify. First, the ratio between the mass suspended during each cooling stage and the amount of particles suspended decreases by increasing the number of cycles, since the higher number of milling stages performed leads to the formation of more crystals. Furthermore, breakage is a complex phenomenon, which depends also on the size of the particles, as shown in Equations 3.27 and 3.28. This

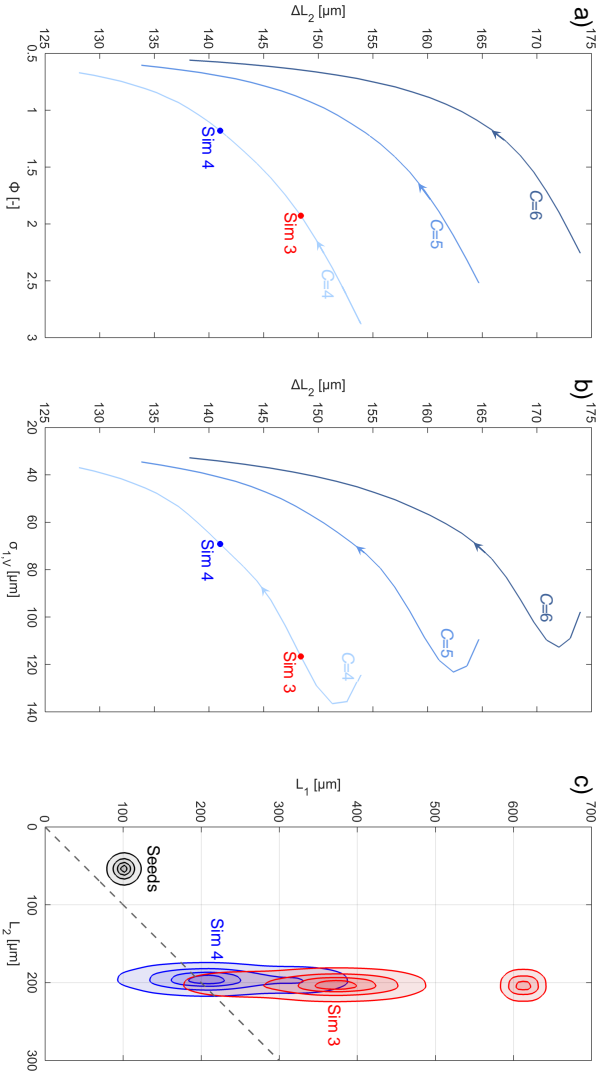


FIGURE 3.5: Results of simulations performed to investigate the effect of the rotor speed θ by increasing it from 3,000 rpm to 14,000 rpm. Simulations have been carried out assuming a constant fraction of mass dissolved ($mD=40\%$) and three different number of cycles. The arrows on each curve indicate the direction along which θ increases. In (a), the curves obtained show how an increased rotor tip speed leads to more equant particles characterized by a low aspect ratio Φ . As shown by the trends reported in (b), increasing the milling intensity allows also to obtain a more compact particle size and shape distribution at the end of the process. A comparison between the simulations Sim 3 and Sim 4 is reported in (c).

means that the way particles break depends on the characteristics of the crystals constituting the population suspended, which changes according to the number of cycles performed. Moreover, the efficiency in removing particles during dissolution depends on the size of the single crystals, as well as their distribution; the narrower the distribution, the smaller the number of crystals dissolved. Therefore, the same amount of solute mass is recovered during crystallization on a larger crystal surface, hence the change in size is reduced. The particle size and shape distributions obtained at the end of a process performed with 3 and with 5 cycles are reported in Figure 3.6(c).

3.4.7 *Parametric study of the process and heuristic optimum*

The analysis performed allows to understand the influence of the single operating conditions on the characteristic features of the crystals, but it is not exhaustive, as it does not consider the interplay between the different variables, hence it does not allow to identify the best conditions under which the process should be operated. However, for the purpose of this work, a multi-objective optimization, besides being computationally expensive and not being supported by a dedicated experimental model validation, would provide no useful information, given the choice of the growth, breakage, and dissolution kinetics used in the simulations (see the discussion in Section 4.1).

It is however useful to illustrate how the model can be used to identify optimal operating conditions in a heuristic manner, and it makes obviously sense to do this using the fictitious parameters defined in Section 4.1. In what follows, the outcome of this analysis is quantitatively discussed as if the model parameters referred to a real substance.

Therefore, in order to explore the whole design space and to identify and characterize possible trade-offs between the different properties of the products, a broad-range parametric analysis has been performed. The results of the set of simulations, performed by combining all the possible values of milling intensity (from 3,000 to 14,000 rpm, with a resolution of 500 rpm) and number of cycles (from 2 to 6) while keeping the amount of mass dissolved constant ($m_D = 40\%$), are illustrated in Figure 3.7(a) in terms of crystal dimensions L_1 and L_2 .

The wide variety of particles morphology achievable at the end of the process reflects the variability of conditions that can be implemented; different combinations of milling intensity and number of cycles allow to meet

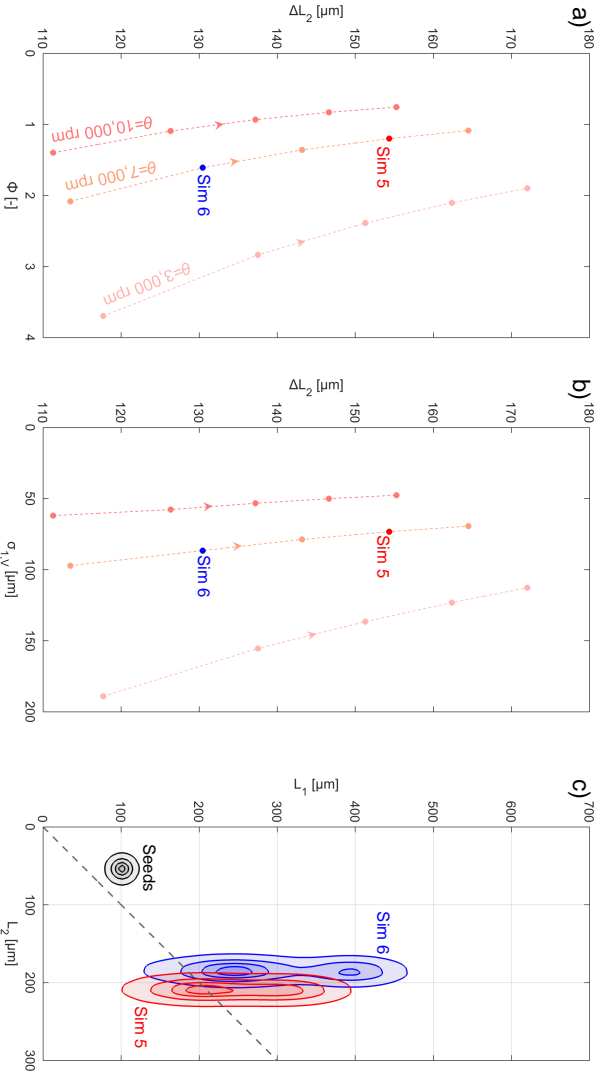


FIGURE 3.6: Results of simulations performed to investigate the effect of the number of cycles C . Simulations have been carried out assuming a constant fraction of mass dissolved ($m_D=40\%$) and three different rotor speeds θ . Since the number of cycles C is a discrete variable, results are reported as points rather than a continuous line. The dashed arrows can be used as guide for the eyes to identify the direction along which C increases. The effect on the increment of the average thickness, as well as on the aspect ratio, is reported in a), while b) shows the broadness of the distribution of the products for the different number of cycles analyzed. A comparison between two exemplary simulations is reported in c).

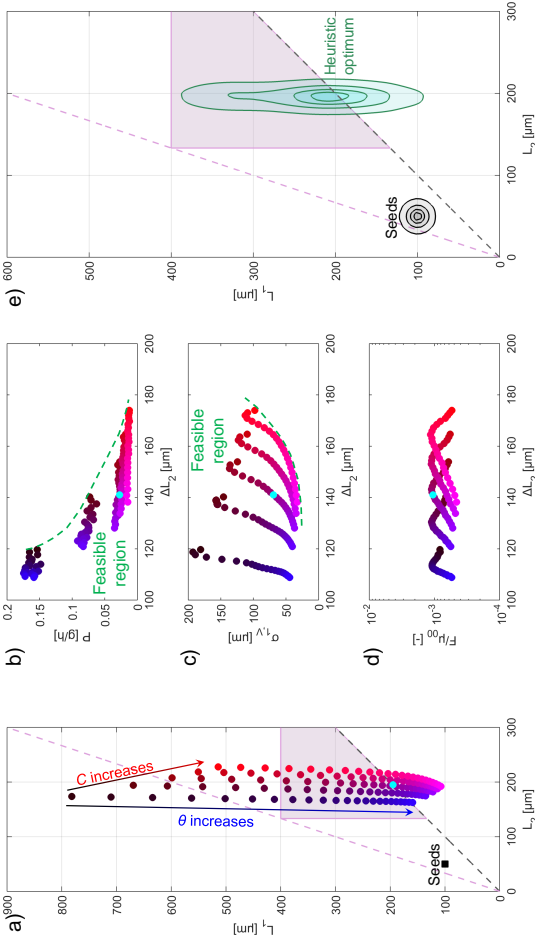


FIGURE 3-7: Results of the parametric analysis for the identification of characteristic process trends. The range of rotor speeds simulated ranges from $\theta=3,000$ rpm to $\theta=14,000$ rpm resolved every $\Delta\theta=500$ rpm. The effect of the number of cycles is investigated by increasing C from 2 to 6. Each dot is characterized by a specific color; increasing shades of blue and red identify respectively increasing milling intensities and number of cycles. The outcome of the simulation performed under the identified heuristic optimum conditions is reported in aquamarine. In (a), the average sizes for all the possible combinations of the operating conditions analyzed is reported. In (b), (c) and (d) the variance $\sigma_{1,v}$, the productivity P and the volume fraction of fines F/μ_{12} are reported as a function of the increment in crystal thickness ΔL_2 . The points identify both a feasible and an unfeasible region, which are separated by the corresponding Pareto curve reported in green. To conclude, in (e) the outcome of the heuristic optimum in terms of particle size and shape distribution is reported.

the process specifications. As previously mentioned, the intrinsic multi-objective nature of the optimization problem does not allow for a quick identification of the best operating conditions. However, the parametric analysis can be used to identify general, characteristic trends and process features, which in turn help understanding how to properly choose operating conditions close to optimality. To this aim, the process indicators defined in Section 3.3.3 can be used. Figure 3.7(b) reports the productivity P as a function of ΔL_2 . The plot clearly shows the presence of a trade-off between these two properties, a behavior typically encountered in chemical processes. A similar trend can be observed also in Figure 3.7(c), where another trade-off is identified between the broadness of the final PSD $\sigma_{1,V}$ and ΔL_2 , as well as in Figure 3.7(d), where the ratio of fines F/μ_{00} for the different process simulations is plotted as a function of ΔL_2 . Based on the previous observations, it is clear that it is not possible to optimize all the objectives of the process at the same time.

The identification of the optimal conditions for the process is not trivial and is outside the scope of this paper. However, based on the previous trade-offs, some heuristic optimal conditions can be proposed, for instance a milling intensity of 10,000 rpm and a number of cycles of 4, which allow increasing L_2 without decreasing the productivity. This set of operating conditions also leads to a reduction in the relative amount of fines in the final product. The distribution of crystals obtained at the end of this simulation is shown in Figure 3.7(e), while its average properties are indicated in Figure 3.7 with the aquamarine markers.

While we believe that the conclusions above illustrate trade-offs that have a general validity, the specific conclusions and observations strongly depend on the specific substance considered, and on the corresponding parameters.

3.4.8 Comparison with other processes

In order to further verify the suitability of the process for a direct control of the size and shape of the particles, as well as the properties of the final distribution, we compare the 3-stage process presented above with a one-stage cooling crystallization process on the one hand and on the other hand with a single sequence of a crystallization step followed by milling. The results of such analysis, carried out using the model described in Section 3, are illustrated in Figure 3.8 and discussed in the following.

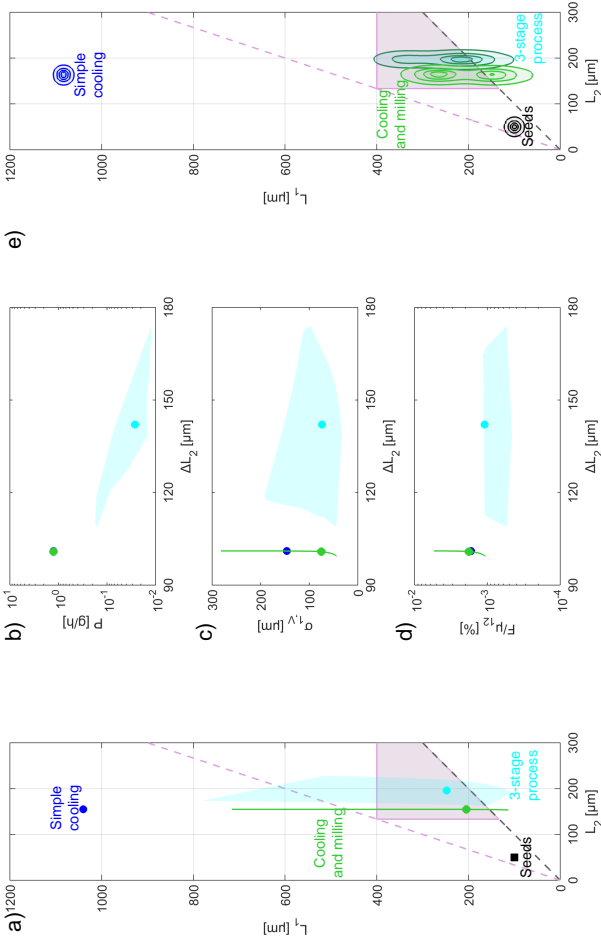


FIGURE 3.8: Comparison of the 3-stage process (aquamarine area) with a single crystallization stage (blue dot) and cooling crystallization followed by milling (green line). The range of rotor speeds θ investigated spans from 3,000 rpm to 14,000 rpm, while the number of cycles changes from 2 to 6. The percentage of mass dissolved m_{D} is constant and equal to 40% of that suspended at the end of the milling stage. The comparison is carried out in terms of average sizes in (a). Broadness of the final distribution, productivity and volume fraction of the fines in the products are analyzed in (b), (c), and (d) respectively. Note that in (b) and (d) the green and blue dots overlap. The particle size and shape distributions of the seeds and of the products obtained at the end of the three different processes are reported in (e).

In Figure 3.8(a) the average sizes of the products obtained at the end of the 3-stage process are reported as the aquamarine area (for rotor speeds θ varying from 3,000 to 14,000 rpm and for a number of cycles ranging from 2 to 6), while those obtained at the end of the cooling stage, both with and without milling, are reported as a green line (with θ ranging from 3,000 to 14,000 rpm) and as a blue dot, respectively. In Figures 8b, 8c and 8d the productivity, broadness of the distribution and the fraction of fines at the end of the process are reported as a function of the variation in average width ΔL_2 . In order to carry out a fair comparison between the cooling followed by milling and the 3-stage process, the process indicator chosen to identify operating conditions for both processes is the variance $\sigma_{1,V}$. A value of 75 μm has been chosen as a reference. Based on this choice, 4 cycles and $\theta=7,500$ rpm are adopted for the 3-stage process, while a rotor speed of 8,500 rpm is used in the case of a process with milling after cooling.

Concerning the average sizes and the morphology of the particles obtained at the end of the three different processes, as shown in Figure 3.8(a) the single cooling stage (blue dot) allows to increase the size of the particles, but their morphology is significantly different from the desired one; a subsequent milling would in fact allow to obtain more equant particles (green dot), whose morphology is close to that of the crystals obtained with the three stage process. Figure 3.8(b) shows how the 3-stage process allows to reduce significantly the $\sigma_{1,V}$ in comparison with the value achieved during the single crystallization stage. This is due to both the milling action and the reduced ΔT_C , which minimizes the extent of nucleation. However, if milling is carried out after the single crystallization step, an improvement in the dispersity of the distribution, similar to that obtained with the 3-stage process, can be attained.

The productivity of the 3-stage process is the lowest among the three alternatives, as shown in Figure 3.8(c). However, this comparison only considers the crystallization aspect of the manufacturing of crystals, neglecting therefore how the downstream process times are affected by such a change in particles morphology. A direct comparison might be therefore misleading.

Figure 3.8(e) shows the particle size and shape distributions of the seeds and of the products of all the processes considered. The comparison between the outcome of the 3-stage process and that of cooling crystallization with milling clearly highlights the benefits of the repeated temperature cycles on the ensemble of crystals. Despite the lower milling intensity applied in the 3-stage process, the products obtained are still monodispersed, while

the ones simply milled exhibit clearly two modes, i.e. a highly undesirable feature.

The main goal of the 3-stage process is that of manipulating the shape of the crystals as well as of reducing the number of undesired fines in the final product. Figure 3.8(c) shows how the temperature cycles effectively decrease the presence of these fine particles in comparison to the other alternatives, improving therefore the quality of the final distribution in terms of further processability.

As mentioned in the introduction, thermal cycles without milling have been proposed to fulfill the same process specifications discussed here. In the case illustrated in Figure 8a, pure temperature cycles can be viewed as the limiting case for a rotor speed θ approaching zero. It is apparent that product crystals obtained with $\theta=0$ and varying number of cycles would yield crystals outside the target region. Though specific to the fictitious substance considered in this parametric study, such result is not surprising and must be general. In fact, it is well known that the attainable region in the L_1L_2 -plane for temperature cycles has a limited amplitude.^{70,71} We definitely believe that a milling step expands the design space of the crystallization process significantly, and enables the generation of crystals with sizes and shapes not attainable without it.

The process developed and presented in this work stands out as a valid technique for the manipulation of particle morphology. The choice of a process over the others leads to advantages and disadvantages that need to be carefully considered, but it is beyond the scope of this paper to suggest which of the three alternatives presented should be implemented when considering the crystallization of a specific compound.

3.5 CONCLUSIONS

A new process, aimed at tuning the size and shape of crystals by combining crystallization, milling and dissolution stages has been designed. A conceptual design helped in defining the sequence of unit operations and in identifying the objectives for each one of them, as well as the key performance indicators for the process. The possible feasibility of this process has been assessed by means of a dedicated mathematical model, capable of describing phenomena ranging from the single particle to the process scale, to create a first set of simulations. Such simulations allowed to further investigate the effect of each operating condition on the performance indi-

cators, providing insight on the significance of the phenomena occurring in the different stages.

A second larger set of simulations has been performed in order to perform a parametric analysis of the process, to identify the characteristic trends obtained by combining all the possible operating conditions. The results of such an analysis highlighted the presence of trade-offs for the different properties of interest. According to the results collected during this simulation campaign, a heuristic optimization, whose aim was to determine close-to-optimality conditions, has been performed. In particular, a successful outcome is achieved when combining mild milling intensities, granting compact particle size and shape distributions, with a moderately large number of cycles, which allows to increase the width L_2 .

Finally, a comparison with two process alternatives, namely a single crystallization stage and a crystallization and milling process, highlighted the benefits achievable through the use of the combined cycles.

3.6 NOTATION

B	birth term in the PBE	$[\mu\text{m}^{-2} \text{kg}^{-1} \text{s}^{-1}]$
c	solute concentration in the liquid phase	$[\text{g kg}^{-1}]$
c_0	initial solute concentration in the liquid phase	$[\text{g kg}^{-1}]$
c^*	solubility	$[\text{g kg}^{-1}]$
C	number of cycles	$[-]$
d_I	diameter of the impeller	$[\text{m}]$
D_i	dissolution rate for dimension i	$[\mu\text{m s}^{-1}]$
E	death term in the PBE	$[\mu\text{m}^{-2} \text{kg}^{-1} \text{s}^{-1}]$
F	number fraction of fines	$[-]$
g_i	daughter distribution of the fragments along the i -th dimension	$[\mu\text{m}^{-1}]$
\mathbf{G}	vector of rates of change	$[\mu\text{m s}^{-1}]$
G_i	growth rate for dimension i	$[\mu\text{m s}^{-1}]$
\mathbf{k}_G	vector of growth rate parameters	[varies]
\mathbf{k}_{Hom}	vector of homogeneous nucleation rate parameters	[varies]
\mathbf{k}_{Het}	vector of heterogeneous nucleation rate parameters	[varies]
\mathbf{k}_{Sec}	vector of secondary nucleation rate parameters	[varies]
\mathbf{k}_M	vector of breakage frequency parameters	[varies]
k_v	shape factor	$[-]$
K_i	breakage frequency for dimension i	$[\text{s}^{-1}]$
J	nucleation rate	$[\text{kg}^{-1}\text{s}^{-1}]$
L_i	crystals characteristic dimension i	$[\mu\text{m}]$
m	mass	$[\text{g}]$

n	number density function	$[\mu\text{m}^{-2} \text{kg}^{-1}]$
n_0	PSD of seed crystals	$[\mu^{-2} \text{kg}^{-1}]$
N_P	power number	[-]
P	productivity	$[\text{g h}^{-1}]$
S	supersaturation	[-]
t	time	[s]
T	temperature	$[\text{°C}]$
V	volume of the reactor / liquid phase	$[\text{m}^3]$
β_C	cooling rate	$[\text{°C min}^{-1}]$
β_H	heating rate	$[\text{°C min}^{-1}]$
$\delta(L_i)$	Dirac's delta function	$[\mu\text{m}^{-1}]$
ϵ	power input	$[\text{W kg}^{-1}]$
Φ	aspect ratio	[-]
μ_{ij}	cross moment ij of the PSSD	[varies]
ρ	density of the crystalline phase	$[\text{kg m}^{-3}]$
$\sigma_{1,V}$	volume weighted standard deviation in the L_1 direction	$[\mu\text{m}]$
τ	residence time in the mill	[s]
ω	impeller rotational speed	[rps]

MANIPULATION OF PARTICLE MORPHOLOGY BY CRYSTALLIZATION, MILLING, AND HEATING CYCLES - EXPERIMENTAL CHARACTERIZATION

4.1 INTRODUCTION

In the pharmaceutical industry, drugs are required to act in a short amount of time and to specifically target certain organs of the human body with limited to no impact on the others. The way the active molecule interacts with body tissues is related to the so called *bioavailability* of the substance, a property, among other features, strongly related to the shape of the crystals of the active pharmaceutical ingredient (API). In particular, needle-like particles are characterized by scarce bioavailability, which, together with difficulties in their processability,^{38,61,80} led to the necessity of developing strategies for a better control of crystal morphology.

In the past years, two main strategies have been applied. The first consists in controlling the shape of crystals during the crystallization process itself. To this aim, different combinations of solvents and additives^{62,63,81-89} are tested and applied. The approach is based on the different chemical interactions that are established at the solid-liquid interface between molecules in the solid phase and in solution. The inclusion of additive molecules on the active sites of the crystal surface can actually be successfully used to promote the growth of surfaces otherwise not favored. However, a typical drawback of this approach lies in the limited amount of additives and solvents that can be used in compliance with the strict regulatory requirements for the chemicals used in the production of APIs. Therefore, another technique commonly used involves the use of temperature cycles.^{16,67,90} However, one possible limitation lies in the shapes achievable when repeatedly dissolving and growing different facets, as the resulting morphology is not necessarily the one granting the desired product properties. The second approach envisions shape manipulation as part of the downstream proces-

Salvatori F. and Mazzotti M., Manipulation of particle morphology by crystallization, milling, and heating cycles - Experimental characterization, *Industrial & Engineering Chemistry research*, **2018**, 57 (45), 15522-15533.

sing and is performed as a standalone unit operation, namely milling.^{7,91–93} Here, size reduction is achieved by exploiting mechanical action, thus breaking the crystals and reducing mainly their length. Due to drawbacks such as overheating of the solid particles and formation of amorphous materials,^{41,42} dry milling is currently being dropped in favor of wet milling. However, the problem of fine splinters formed during rupture still remains unsolved.

To tackle this problem, in a previous publication,³⁴ we proposed and designed a process, called 3-stage process, consisting in a combination of different stages to selectively manipulate the morphology and size of needle shaped crystals. First, a clear saturated solution at high temperature, coming from the synthesis stage, is fed to a crystallizer, where seed crystals are added in order to reduce to a minimum the occurrence of nucleation events during crystallization. The system is then cooled, recovering solute molecules from the liquid phase by incorporating them in the crystal lattice. The suspension obtained at the end of this first stage is fed to a continuous rotor-stator wet mill, where milling is performed. The outlet stream is collected in a second crystallizer, where it is heated to a higher temperature in order to dissolve the fines formed during the previous stage. The stages are repeated cyclically as many times as desired, until the process is concluded by a final cooling crystallization step. The novelty of the 3-stage process, in comparison to similar techniques,⁹⁴ lies in the possibility of using industrially available equipment and well developed techniques to selectively manipulate particle morphology.

A first assessment of process feasibility has been performed by means of a specifically tailored mathematical model, capable both of capturing phenomena occurring at the single particle scale and of describing the unit operations at the process scale. The effect of the single operating conditions has also been investigated, to understand their effect on the ensemble of particles and on the morphology of the final product. Furthermore, the model has been used to simulate a large number of experiments obtained by varying the different process variables and to subsequently identify heuristic optimum. This in-silico experiment was chosen as the best trade-off, i.e. as the one granting the specific requirements concerning the size and shape of crystals while ensuring a good process productivity. This simulation has been subsequently compared with process simulations of cooling crystallization, both with and without a final milling stage, thus highlighting the possible benefits deriving from the application of the 3-stage process over the other two alternatives. These results certainly represented a novelty,

as no other multidimensional model has been presented and discussed in details, for such a complex crystallization system, in the literature before.

In this work, an experimental campaign is designed, carried out, and evaluated together with the outcome of process simulations to assess and characterize the process and its characteristics. The work is structured as follows. In Section 4.2 the mathematical model used for process simulations, as well as the theoretical background for the choice of the values for the kinetic parameters and the key performance indicators used, is presented. Section 4.3 reports a detailed description of the laboratory setup used to carry out the experimental tests, along with the materials, the procedures adopted, and the operating conditions implemented during the experimental campaign. In Section 4.4, the results of laboratory tests, performed with β L-Glutamic acid, aimed at verifying first the process feasibility and then the effect of selected operating conditions on the process outcome via a comparison with model simulations are presented. The analysis of the experiments carried out at different operating conditions and their comparison with the corresponding simulations will constitute the basis for the identification of general, heuristic, optimal conditions, under which the process should be operated in order to tune the final properties of the powder effectively. Furthermore, the results of a single crystallization stage and a single crystallization stage followed by milling are analyzed, together with those obtained for the 3-stage process, for a better understanding of advantages and disadvantages deriving from the application of the novel technology. The unique insight gained with the μ -DISCO is fundamental for a thorough quantification and characterization of the improvements in particle morphology achievable with the combination of temperature cycles and breakage through mechanical action.

4.2 THEORY

In the previous chapter, the feasibility of the 3-stage process was assessed in-silico by means of process simulations. To this aim, a mathematical model based on morphological population balance equations (MPBE) has been developed. In this work, experiments are devised and performed in order to verify the qualitative trends obtained through simulations. For the sake of clarity, here a brief though comprehensive description of the model is reported along with a description the numerical methods exploited to solve its equations. Furthermore, the properties considered to quantitatively characterize the final products are presented and discussed in detail.

4.2.1 Crystal model and PBE

Crystals are usually characterized by the complex features studied in the context of crystallography.^{72,95,96} Of particular relevance is the development of models capable of capturing the basic properties of crystal lattices with a limited number of descriptors. The generic particle model, as presented by Schorsch et al.²³ and further developed by Rajagopalan et al.,⁵¹ satisfies these needs and is adopted in this work. Based on this model, a needle-like crystal is approximated by a cylinder of length L_1 and width L_2 .

According to the characteristic length and width of each crystal belonging to the crystals' ensemble, the particle size and shape distribution (PSSD) can be reconstructed. In particular, $n(L_1, L_2)dL_1dL_2$ represents the number of particles with length $L_1 \in [L_1; L_1 + dL_1]$ and width $L_2 \in [L_2; L_2 + dL_2]$. PSSDs are graphically represented in the L_1L_2 -plane as contour plots, where, along each isoline, the function $n(L_1, L_2)$ attains a constant value.

PSSDs, as well as the chosen particle descriptors, constitute the basis for the mathematical model of the process. The generic formulation of a morphological population balance equation for well-mixed a batch process, where no change in the volume occurs, is reported by Ramkrishna [45] and reads as follows:

$$\frac{\partial}{\partial t}n(t, \mathbf{x}) + \nabla_{\mathbf{x}} \cdot [\mathbf{G}(t, \mathbf{x}, \mathbf{z})n(t, \mathbf{x})] = B(t, \mathbf{x}, \mathbf{z}) - E(t, \mathbf{x}, \mathbf{z}) \quad (4.1)$$

In Equation 4.1, $n(t, \mathbf{x})$ is the number density function representing the crystal ensemble, defined on the internal set of coordinates \mathbf{x} , representing the particle descriptors; \mathbf{G} is the vectorial field describing the growth rates, function of the properties \mathbf{z} of the continuous phase and - in principle - of the particle descriptors \mathbf{x} , along the internal coordinates. The terms $B(t, \mathbf{x}, \mathbf{z})$ and $E(t, \mathbf{x}, \mathbf{z})$ are used to model the birth and death of crystals, respectively, due to breakage, agglomeration, and nucleation events. The advantage of this type of model lies in its flexibility, due to the possibility of tailoring each term in the equation according to the physical phenomena characterizing each stage of the process. A detailed description of these terms for each step of the 3-stage process has been reported recently [34]. For the sake of completeness and clarity however, in the following the equations for each stage are briefly discussed.

Under the assumption of cylindrical particles, perfectly-mixed suspension, and no agglomeration and breakage events, the population balance equation for a batch crystallizer can be recast as:

$$\frac{\partial n}{\partial t} + \frac{\partial (G_1 n)}{\partial L_1} + \frac{\partial (G_2 n)}{\partial L_2} = J \delta(L_1) \delta(L_2) \quad (4.2)$$

$$n(L_1, L_2, t = 0) = n_0(L_1, L_2) \quad (4.3)$$

$$n(L_1 = 0, L_2, t) = 0 \quad (4.4)$$

$$n(L_1, L_2 = 0, t) = 0 \quad (4.5)$$

Equations 3.3, 4.4 and 4.5 represent respectively the initial and boundary condition of Equation 4.2, describing the particle size and shape distribution at the beginning of the process and the flux of particles across the boundaries of the $L_1 - L_2$ domain. In order to ensure mass conservation, the population balance equation is coupled with a material balance for the solute, which, under the assumption of constant volume of the suspension, can be written as follows.

$$\frac{dc}{dt} = -k_V \rho \frac{d\mu_{12}}{dt} \quad (4.6)$$

$$c(t = 0) = c_0 \quad (4.7)$$

where k_V is the shape factor, which is equal to $\pi/4$ in the case of cylindrical particles, where $V_P = \pi L_1 L_2^2/4$ is the volume of the particle, and μ_{12} is the cross-moment of the particle size and shape distribution, which is directly proportional to the total volume of the suspended crystals and is defined as follows

$$\mu_{12}(t) = \int_0^\infty \int_0^\infty n(L_1, L_2, t) L_1 L_2^2 dL_1 dL_2 \quad (4.8)$$

The equations used to model the nucleation $J^{73,76}$ and the growth rates G_1 and G_2^{77} are

$$J = J_{\text{Sec}} + J_{\text{Hom}} + J_{\text{Het}} \quad (4.9)$$

$$J_{\text{Hom}} = k_{\text{Hom},1} \exp\left(-\frac{k_{\text{Hom},2}}{\ln^2 S}\right) \quad (4.10)$$

$$J_{\text{Het}} = k_{\text{Het},1} \exp\left(-\frac{k_{\text{Het},2}}{\ln^2 S}\right) \quad (4.11)$$

$$J_{\text{Sec}} = k_{\text{Sec},1} \epsilon^{k_{\text{Sec},2}} m_S^{k_{\text{Sec},3}} \bar{G}^{k_{\text{Sec},4}} \quad (4.12)$$

$$G_i = k_{G,i1} \exp\left(-\frac{k_{G,i2}}{T}\right) (S-1)^{k_{G,i3}} \quad \text{with } S > 1 \quad (4.13)$$

The population balance equation for a continuous rotor-stator wet mill, described as a plug-flow tubular apparatus (i.e. under conditions of perfectly segregated flow), operated at steady-state, under the assumption of constant temperature and supersaturation, where no growth, nucleation, and agglomeration events occur, can be written as

$$\frac{dn}{d\tau} = B_1 + B_2 - E \quad (4.14)$$

$$B_1 = \int_{L_1}^{\infty} K_1(x, L_2)n(x, L_2, \tau)g_1(L_1, x)dx \quad (4.15)$$

$$B_2 = \int_{L_2}^{\infty} K_2(L_1, y)n(L_1, y, \tau)g_2(L_2, y)dy \quad (4.16)$$

$$E = K_1(L_1, L_2)n(L_1, L_2, \tau) + K_2(L_1, L_2)n(L_1, L_2, \tau) \quad (4.17)$$

$$n(L_1, L_2, \tau = 0) = n_0(L_1, L_2) \quad (4.18)$$

This model has been developed and assessed along with its assumptions in a previous publication.³⁵ The term τ represents here the residence time in the grinding chamber of the mill, while B_1 , B_2 , and E are the birth and extinction terms due to breakage of particles and the subsequent formation of smaller fragments. The equations chosen for the breakage frequencies and the daughter distributions are of the same functional form proposed elsewhere [35]

$$K_1 = k_{M,11}m_M(\theta r_M)^2 \left(\frac{L_1}{L_{ref,1}}\right)^{k_{M,12}} \left(1 + \exp\left(-\frac{L_1 - k_{M,13}}{L_{ref,2}}\right)\right)^{-1} \frac{\Phi}{\Phi + k_{M,14}} \quad (4.19)$$

$$K_2 = k_{M,21}m_M(\theta r_M)^2 \left(\frac{L_2}{L_{ref,1}}\right)^{k_{M,22}} \left(1 + \exp\left(-\frac{L_2 - k_{M,23}}{L_{ref,2}}\right)\right)^{-1} \frac{k_{M,24}}{k_{M,24} + \Phi} \quad (4.20)$$

$$g_1(L_1, \eta) = \frac{2}{\eta} \quad (4.21)$$

$$g_2(L_2, \eta) = \frac{4L_2}{\eta^2} \quad (4.22)$$

Here, $\Phi = L_1/L_2$ represents the aspect ratio of the particle that is breaking, while $g_i(L_i, \eta)$ represents the number of fragments of size L_i formed when a particle of size η breaks. It is worth noting that Equation 4.21 corresponds to breakage events yielding two fragments exhibiting a homogeneous distribution of lengths L_1 , whereas Equation 4.21 corresponds

to breakage events yielding two fragments exhibiting a homogeneous distribution of cross sectional areas $\pi L_2^2/4$. Note that $L_{\text{ref},1} = 1000 \mu\text{m}$ and $L_{\text{ref},2} = 1 \mu\text{m}$ are used to provide numerical stability when solving the population balance equation. For a deeper analysis of the functional forms chosen and the physics underlying the breakage of needle-like crystals in a continuous rotor-stator wet mill, the reader is referred to the original paper.³⁵

The model for a batch well-mixed dissolution stage has the same form of that presented in Equation 4.2 for cooling crystallization.

$$\frac{\partial n}{\partial t} + \frac{\partial (D_1 n)}{\partial L_1} + \frac{\partial (D_2 n)}{\partial L_2} = 0 \quad (4.23)$$

$$n(L_1, L_2, t = 0) = n_0(L_1, L_2) \quad (4.24)$$

$$n(L_1 \rightarrow \infty, L_2, t) = 0 \quad (4.25)$$

$$n(L_1, L_2 \rightarrow \infty, t) = 0 \quad (4.26)$$

The boundary conditions are chosen in agreement with the hypothesis of no incoming particles flux through the relevant $L_1 - L_2$ domain boundaries, which are $L_1 \rightarrow \infty$ and $L_2 \rightarrow \infty$ in the case of dissolution.⁴⁵ To ensure preservation of the mass of solute, Equation 4.6, is coupled with Equation 4.23. D_1 and D_2 are the dissolution rates along the two characteristic dimensions and have a negative value. The kinetics used in this work are of the same form proposed recently [75].

$$D_i = -k_{D,i1} \exp\left(-\frac{k_{D,i2}}{T}\right) (1 - S)^{k_{D,i3}} \quad \text{with } S < 1 \quad (4.27)$$

Table 4.1 reports in detail the values adopted for the kinetic parameters appearing in each of the models presented above. It is necessary to stress that the values chosen are not representative of a single specific system, but are selected based on different systems. Growth rate kinetics have been estimated from fitting raw data reported previously,²³ dissolution parameters have been adjusted from the ones reported already⁷⁵ for potassium dihydrogen phosphate, while breakage kinetics have been obtained by visual fitting of a limited amount of simple breakage experiments of L-glutamic acid particles in water.

4.2.2 Solution of the PBE

In order to solve the morphological population balance equations, the PDEs are discretized in the space of the internal coordinates L_1 and L_2 , using 400

Stage	Parameter	Dimension L ₁	Dimension L ₂
Crystallization	$k_{G,i1}$ [$\mu\text{m s}^{-1}$]	2400	58
	$k_{G,i2}$ [K]	2400	2400
	$k_{G,i3}$ [-]	3.7	2.5
	$k_{\text{Hom},1}$ [$\# \text{kg}^{-3} \text{s}^{-1}$]		1.3×10^{24}
	$k_{\text{Hom},2}$ [-]		163
	$k_{\text{Het},1}$ [$\# \text{kg}^{-3} \text{s}^{-1}$]		1.4×10^5
	$k_{\text{Het},2}$ [-]		10
	$k_{\text{Sec},1}$ [-]		2.5×10^{19}
	$k_{\text{Sec},2}$ [-]		0.6
	$k_{\text{Sec},3}$ [-]		0.75
	$k_{\text{Sec},4}$ [-]		2
Milling	$k_{M,i1}$ [s^{-1}]	16.06	16.06
	$k_{M,i2}$ [-]	1.907	1.964
	$k_{M,i3}$ [μm]	30	30
	$k_{M,i4}$ [-]	$\sqrt{3}$	$\sqrt{3}$
Dissolution	$k_{D,i1}$ [$\mu\text{m s}^{-1}$]	0.818×10^6	0.136×10^6
	$k_{D,i2}$ [K]	3572	3223
	$k_{D,i3}$ [-]	1	1

TABLE 4.1: Parameters adopted throughout simulations

and 50 grid points respectively. The PBE for the dissolution and crystallization stages are solved by implementing the finite volume method,^{78,79} which ensures strict preservation of the particle number through smoothening of the fluxes across the discretization boundaries. For the PBE of the milling stage, the fixed pivot technique is exploited,⁵³ as it guarantees exact preservation of the number and mass of the fragments formed during each simulated breakage event. Both numerical techniques allow to avoid numerical oscillations and loss of particle mass and number throughout the calculations. The simulations have been performed on a computer with an Intel(R) Core(TM) CPU i7-4770 @ 3.40 GHz processor, 8 cores, and 16 GB of RAM.

4.2.3 Process performance indicators

In order to evaluate the potential of the 3-stage process, it is necessary to identify measurable quantities that can be used to compare and assess the quality of the product crystals. A comparison between the particle ensembles as a whole, despite carrying inherently all the required information, is not useful due to the large amount of data shown simultaneously, which makes carrying out a clear and thorough analysis impossible. To circumvent this problem, the cross moments of the population μ_{ij} can be used based on the following definition:

$$\mu_{ij}(t) = \int_0^\infty \int_0^\infty n(L_1, L_2, t) L_1^i L_2^j dL_1 dL_2 \quad (4.28)$$

Table 4.2 reports all the performance indicators, along with their definition, used in this work. The first set is constituted by the volume-weighted average sizes of the population $L_{1,V}$ and $L_{2,V}$, which are a good indication of whether an improvement in the sizes and morphology of the crystals has been achieved or not. Another set of useful indicators is constituted by $\sigma_{1,V}$ and $\sigma_{2,V}$, which are the volume-weighted variances of the distribution for the two internal coordinates L_1 and L_2 . These quantities can be used as a measure of the polydispersity of the produced powder, since a high value of these indicators would correspond to a large variability in terms of the corresponding characteristic size among the particles.

The amount of fines still present in the final products is also a quantity of interest. In this work, we classify particles as fines when either one or both

dimensions are below $\lambda = 20 \mu\text{m}$. The fraction of fines in the final product can then be calculated as

$$F = \frac{\int_0^\lambda \int_0^\lambda n(L_1, L_2, t) L_1 L_2 dL_1 dL_2}{\mu_{00}} \quad (4.29)$$

Average quantities	
Volume weighted \bar{L}_1 :	μ_{22}/μ_{12}
Volume weighted \bar{L}_2 :	μ_{13}/μ_{12}
Volume weighted $\sigma_{1,V}$:	$\sqrt{\mu_{32}/\mu_{12} - \bar{L}_1^2}$
Volume weighted $\sigma_{2,V}$:	$\sqrt{\mu_{14}/\mu_{12} - \bar{L}_1^2}$

TABLE 4.2: Performance indicators used in this work.

4.3 MATERIALS AND METHODS

4.3.1 *Experimental setup*

Figure 4.1 shows a detailed schematic of the laboratory rig developed and used for the experimental campaign. The plant consists of two jacketed batch crystallizers (LaboTechSystems LTS, Reinach) each with a volume of 2 liters and equipped with an overhead stirrer, and a continuous rotor-stator wet mill IKA MagicLab, whose grinding chamber is equipped with the module MK/MKO (IKA-Werke, Staufen). Both crystallizers and the mill are equipped with a dedicated thermostat (Huber Pilot ONE, Offenburg) for precise temperature control. The three devices are interconnected through a line, inside of which the suspension flows thanks to a peristaltic pump (Ismatec, Wertheim). The configuration allows to perform the experiments in a robust way, avoiding undesired changes of temperature.

4.3.2 *Model compound*

The model compound used throughout the experimental campaign is L-Glutamic acid, namely its β polymorph.

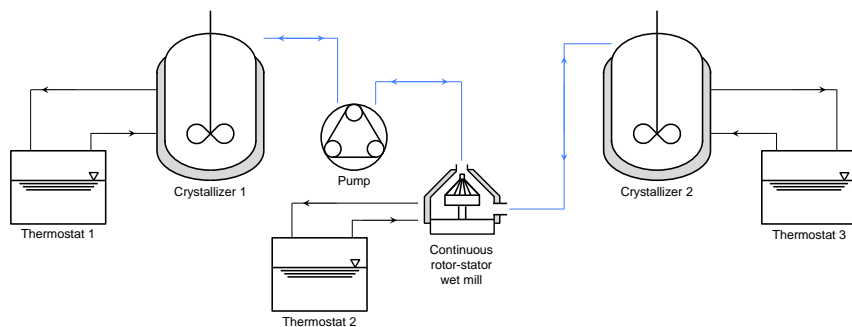


FIGURE 4.1: Scheme of the laboratory setup. Please note that the peristaltic pump can transfer the suspension from Crystallizer 1 to Crystallizer 2 and viceversa.

As widely reported in literature,⁵⁴ L-Glutamic acid exhibits two known polymorphs, the metastable α polymorph and the thermodynamically stable β form. The solubility of both polymorphs in water is shown in Figure 4.2. The needle-like morphology of the stable form, as well as its low solubility in water, make this compound a perfect candidate for our scope.

Crystals are produced through pH-shift precipitation and subsequent polymorphic transformation at constant temperature. First, equimolar amounts of sodium glutamate (NaGlu, Sigma Aldrich, Switzerland, purity $\geq 99\%$) and hydrochloric acid (HCl, Sigma Aldrich, Switzerland, $\geq 37\%$) are mixed in deionized and microfiltered water, obtained using a Milli-Q Advantage A10 device (Millipore, Zug, Switzerland), at $5\text{ }^{\circ}\text{C}$ under continuous stirring at 300 rpm for an hour. The crystals produced are recovered, filtered and dried for 12 hours in a ventilated oven at $45\text{ }^{\circ}\text{C}$. A saturated solution of the α form is prepared at $45\text{ }^{\circ}\text{C}$ by mixing equimolar amounts of NaGlu and HCl; the crystals produced in the previous synthesis step are then added and allowed to transform at constant temperature over a period of 48 hours. The β crystals are then recovered, filtered and dried in a ventilated oven at $60\text{ }^{\circ}\text{C}$ for 24 hours.

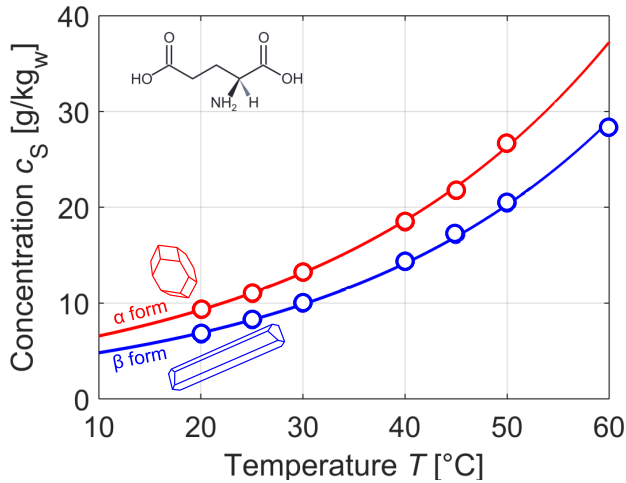


FIGURE 4.2: Solubility of the two polymorphs of L-Glutamic acid in water.

4.3.3 Experimental protocol for 3-stage process experiments

A saturated solution of β L-Glutamic acid in water is prepared at the initial temperature of the first cooling stage T_0 . The required amount m_0 of β crystals per kilogram of water is added to the saturated solution as seeds, to reduce to a minimum extent nucleation events. The temperature is reduced by applying the designed cooling ramp and the corresponding cooling rate γ_C , until the final temperature of the cooling stage is reached. The system is left under stirring conditions until the concentration approaches equilibrium. The suspension is then pumped through the grinding chamber, where milling is performed at the desired intensity by setting the rotor speed θ , and the ground product is collected in the second crystallizer. Here, the system is heated at a rate γ_D until the final temperature of the dissolution stage is reached. This is calculated as the temperature where, once equilibrium is reached, the required mass fraction m_D of the total solid mass suspended at the end of the grinding stage has been dissolved. The stages are then repeated for the established number of times n_C and the final products are filtered and dried for further analysis. Concerning the duration of each stage, we observed via a preliminary set of ATR-FTIR measurements that the time required for equilibration during cooling is approximately twelve hours, while it reduces to three hours for dissolution. We therefore used this as the duration for all the crystallization and dissolution stages. Of

course, this choice impacts productivity of the process, whose optimization is out of the scope of this work.

4.3.4 *Experimental protocol for process comparison experiments*

A single cooling experiment, both with and without milling, has been performed to assess the benefits of the 3-stage process on the size and shape of the final products. A saturated solution is prepared at the same initial temperature T_0 of the 3-stage process and the amount m_0 of β seeds is added. The system is cooled from T_0 to T_F at the same rate used in the 3-stage process characterization experiments and stirred until equilibrium is reached. Crystals are then recovered and dried in the case of no milling, or ground at the desired milling intensity.

4.3.5 *Operating conditions*

The combination of three different unit operations leads to a broad design space, due to the large number of degrees of freedom associated to the operation of each stage in each cycle. Concerning the cooling stage, the population and amount of seeds added, the temperature profile, and the cooling rate are the operating conditions that should be taken into account. The milling stage can be characterized in terms of the milling intensity and of the residence time of the suspension in the grinding chamber. The heating stage requires the definition of the heating ramp and of the amount of mass that is dissolved, which in turns affect the final temperature of this step. At the process level, the initial and final temperature, as well as the overall number of cycles carried out are the operating variables.

It is immediately clear that designing an experimental campaign that could comprehensively investigate the whole design space is very time consuming. Therefore, some generally valid set values for some of these conditions can be chosen, thus leading to a reduced design space. In agreement with the previous work, the initial and final temperature T_0 and T_F of the process are chosen based on the fact that, in industrial pharmaceutical processes, the pure solution comes from a synthesis stage operated at high temperature, and on process constraints on the amount of mass recovered. The seeds used in the first cooling stage are produced through pH-shift transformation according to the procedure described in Section 4.3.2 and the amount added equals 10% of the total mass recovered throughout the process. The cooling ramp adopted is linear with a rate of 0.1 °C/min. The

residence time in the milling chamber is set to 5 s, the minimum allowed by the peristaltic pump used in the experimental campaign. In line with the choices adopted for the cooling stage, the heating ramp is linear and has a rate of $0.1\text{ }^{\circ}\text{C}/\text{min}$. Table 4.3 reports all the conditions fixed throughout the experimental campaign. The three remaining degrees of freedom, namely the milling intensity, the amount of mass dissolved in the heating stage, and the number of cycles have been thoroughly investigated to identify their major effects on product properties.

Concerning the conditions applied for the two process comparison experiments, in order to carry out a fair analysis, the same conditions exploited for the 3-stage process are adopted. As to the single crystallization process, the same amount and type of seeds used for the combined cycles is used, and the difference between initial and final temperature is also the same, along with the cooling profile and the cooling rate. For the milling stage, a rotor speed of 5,000 rpm is applied together with a residence time of 5 seconds.

Process		Stages	
Condition	Set point	Condition	Set point
Initial temp. T_0	$50\text{ }^{\circ}\text{C}$	Crystallization	
Final temp. T_F	$25\text{ }^{\circ}\text{C}$	Temp. drop ΔT_C	$(T_0 - T_F) / nC$
Compound	β LGA	Cooling rate γ_C	$0.1\text{ }^{\circ}\text{C}/\text{min}$
Seeds mass m_0	$1\text{ g}/\text{kg}_w$	Milling	
Seeds	pH-shift prod.	Residence time τ	5 s
N° cycles	varying	Rotor speed θ	varying
		Dissolution	
		Mass dissolved m_D	varying
		Heating rate γ_D	$0.1\text{ }^{\circ}/\text{min}$

TABLE 4.3: Process operating conditions. The temperatures at the end of each cooling stage can be calculated from the data in the table. For example, if two cycles are performed, the set point temperatures of the cooling stages would be $37.5\text{ }^{\circ}\text{C}$ and $25\text{ }^{\circ}\text{C}$, while if five cycles are performed, they would be $45\text{ }^{\circ}\text{C}$, $40\text{ }^{\circ}\text{C}$, $35\text{ }^{\circ}\text{C}$, $30\text{ }^{\circ}\text{C}$, and $25\text{ }^{\circ}\text{C}$.

4.3.6 *Measurement techniques*

In order to compare the results of simulations and experiments, it is necessary to measure the length and width of the real particles suspended in the crystallizer. To this aim, an in-house built opto-mechanical measurement device, the μ -DISCO, has been used. The system consists of two cameras, equipped with telecentric lenses, capable of capturing images along two orthogonal planes at a frame rate of 5 fps. An image analysis routine allows to identify and separate the silhouettes of the different particles from the background. The contours of each silhouette are matched and a visual hull is reconstructed. This feature is used to automatically assign the particles to pre-defined shape classes (cuboids, needles, spheres, agglomerates, and non-convex) hence to evaluate their characteristic sizes. Concerning needle-like particles, the length L_1 and width L_2 are used in agreement with the generic particle model to reconstruct the PSD of the ensemble of crystals. Further details are reported in Rajagopalan et al.⁵¹ In this work, the measured PSDs are based on the measured size and shape of about 10,000 crystals. Due to the high suspension densities reached throughout the process, measurements are performed offline, mixing a representative sample of crystals (approximately 0.5 grams) with 500 grams of ethanol.

A Leica 8000 M microscope has also been used to collect high-quality pictures of crystals for a better visualization and comparison of their morphology and their surface structure. Both $5\times$ and $10\times$ magnification have been used; the relative scale bar is reported in each picture.

4.4 RESULTS AND DISCUSSION

4.4.1 *Feasibility and experimental reproducibility*

In order to verify the possibility of accurately repeating experiments, as well as of producing crystals whose average sizes fulfill the desired specifications, three tests have been performed under the reference conditions reported in the first row of Table 4.4. The target region (grey area in Figure 4.3) has been defined by the following constraints on the average aspect ratio, i.e. $\Phi \leq 5$, length, i.e. $L_{1,V} \leq 500 \mu\text{m}$, and width, i.e. $L_{2,V} \geq 100 \mu\text{m}$, of the crystals. Concerning the specifications on the products, the values adopted are chosen for $L_{2,V}$ and Φ so that the final average width L_2 of the crystals is larger than the initial one, by retaining at the same time a compact

morphology. The maximum value of $L_{1,V}$ is back-calculated from the other two constraints.

Experiment ID	Operating conditions		
	θ [rpm]	m_D [%]	n_C [-]
Reference	5,000	40	3
Mill 1	12,000	40	3
Mill 2	20,000	40	3
Mill 3	25,000	40	3
Cycle 1	5,000	40	4
Cycle 2	5,000	40	6
Mass 1	5,000	60	3
Mass 2	5,000	80	3
Heuristic Optimum	8,000	40	5
Single Cooling	N.A.	N.A.	N.A.
Cooling + milling	5,000	N.A.	N.A.

TABLE 4.4: Operating conditions of the experimental runs. In all the cases, the remaining operating conditions are those reported in Table 4.3

The average sizes of the crystals obtained at the end of these three experiments are plotted as the three colored circles in the L_1L_2 -plane shown in panel (b). The small difference between the outcome of the three experimental runs demonstrates the possibility of accurately reproducing the experiments; such difference is reasonable and acceptable when considering the large number of process steps involved and the inherent and inevitable propagation and amplification at each step of possible experimental errors. The green triangle, whose vertices correspond to the outcome of the three experiments, defines the region where the outcome of the process performed under the specified conditions belongs. In order to further verify experimental reproducibility, the particle size and shape distributions of two of the three experiments have been compared as shown in panel (c) of Figure 4.3. The overlapping of the two populations and of their contour lines confirms once again the consistency between the different runs of the process.

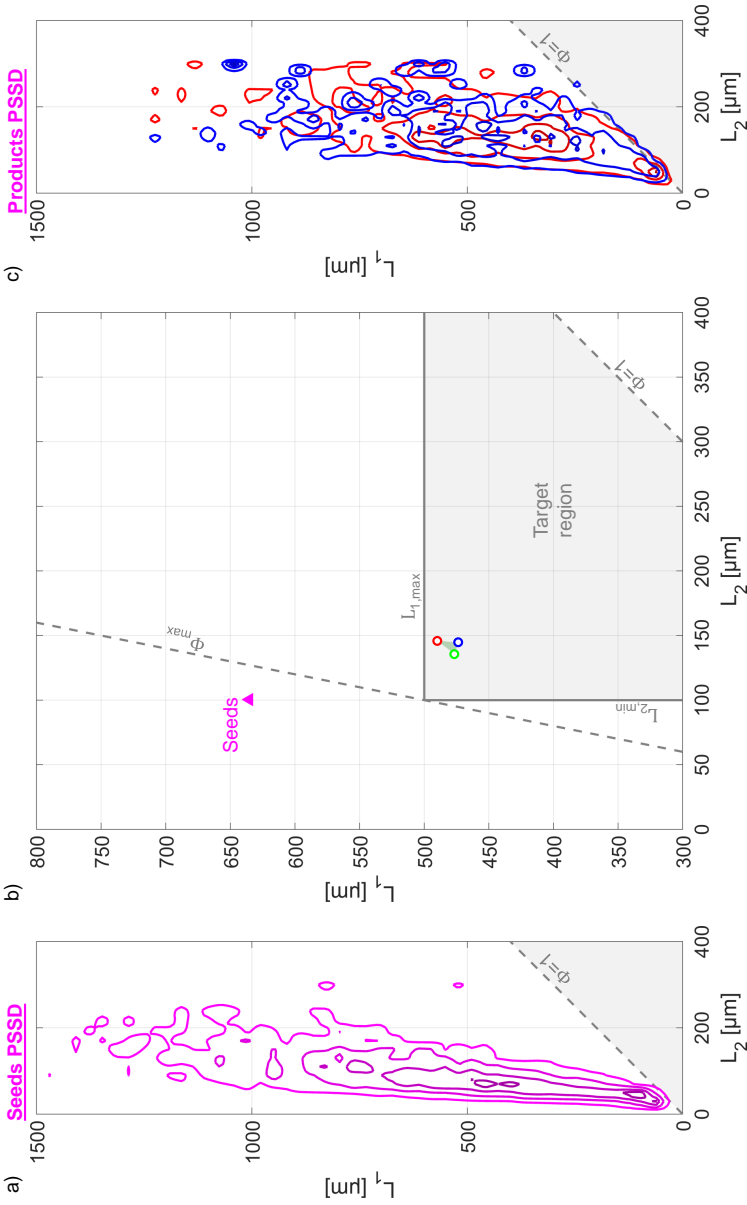


FIGURE 4.3: Outcome of the set of three experiments performed to assess experimental reproducibility. In panel (b), the average sizes of the seeds and the products are reported as the green triangle and the colored circles respectively. The target region, corresponding to the grey area in the L_1 - L_2 -plane is also shown. In panels (a) and (c) the PSSDs of the seeds and products are reported.

Concerning feasibility, the process performed adopting the operating conditions listed in Table 4.4 proved to be capable of producing crystals fulfilling the given specifications.

4.4.2 *Experimental analysis and assessment of the 3-stage process*

In the following, the results of experiments carried out to investigate the effect of the mill rotor speed, the number of cycles, and the amount of mass dissolved on the properties of the final particles are presented. The experimental conditions for each of the experiments performed are reported in Table 4.4.

The effect of the operating conditions on the product properties can be understood by analyzing their PSSDs, shown in Figure 4.4. Here, the particle size and shape distributions for the experiments aimed at investigating the effect of a higher milling intensity (Mill_1), of a larger number of cycles (Cycle_1), and of a larger fraction of mass dissolved during heating (Mass_1) are shown. It is readily observed that not only the 3-stage process affects the average sizes of the population, but also the whole PSSD, thus leading to products with different distributions of sizes and shapes. A large amount of information is contained in the contour plots used to illustrate the PSSD in Figure 4.4, which can be summarized by the values of the average properties in Figure 4.5, namely average sizes in panel (a) and average broadness in panel (b). Here, the green triangle, labeled as a reference, is an average of the three experiments presented in Section 4.4.1. A thorough analysis of the effect of each operating condition investigated is therefore carried out by considering both the experimental data and the process simulations, in terms of these average properties.

The average sizes of the products, are shown in panel (a) of Figure 4.5. Here, the symbols, connected by a dotted line serving as a guide to the eye, represent the outcome of the experiments aimed at characterizing the effect of the rotor speed, θ (blue), of the number of cycles, n_C (red), and of the mass dissolved, m_D (orange). The filled fuchsia circle represents the outcome of a simulation performed under the same operating conditions adopted for the experiments described in the previous section. The solid lines represent the results of the simulations performed with the model presented in Section 4.2.1 varying the three parameters above in the same range of the experimental campaign (15 simulations for the blue and orange line, 5 simulations for the red line).

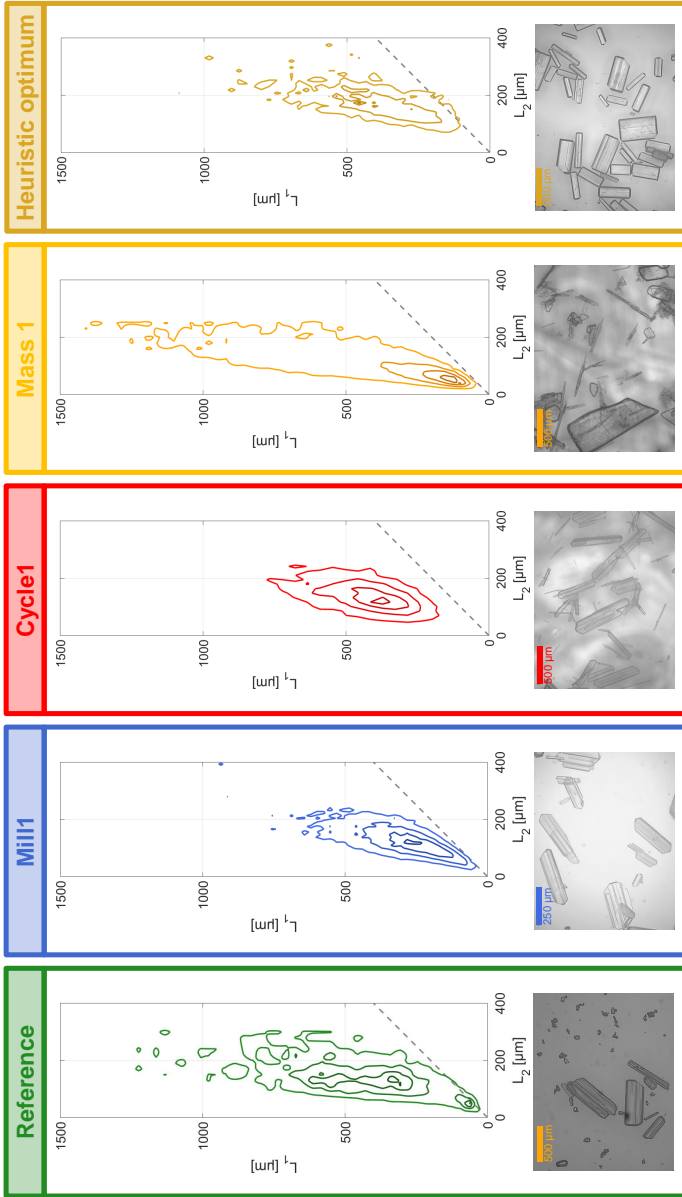


FIGURE 4-4: Effect of rotor speed, mass dissolved, and number of cycles on average product properties as illustrated by the average particle sizes at the end of each corresponding experiment or simulation in panel (a) and $\sigma_{1,V}$ and $\sigma_{2,V}$ in panel (b). The solid lines represent the results of process simulations, carried out for about 15 different values of the reported parameter, while the open symbols, connected by a dotted line as a guide to the eyes, correspond to the measured experimental outcome.

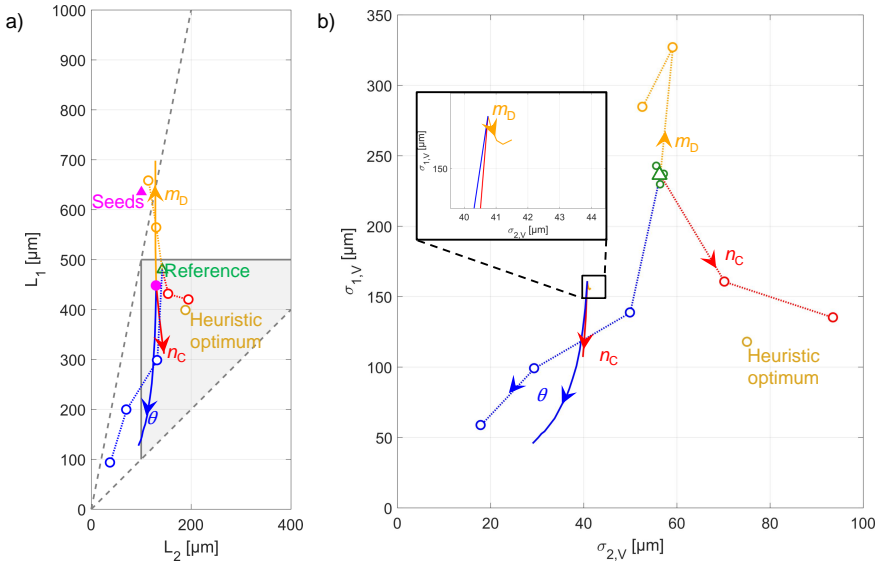


FIGURE 4.5: Effect of rotor speed, mass dissolved, and number of cycles on average product properties as illustrated by the average particle sizes at the end of each corresponding experiment or simulation in panel (a) and $\sigma_{1,V}$ and $\sigma_{2,V}$ in panel (b). The solid lines represent the results of process simulations, carried out for about 15 different values of θ and m_D and 5 values of n_C , while the open symbols, connected by a dotted line as a guide to the eyes, correspond to the measured experimental outcome. The three green circles represent the outcome of the three repetitions for the reference experiment (see Figure 4.3 for the corresponding average sizes), while the green triangle represents their average.

The experimental and simulation trends are in good qualitative agreement. High values of rotor speed θ can be used to significantly reduce the average size $L_{1,V}$, but at the price of favoring also undesired breakage along the width, thus reducing also $L_{2,V}$. Performing more cycles allows to obtain more compact crystals, since $L_{1,V}$ reduces and $L_{2,V}$ becomes larger at the same time, due to the repeated milling action and the lower values of supersaturation achieved during each cooling step. Dissolving more mass leads to very elongated crystals no longer fulfilling the product specifications.

Increasing the rotor speed θ not only produces smaller crystals, but also leads to more compact distributions. On the other hand, increasing the

number of cycles leads to a powder with reduced variability in crystals' length but larger variability in crystals' width. This effect can be justified by considering that more milling stages are performed on crystals with a larger L_2 , hence favoring the breakage along this dimension. The trend observed experimentally when increasing the mass dissolved exhibits a maximum for both $\sigma_{1,V}$ and $\sigma_{2,V}$. This can be explained by considering that increasing the mass dissolved leads to higher and higher levels of supersaturation during cooling, to the formation of more and more nuclei, and to the removal of more and more crystals during dissolution, until eventually, for $m_D=100\%$, the distribution would correspond to that obtained via unseeded crystallization from a homogeneous solution.

In panel (b) of Figure 4.5, a comparison between the experimental and simulated $\sigma_{1,V}$ and $\sigma_{2,V}$ is also carried out. Here, the three green circles represent the outcome of the three repetitions of the reference experiment (see Figure 4.3 for the corresponding average sizes); the green triangle represents the average of the three repetitions. Their relative position gives an indication of the experimental uncertainty, which is also in the case of the broadness of the PSSD as in the case of the average sizes very small. Concerning the effect of the rotor speed θ on these properties, the model and the experiments show a good qualitative agreement. However, the simulations underestimate the effect of the number of cycles n_C on $\sigma_{2,V}$, for which no significant effect is observed in the calculations, in contrast with the relevant variation observed throughout the experiments. Furthermore, the model also predicts a reduced effect of the mass dissolved m_D on both $\sigma_{1,V}$ and $\sigma_{2,V}$, whereas the experiments exhibit a characteristic and detectable trend. This discrepancy cannot be simply justified as an experimental error (as shown above) but might be explained by considering three aspects. The first concerns the kinetics implemented in the model, which are not representative of the specific system used and therefore can not make the model a fully predictive tool. Estimating the specific kinetics at this stage is however beyond the scope of this work. The second aspect concerns the properties $\sigma_{1,V}$ and $\sigma_{2,V}$ themselves, as they are calculated through high-order moments μ_{ij} , which are difficult both to predict using a model and to measure experimentally.⁷⁷ While the average sizes depend on the low-order moments and are easy to predict once the physical phenomena are correctly taken into account (i.e. growth, breakage, etc.), describing the evolution of $\sigma_{1,V}$ and $\sigma_{2,V}$ would require the precise modeling of phenomena that cannot be known a priori and that bear no general validity (i.e. growth rate dispersion, breakage mechanism, etc.). Finally, the third

aspect concerns the complex interplay between the different phenomena, the operating conditions, and the combination of different unit operations. To better clarify this point, in a separate set of calculations not reported here for brevity, we performed an in-silico sensitivity analysis where the secondary nucleation rate J_{Sec} has been increased while keeping all the other conditions and kinetic parameters constant; we have observed that the output of the model is extremely sensitive to such rate, both quantitatively and qualitatively, with the resulting $\sigma_{1,V}$ and $\sigma_{2,V}$ attaining very different values and exhibiting significantly different trends for different levels of J_{Sec} .

All the effects described above can be observed visually in the set of microscope pictures provided in Figure 4.4 along with the PSSDs. For each of them, the scale bar is provided inside the corresponding images. Despite the possibility of observing all the phenomena described in the previous paragraph, we should not forget that these images are only complementary to the information contained in the PSSDs, which allow to quantify the properties of interest based on a statistically relevant number of sampled crystals and that are therefore of fundamental importance for a correct assessment of the process outcome.

4.4.3 *Heuristic optimum experiment*

An experiment has been performed in order to assess the observation, made using the model, that combining moderate milling intensities and a large number of cycles allows to achieve the best compromise; the corresponding operating conditions are reported in Table 4.4. The values have been chosen based on the considerations reported in detail earlier,³⁴ where the tradeoffs between the different objectives of the process were analyzed, as well as on the experimental observations collected throughout the experimental campaign reported in this work. Since only rotor speeds between 5,000 rpm and 12,000 rpm ensure that the final products belong to the target region, the chosen value of 8,000 rpm for the heuristic optimum experiments represents a reasonable intermediate value. The choice of the percentage of mass dissolved, namely the 40%, ensures that enough fines are dissolved and nucleation is contained, as highlighted in Section 4.4.2. The outcome of the selected experiment is illustrated in Figures 4.4 and 4.5.

In panel (a) of Figure 4.5, it is possible to see how the average length L_1 of the product decreased, due to the effect of moderate milling intensities, while the average width L_2 significantly increased due to the high num-

ber of cycles performed, namely 5. These results are in semi-quantitative agreement with the simulations. Furthermore, panel (b) shows the variances $\sigma_{1,V}$ and $\sigma_{2,V}$ of the particle size and shape distribution of the products. Also in this case, the properties of the final powder are a combination of those observed by tuning the single operating conditions. The PSSD as measured at the end of the process, shown in Figure 4.4, demonstrates the possibility of operating the 3-stage process in order to obtain particles with an improved morphology, as observable in the microscope picture, and a more monodispersed powder.

Figure 4.6 plots the percentage of fines in the product F against the increment in average width ΔL_2 . The heuristic optimum can be seen as a representative outcome of the 3-stage process, combining at the same time a reduced presence of fines granting with a significant improvement in the morphology of the crystals due to the larger L_2 reached. We believe that this proves the suitability of this novel technology for the selective manipulation of β L-Glutamic acid crystal habit.

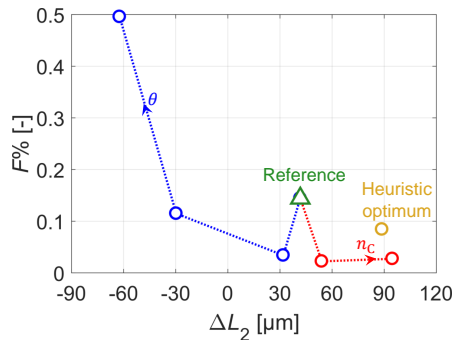


FIGURE 4.6: Fraction of fines present in the final products as a function of the increment in average width achieved at the end of the different experiments.

4.4.4 Comparison with other processes

In order to assess the benefits on the particle size and shape distribution, as well as on the morphology of the individual crystals, granted by the 3-stage process, it is necessary to compare the powder produced in this process, in particular that obtained in the reference case, with that produced at the end of a single cooling stage, operated under the same conditions as the

3-stage process, and that obtained after milling at 5,000 rpm the crystals obtained at the end of such cooling crystallization step. In Figure 4.7, where the results are illustrated, the heuristic optimum experiment for the 3-stage process is also reported for the sake of comparison.

In panel (a), the comparison among the average sizes obtained at the end of each different process shows that the target region can be reached only if a milling stage is also included. However, further information concerning the quality of the products can be obtained from panel (b) and (c), where the broadness along both L_1 and L_2 , as well as the particle size and shape distributions for each of the experiments are reported. Despite the requirements on the sizes being fulfilled for both the milling and the 3-stage process, the distribution obtained by a single cooling stage and subsequent milling is characterized by a more pronounced polydispersity, due to the larger values of $\sigma_{1,V}$ and $\sigma_{2,V}$ as reported in panel (b). This evidence is also confirmed by the comparison of the microscope pictures of the crystals produced in the different processes, clearly highlighting how the repeated dissolution and crystallization cycles effectively help in removing the fine particles. Furthermore, the improvement achieved with the 3-stage process is even more striking when the outcome of the two alternative simple processes are compared with the heuristic optimum experiment. The comparison of microscope images allows to investigate features of the crystals which are hardly accessible when using the mathematical model to investigate the process. Another important difference between the particles produced is their quality in terms of smoothness of the surface and regularity; it appears that the crystals produced at the end of the 3-stage process are less indented than those produced by cooling and by milling, as well as less jagged than the seeds. This effect is mainly due to the healing effect induced by the series of dissolution and subsequent crystallization stages carried out in the novel 3-stage process.

In light of the results obtained, it is possible to confirm that the 3-stage process effectively leads to a product powder of β L-Glutamic acid crystal with improved properties.

4.5 CONCLUSIONS

In this work, for the seeded crystallization of β L-Glutamic acid in water, we have investigated a novel 3-stage cyclic process aimed at tuning the aspect ratio of the product crystals. The process consists of a combination of crystallization, milling, and dissolution steps through a dedicated and

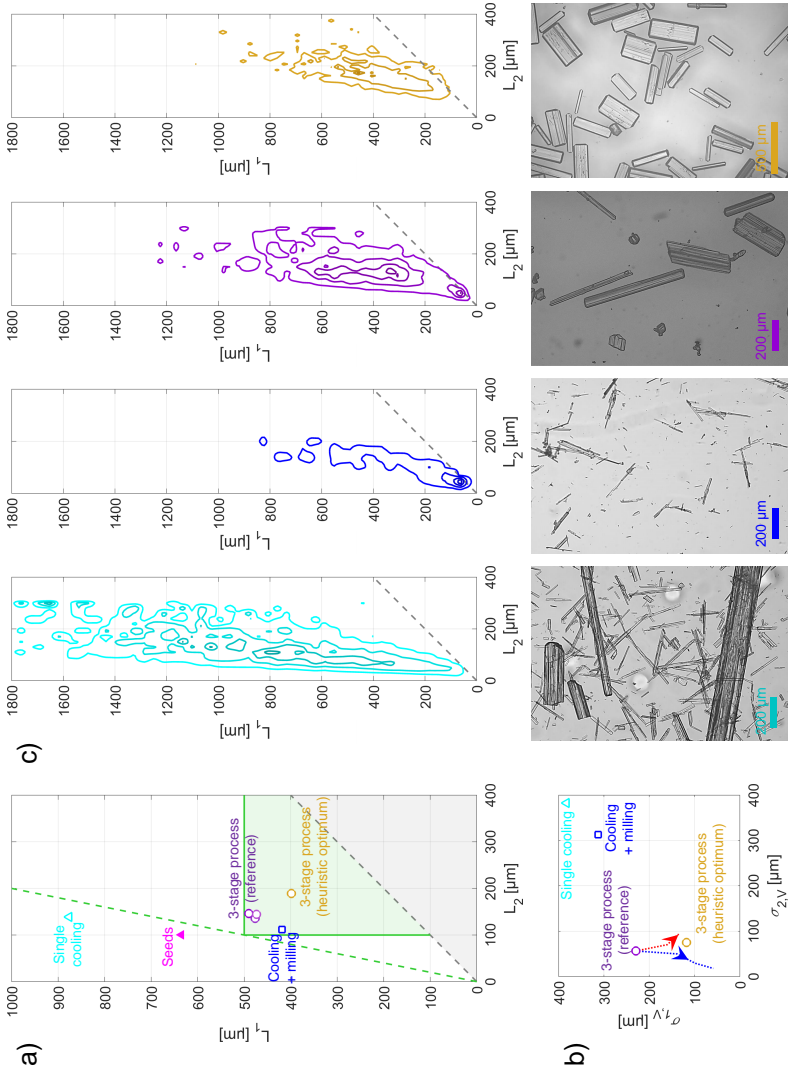


FIGURE 4-7: Detailed comparison between the outcome of the 3-stage process and a single cooling step with and without final milling. In (a), the comparison is carried out in terms of average sizes, while in (b) the $\sigma_{1,V}$ and $\sigma_{2,V}$ are plotted. In panel (c) the PSSDs for the simple cooling without (aquamarine) and with (blue) final milling, as well as the reference case (purple) and the heuristic optimum (gold) of the 3-stage process, along with corresponding microscope pictures, are shown.

comprehensive experimental campaign to confirm the conclusions reached using a specifically developed mathematical model and described in detail earlier.³⁴

First, the reproducibility and repeatability has been verified by repeatedly performing the process under the same operating conditions. Then, the effect of the rotor speed, the number of cycles, and the mass dissolved during the heating step has been investigated with a back-to-back comparison of experiments and simulations to analyze and understand the trends observed. The comparison showed that there is a good agreement between the trends measured and those simulated for the average sizes, less good for the broadness of the PSSD (which is admittedly more difficult to measure and predict).

With the aim of obtaining crystals with an improved morphology, a new experiment has been carried out under operating conditions that have been optimized heuristically. Such conditions have been selected based on the observation obtained with the model and on the results of the previous experimental campaign, and combine mild milling intensities and a large number of cycles. The results confirmed that the produced crystals exhibit a more equant shape, in agreement with the model qualitative predictions. The outcome has also been compared with those of a cooling stage, both with and without final milling, thus showing how the 3-stage process is the only process capable of producing crystals with the most compact morphology and with a width larger than that of the seeds.

Despite the promising results obtained, a few points remain open. The first concerns the effective possible implementation of the 3-stage process at the industrial scale. The data collected, as well as the model, do not allow to understand whether the increased process time can be counterbalanced by a reduced time required in the downstream processing of the powder.

The second related point concerns the lack of a quantitative correlation between the size and shape of the crystals and their processability (i.e. filterability, flowability, etc.). This would be very useful, as it would allow to make a better choice of the size and shape of the crystals based on the corresponding processability and not merely on heuristic considerations.

The third and last point concerns the potential of the 3-stage process for scale-up to industrial applications. This should be attractive in light of what we have demonstrated here and elsewhere,³⁴ i.e. its potential for tuning the PSSD of the product particles. However, the complexity of the 3-stage process leads to a large design space, whose exploration, to identify optimal operating conditions, might be very demanding in the design and

development phase of a new industrial process, namely for reasons of time and lack of materials. In this context, the role of the mathematical model, which has been demonstrated to be able to capture the key trends in the effect of the operating conditions on product quality, is extremely important in guiding decisions during the process synthesis and design phases. Nevertheless, scale-up of this process constitutes without doubt a challenge, that calls for new developments: on the one hand the study of new design methods, which enable an efficient exploration of the design space; on the other hand the application of on-line control techniques, supported by the use of the μ -DISCO monitoring instrument.

4.6 NOTATION

B	birth term in the PBE	$[\mu\text{m}^{-2} \text{kg}^{-1} \text{s}^{-1}]$
c	solute concentration in the liquid phase	$[\text{g kg}^{-1}]$
c_0	initial solute concentration in the liquid phase	$[\text{g kg}^{-1}]$
c^*	solubility	$[\text{g kg}^{-1}]$
C	number of cycles	$[-]$
D_i	dissolution rate for dimension i	$[\mu\text{m s}^{-1}]$
E	death term in the PBE	$[\mu\text{m}^{-2} \text{kg}^{-1} \text{s}^{-1}]$
F	number fraction of fines	$[-]$
g_i	daughter distribution of the fragments along the i -th dimension	$[\mu\text{m}^{-1}]$
\mathbf{G}	vector of rates of change	$[\mu\text{m s}^{-1}]$
G_i	growth rate for dimension i	$[\mu\text{m s}^{-1}]$
\mathbf{k}_G	vector of growth rate parameters	[varies]
\mathbf{k}_{Hom}	vector of homogeneous nucleation rate parameters	[varies]
\mathbf{k}_{Het}	vector of heterogeneous nucleation rate parameters	[varies]
\mathbf{k}_{Sec}	vector of secondary nucleation rate parameters	[varies]
\mathbf{k}_M	vector of breakage frequency parameters	[varies]
k_v	shape factor	$[-]$
K_i	breakage frequency for dimension i	$[\text{s}^{-1}]$
J	nucleation rate	$[\text{kg}^{-1}\text{s}^{-1}]$
L_i	crystals characteristic dimension i	$[\mu\text{m}]$
m_M	mass of the rotor	$[\text{g}]$
n	number density function	$[\mu\text{m}^{-2} \text{kg}^{-1}]$

n_0	PSD of seed crystals	$[\mu\text{m}^{-2} \text{kg}^{-1}]$
N_P	power number	[-]
S	supersaturation	[-]
t	time	[s]
T	temperature	$[\text{°C}]$
γ_C	cooling rate	$[\text{°C min}^{-1}]$
γ_H	heating rate	$[\text{°C min}^{-1}]$
$\delta(L_i)$	Dirac's delta function	$[\mu\text{m}^{-1}]$
ϵ	power input	$[\text{W kg}^{-1}]$
Φ	aspect ratio	[-]
μ_{ij}	cross moment ij of the PSSD	[varies]
ρ	density of the crystalline phase	$[\text{kg m}^{-3}]$
$\sigma_{i,v}$	volume weighted standard deviation in the L_i direction	$[\mu\text{m}]$
τ	residence time in the mill	[s]
θ	rotor speed	[rps]

EFFICIENT ASSESSMENT OF A COMBINATION OF CRYSTALLIZATION, MILLING, AND DISSOLUTION STAGES FOR PARTICLE SIZE AND SHAPE MANIPULATION

5.1 INTRODUCTION

Crystallization is one of the most used separation and purification processes in the pharmaceutical and food industry. The properties of the crystals, such as their polymorphism and their morphology, are important both for their behavior in the downstream processes^{97–101} and for the quality of the final commercialized products.^{102–106} In particular, the size and the shape of the crystals are known to significantly impact the performance of steps as filtration and tableting, thus rising interest in developing methods to directly manipulate the particle morphology at the crystallization stage. Currently, two are the major alternatives available. The first involves the use of additives, to modify how the solute molecules are integrated onto specific crystal facets.¹⁰⁷ Numerous studies have proven how the same compound can exhibit significantly different morphologies depending on the type of additive used and on its amount.^{16,66,108–110} However, the additives that can be exploited in pharmaceutical processes are regulated and strongly limited by their impact on human health, thus restricting the possibility of effectively manipulating crystal morphology and their application in industrial processes. Therefore, the most widespread industrial technique exploited to manipulate crystal habit is milling. Here, mechanical force is applied to break the individual crystals and to obtain more equantly shaped particles. However, the high stresses induced by the forces applied and the strong temperature increment experienced by the solid particles may lead to undesired solid-state transformations,^{41,111,112} which would alter the properties of the final product. Furthermore, the large amount

Binel P., Salvatori F. and Mazzotti M., A robust and efficient approach for the investigation of combined crystallization, milling, and dissolution stages, *Chemical Engineering Science X*, 2018, *In press*.

of fines formed during breakage represents a problem during filtration,¹¹³ leading to long process times with a higher risk of product decomposition.

In previous publications^{34,36} we have investigated the possibility of combining crystallization, milling, and dissolution stages into a new process, called 3-stage process, to selectively manipulate the size and shape of crystals while mitigating the drawbacks characteristic of each unit operation. The strategy underlying the new technology is to let crystals grow under typical crystallization conditions and to subsequently mill them, breaking them mainly along their shorter dimension, thus producing more compact crystals. The fine particles formed are then dissolved and the excess of solute in the liquid phase is recovered by repeating these three steps cyclically. A first assessment of the process analyzing the qualitative trends in terms of average sizes and dispersity of the distribution was carried out by performing an in-silico investigation.³⁴ The mathematical model used to carry out the study was structured so as to specifically describe the phenomena occurring during each stage, but it was not fitted to a specific substance, in order to keep the observation as generally valid as possible. The effect of a subset of the most important operating conditions was thoroughly analyzed and some heuristic optimum conditions were identified. More recently, a comprehensive set of experiments has been performed to assess the results of the simulations and to verify the possibility of effectively tuning particle morphology in practice.³⁶ The results highlighted how the process, when applied to β L-Glutamic acid, can effectively produce particles satisfying the product specifications, thus yielding product particles with a quality superior to that of the crystals obtained via more conventional processes. However, the study has also highlighted how the productivity of the 3-stage process is significantly lower than that of the other processes analyzed for comparison. Furthermore, process characterization requires a large effort when it comes to estimating the set of process outcome for different, newly explored compounds.

Despite being aware of the great potential of the 3-stage process in changing particle size and shape, we are also aware of its shortcomings, especially concerning its implementation to compounds with very different properties, its time consuming characterization, and its reduced productivity. Therefore, in this work, we aim at specifically tackling these problems, by providing a shortcut method with a reduced characterization effort, to assess the potential and feasibility of the 3-stage process when applied to new systems. To do so, we apply the methodology developed in the previous publications, both for simulations and experiments, extending it

to the whole range of operating conditions that can be effectively applied, using the available experimental setup. Both a new set of simulations and a new set of experiments, involving also a new compound for which no information on the characteristic growth or dissolution kinetics is readily available, are performed; we analyze and exploit the results from a completely new perspective. The paper is structured as follows. In Section 5.2 the mathematical model is presented, along with the fitting procedure for parameter estimation, the method adopted to identify the required set of experiments, and the theoretical evidence at the basis of the proposed approach. In Section 5.3, the model compounds and the experimental setup are described and the procedure to perform the laboratory tests is reported in detail. In Section 5.4 the experimental evidence is reported, analyzed, and discussed, focusing on the quantity and type of information that can be collected throughout the experimental campaign and how it can be exploited during the process design stage. Finally, Section 5.5 draws conclusions.

5.2 THEORY

The aim of this work is to develop a robust and effective strategy to investigate the 3-stage process and to understand under which operating conditions it should be operated for the specific system considered. In this section, the theoretical basis of the approach developed and proposed is presented; the results of such in-silico analysis will guide the experimental assessment. First, the mathematical model, based on morphological population balance equations (MPBEs),⁴⁵ and capable of tracking the evolution of the whole particle ensemble in terms of the size and shape of its crystals, is presented. The model is hence used to simulate the process under a broad range of operating conditions, and of different compound-specific properties, to explore its application and potential for different systems. The results of these simulations are analyzed to identify general, system-dependent features, which constitute the basis of a compound-specific strategy for the identification of heuristically optimal operating conditions.

5.2.1 *Mathematical modeling of the 3-stage process*

5.2.1.1 *Crystal model*

The multi-faceted nature of crystals requires models capable of correctly capturing these important features. Convex polytopes^{21,114,115} can describe

the different surfaces exposed by the single crystals, but their use in MPBEs would require not only a large computational effort, but also measurement tools capable of identifying the different facets of the particles constituting the whole ensemble and of measuring a statistically relevant sample in a short period of time. To overcome these drawbacks, and in agreement with the measurements made with the μ -DISCO (see Section 5.3.4), the generic particle model^{33,51,116} is adopted in this work. Particles are approximated as cylinders with length L_1 and width L_2 , with their shape represented by the aspect ratio $\Phi = L_1/L_2$. The particle ensemble is modeled using the particle size and shape distribution (PSSD), where the double differential $n(L_1, L_2, t)dL_1dL_2$ represents the number of crystals with length $L_1 \in [L_1; L_1 + dL_1]$ and width $L_2 \in [L_2; L_2 + dL_2]$ per unit mass of solvent.

5.2.1.2 MPBE for the crystallization stage

The MPBE for a well-stirred batch crystallizer, where no breakage and no agglomeration occur, reads as follows:

$$\frac{\partial n}{\partial t} + \frac{\partial (G_1 n)}{\partial L_1} + \frac{\partial (G_2 n)}{\partial L_2} = J_N \delta(L_1) \delta(L_2) \quad (5.1)$$

$$n(L_1, L_2, t = 0) = n_0(L_1, L_2) \quad (5.2)$$

$$n(L_1 = 0, L_2, t) = 0 \quad (5.3)$$

$$n(L_1, L_2 = 0, t) = 0 \quad (5.4)$$

Here, G_1 and G_2 represent the growth rates along the internal coordinates L_1 and L_2 , while the term $J\delta(L_1)\delta(L_2)$ represents the formation of new crystals, due to nucleation events, of size $L_1 = L_2 = 0$. Equation 5.2 is the initial condition for Equation 5.1 and $n_0(L_1, L_2)$ represents the particle size and shape distribution of crystals at the beginning of the cooling stage, whereas Equations 5.3 and 5.4 are its boundary conditions.

Equation 5.1 is coupled with a mass balance for the solute concentration in the liquid phase, c , which under the assumption of constant mass of solvent reads as

$$\frac{dc}{dt} = -k_V \rho \frac{d\mu_{12}}{dt} \quad (5.5)$$

$$c(t = 0) = c_0 \quad (5.6)$$

Here, k_V is the shape factor, equal to $\pi/4$ for cylinders, and μ_{12} is the cross-moment of the particle size and shape distribution, which is directly

proportional to the mass of crystals suspended per unit mass of solvent. The supersaturation S , in the case of either mild non-idealities or negligible effect of the composition on the activity coefficient of the solute, can be defined as the ratio between the concentration of solute in solution and its solubility at the temperature T :

$$S = \frac{c}{c^*(T)} \quad (5.7)$$

The constitutive equations for growth and nucleation, both primary and secondary, have been adapted from Ochsenbein et al.,⁷⁷ Ploss et al.,⁷³ and derived from the classical nucleation theory.

$$G_i = k_{G,i1} \exp\left(-\frac{k_{G,i2}}{T}\right) (S-1)^{k_{G,i3}} \quad \text{with } S > 1 \quad (5.8)$$

$$J_N = J_S + J_{He} + J_{Ho} \quad (5.9)$$

$$J_S = k_{S,1} \epsilon^{k_{S,2}} m_S^{k_{S,3}} \bar{G}^{k_{S,4}} \quad (5.10)$$

$$J_{Ho} = k_{Ho,1} \exp\left(-\frac{k_{Ho,2}}{\ln^2 S}\right) \quad (5.11)$$

$$J_{He} = k_{He,1} \exp\left(-\frac{k_{He,2}}{\ln^2 S}\right) \quad (5.12)$$

$$(5.13)$$

Here, ϵ is the power input, m_S the suspension density, \bar{G} is the average growth rate, calculated as $(G_1 + G_2) / 2$. This is an arbitrary choice, provided the ambiguity of the original definition of $G = dL/dt$, that we however believe has no significant impact on the outcome of the simulations performed.

5.2.1.3 MPBE for the milling stage

The MPBE for a continuous rotor-stator wet mill, under the assumption of perfectly segregated flow (i.e. the grinding chamber is assumed to be a tubular apparatus), constant supersaturation, and isothermal conditions, reads as:³⁵

$$\frac{\partial n(L_1, L_2, \tau)}{\partial \tau} = B_1 + B_2 - D \quad (5.14)$$

$$B_1 = \int_{L_1}^{\infty} K_1(x, L_2)n(x, L_2, \tau)g_1(L_1, x)dx \quad (5.15)$$

$$B_2 = \int_{L_2}^{\infty} K_2(L_1, x)n(L_1, x, \tau)g_2(L_2, x)dx \quad (5.16)$$

$$D = K_1(L_1, L_2)n(L_1, L_2, \tau) + K_2(L_1, L_2)n(L_1, L_2, \tau) \quad (5.17)$$

$$n(L_1, L_2, \tau = 0) = n_0(L_1, L_2) \quad (5.18)$$

The functions K_i and $g_i(L_i, x)$ are called breakage frequency and daughter distribution respectively and are used to model how fast the particles are breaking and the size of the fragments formed according to the type of mechanism underlying the breakage events. The functional forms adopted in this work are:

$$K_1 = p_{11}m_M(\theta r_M)^2 \left(\frac{L_1}{L_{\text{ref},1}}\right)^{p_{12}} \left(1 + \exp\left(-\frac{L_1 - p_{13}}{L_{\text{ref},2}}\right)\right)^{-1} \frac{\Phi}{\Phi + p_{14}} \quad (5.19)$$

$$K_2 = p_{21}m_M(\theta r_M)^2 \left(\frac{L_2}{L_{\text{ref},1}}\right)^{p_{22}} \left(1 + \exp\left(-\frac{L_2 - p_{23}}{L_{\text{ref},2}}\right)\right)^{-1} \frac{p_{24}}{p_{24} + \Phi} \quad (5.20)$$

$$g_1(L_1, x) = \frac{2}{x} \quad (5.21)$$

$$g_1(L_2, x) = \frac{2L_2}{x^2} \quad (5.22)$$

Here, $\Phi = L_1/L_2$ represents the aspect ratio of the particle that is breaking, while $g_i(L_i, \eta)$ represents the number of fragments of size L_i formed when a particle of size η breaks. It is worth noting that Equation 4.21 corresponds to breakage events yielding two fragments exhibiting a homogeneous distribution of lengths L_1 , whereas Equation 4.21 corresponds to breakage events yielding two fragments exhibiting a homogeneous distribution of cross sectional areas $\pi L_2^2/4$. Note that $L_{\text{ref},1} = 1000 \mu\text{m}$ and $L_{\text{ref},2} = 1 \mu\text{m}$ are used to provide numerical stability when solving the population balance equation. For a deeper analysis of the functional forms chosen and the physics underlying the breakage of needle-like crystals in a continuous rotor-stator wet mill, the reader is referred to the original paper³⁵ or to Chapter 2.

5.2.1.4 MPBE for the dissolution stage

The MPBE for the batch, well-mixed dissolution stage is similar to that presented for the crystallization stage:

$$\frac{\partial n}{\partial t} + \frac{\partial (D_1 n)}{\partial L_1} + \frac{\partial (D_2 n)}{\partial L_2} = 0 \quad (5.23)$$

$$n(L_1, L_2, t = 0) = n_0(L_1, L_2) \quad (5.24)$$

$$n(L_1 = 0, L_2, t) = 0 \quad (5.25)$$

$$n(L_1, L_2 = 0, t) = 0 \quad (5.26)$$

Here, D_i is the dissolution rate along characteristic dimension L_i and has a negative value. The material balance presented in Equation 5.5 is coupled with Equation 5.23 to ensure preservation of the mass of solute. The functional form chosen is that proposed by Eisenschmidt et al.⁷⁵

$$D_i = -k_{D,i1} \exp\left(-\frac{k_{D,i2}}{T}\right) (1 - S)^{k_{D,i3}} \quad \text{with } S < 1 \quad (5.27)$$

5.2.1.5 Solution of the MPBE

The MPBE is solved by discretizing Equations 5.1 and 5.23 along the internal coordinates using 300 and 100 points for L_1 and L_2 , respectively. The MPBEs for crystallization and dissolution are solved using the finite volume method, with Van Leer flux limiters for improved stability,⁷⁸ while the MPBE for breakage is solved by exploiting the fixed pivot technique developed by Kumar et al.,⁵³ to ensure the preservation of the number of fragments formed and of their mass. Simulations have been performed on a Computer with an Intel(R) Xeon(R) CPU E5-2687W v3 @ 3.10 GHz processor, 20 cores, and 32 GB of RAM.

5.2.2 Process performance indicators

In order to quantify the quality of the products obtained at the end of both simulations and experiments, it is convenient and necessary to define average properties extracted by their particle size and shape distribution, using the cross-moments defined as

$$\mu_{ij}(t) = \int_0^\infty \int_0^\infty n(L_1, L_2, t) L_1^i L_2^j dL_1 dL_2 \quad (5.28)$$

Table 5.1 reports the definition for the average quantities used to quantify the product quality. In particular, the volume-weighted average length $L_{1,V}$ and width $L_{2,V}$ are used to identify the attainable region of the 3-stage process for both simulations and experiments. The number-weighted variances of the distribution, $\sigma_{1,N}$ and $\sigma_{2,N}$, and the number-weighted average sizes, $L_{1,N}$, and width, $L_{2,N}$, can be exploited to further characterize the product quality and to estimate the kinetic parameters appearing in the constitutive equations of the model, as discussed in detail in Section 5.4.1.4.

Average quantities	
Volume weighted $L_{1,V}$:	μ_{22}/μ_{12}
Volume weighted $L_{2,V}$:	μ_{13}/μ_{12}
Number weighted $L_{1,N}$:	μ_{10}/μ_{00}
Number weighted $L_{2,N}$:	μ_{01}/μ_{00}
Number weighted $\sigma_{1,N}$:	$\sqrt{\mu_{20}/\mu_{00} - L_{1,N}^2}$
Number weighted $\sigma_{2,N}$:	$\sqrt{\mu_{02}/\mu_{00} - L_{2,N}^2}$

TABLE 5.1: Performance indicators used in this work.

5.2.3 Parametric analysis

The aim of this work is to develop a strategy to characterize, using a small amount of experiments, the outcome of the 3-stage process when applied to compounds with different properties and kinetics. An in-silico approach is certainly convenient to define such strategy, since it allows tackling this problem with a limited effort in comparison to that required for a comprehensive experimental characterization. Therefore, we have carried out first a sensitivity analysis on the operating conditions, namely the rotor speed θ and the number of cycles n_c , adopting the conditions reported in Table 5.3.

The choice stems from the observation made elsewhere^{34,36} that these two operating parameters have the strongest impact on product properties.

Stage	Parameter	Dimension L ₁	Dimension L ₂
Crystallization	$k_{G,i1}$ [$\mu\text{m s}^{-1}$]	600 - 4800	58
	$k_{G,i2}$ [K]	2400	2400
	$k_{G,i3}$ [-]	3.7	2.5
	$k_{\text{Ho},1}$ [$\# \text{kg}^{-3} \text{s}^{-1}$]	1.3×10^{24}	
	$k_{\text{Ho},2}$ [-]	163	
	$k_{\text{He},1}$ [$\# \text{kg}^{-3} \text{s}^{-1}$]	1.4×10^5	
	$k_{\text{He},2}$ [-]	10	
	$k_{\text{S},1}$ [-]	2.5×10^{19}	
	$k_{\text{S},2}$ [-]	0.6	
	$k_{\text{S},3}$ [-]	0.75	
Milling	$k_{\text{S},4}$ [-]	2	
	$k_{\text{M},i1}$ [s^{-1}]	16.06	16.06
	$k_{\text{M},i2}$ [-]	1.907	1.964
	$k_{\text{M},i3}$ [μm]	30	30
Dissolution	$k_{\text{M},i4}$ [-]	$\sqrt{3}$	$\sqrt{3}$
	$k_{\text{D},i1}$ [$\mu\text{m s}^{-1}$]	$0.205 - 1.636 \times 10^6$	0.272×10^6
	$k_{\text{D},i2}$ [K]	3572	3223
	$k_{\text{D},i3}$ [-]	1	1

TABLE 5.2: Model parameters adopted in the simulations

Process		Stages	
Condition	Set point	Condition	Set point
Initial temp. $T_{0,C1}$	50 °C	Crystallization	
Final temp. $T_{f,Cn}$	25 °C	Temp. drop ΔT_C	$(T_{0,C1} - T_{f,Cn}) / n_C$
Seeds mass m_0	1 g kg _w ⁻¹	Cooling rate γ_C	6 °C h ⁻¹
Seeds	fine powder	Milling	
N° cycles n_C	2-6	Residence time τ	5 s
		Rotor speed θ [rpm]	3,000-26,000
		Dissolution	
		Fraction of mass dissolved m_D	40%
		Heating rate γ_D	6 °C h ⁻¹

TABLE 5-3: Operating conditions in the simulations

The range of operating conditions investigated in this work is the one that can be effectively applied when the experimental setup described in Section 5.3.1 is used. This is certainly of interest and improves the information provided by the model, as it allows to acquire a more precise estimation of the outcome of the 3-stage process. The sensitivity analysis has been subsequently complemented with a parametric analysis on some of the parameters appearing in the constitutive equations of the model, by varying them in physically-sound intervals. By doing so, we aim at simulating and characterizing the outcome of the 3-stage process, under a broad range of operating conditions, when applied to different compounds exhibiting different intrinsic features. In particular, the analysis focused on the growth and dissolution rates for both characteristic dimensions, as the energy input provided by the grinding device and the mechanical properties of typical active pharmaceutical ingredients are such that it is not possible to observe a significant variation in the average sizes of the ground crystals when considering different such substances.¹¹⁷ The effect of different growth and dissolution rates has been simulated by varying the pre-exponential factors $k_{G,11}$ and $k_{D,11}$, in the range reported in Table 5.2. This choice stems from the observation that varying all the remaining parameters appearing in the growth and dissolution rates shown in Equations 5.8 and 5.27 would lead to similar conclusions. Moreover, given the linear dependence of the growth and dissolution rates on the selected parameters, it is possible to easily relate the trends observed with the change in the corresponding kinetics. It is worth noting that the absolute value of the growth or dissolution kinetics is however of limited interest in the context of studies where crystal shape is the focus, since it is the ratio of the growth and dissolution rates of the specific facets that determines the morphology of the crystals and not their absolute values.⁶⁷ The results obtained are therefore rationalized to quickly identify trends characteristic to specific groups of compounds based on common features (i.e. ratio of the dissolution rates, ratio of the growth rates, etc.) and are subsequently used to design and guide the experimental activity required to characterize the 3-stage process when applied to new systems.

5.2.3.1 *Effect of varying the operating conditions*

The third panel on the second row of Figure 5.1 shows, in the L_1L_2 -plane, all the possible simulated outcomes of the 3-stage process (pink circles encased by solid pink lines), adopting the simulation conditions reported in Table 5.3 and when $k_{G,11} = 600 \mu\text{m s}^{-1}$ and $k_{D,11} = 0.818 \times 10^6 \mu\text{m s}^{-1}$.

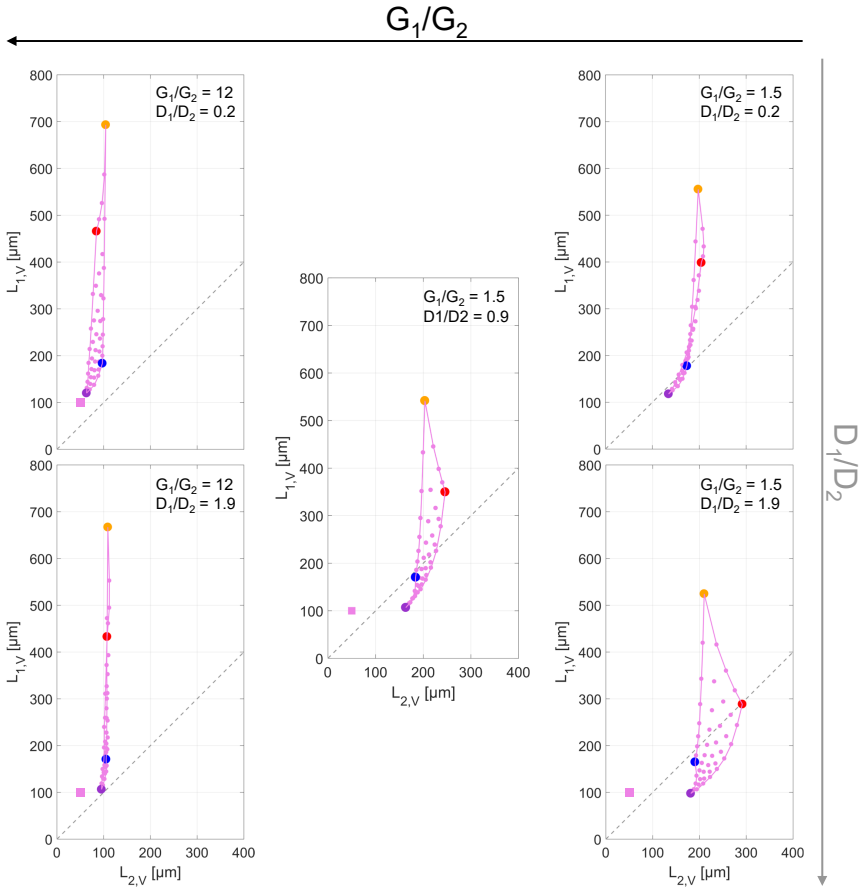


FIGURE 5.1: Results of the sensitivity and parametric analyses performed by varying first the rotor speed θ and the number of cycles n_C (see Table 5.3) and subsequently the growth and dissolution kinetics to reproduce the effect of different compound properties on the achievable region of the 3-stage process. The pink dots represent all the possible outcomes obtained adopting the kinetic parameters reported in Table 5.2 and the conditions shown in Table 5.3. The solid pink line enclosing all the possible outcome of the 3-stage process represents the so called attainable region. The four experiments, indicated by the orange, red, blue, and purple markers, corresponding to the four tests constituting the smart approach for process characterization.

It is readily observed that all the average sizes obtained at the end of the process belong to a curved quadrilateral region, whose vertices are the four colored points; we call this region the attainable region (by the 3-stage process) for a given substance and the selected seeds characteristics. Such points correspond to the outcome of the process when the combination of the minimum and maximum level chosen for the rotor speed θ (3,000 and 26,000 rpm) and the number of cycles n_c (2 and 6) are applied. Therefore, a possible experimental screening procedure to assess the feasibility of the 3-stage process for a specific new substance consists in performing these four experiments, corresponding to a two-factors factorial design, and to use the sizes of their products to define an approximated attainable region. This has the advantage of being a model-free strategy, that does not require a comprehensive characterization of the system, which is known to be extremely time demanding.

5.2.3.2 *Effect of varying the system kinetics*

However, it is necessary to verify the applicability of this method also when compounds with different properties are used. Therefore, a parametric analysis has been performed investigating the effect of different growth and dissolution kinetics. Its results are reported in the other panels of Figure 5.1. Here it is possible to observe that very distinct attainable regions can be obtained for different simulated compounds, ranging from a situation where the 3-stage process actually worsens the particle size and shape when more cycles are applied (upper left corner) to a case where it greatly improves the crystal morphology leading to a wide variety of different outputs (lower right corner). It is worth noting that in all cases the outcome of the factorial design experiments can be used to delimit and define the attainable region, thus confirming the suitability and robustness of the characterization strategy proposed.

In order to get a deeper understanding of the connection between compound kinetics and process outcome, it is convenient to observe how the relative position of the average sizes of the four identified experiments and their absolute position in the L_1L_2 -plane changes when different kinetics are applied. To this aim, panel (a) of Figure 5.2 can be used to visualize these effects. The black and gray arrows show the results of the parametric analysis when either the growth or the dissolution kinetics only are changed, while the shaded area shows the results obtained when all the possible combinations of growth and dissolution rates are explored. The effect of different growth rate ratios is generally more significant than that

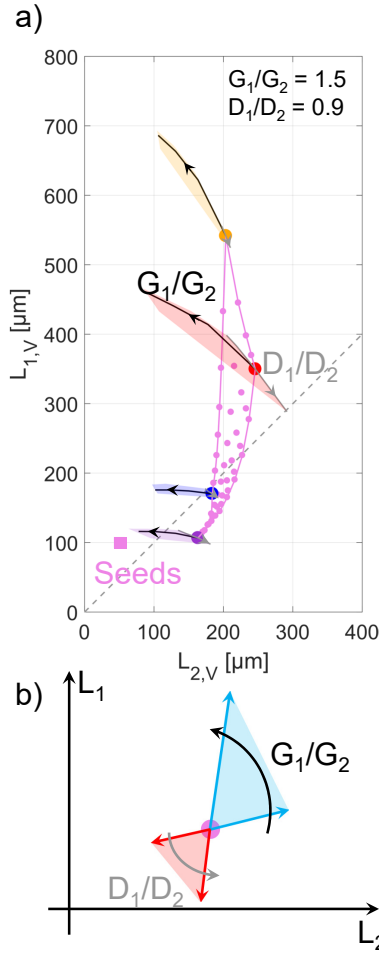


FIGURE 5.2: In panel (a), the effect of different growth and dissolution kinetics on the four experiments used for robust and efficient process characterization is shown. The conceptualization of the phenomena leading to the different types of attainable regions are shown in panel (b). Here, for different growth and dissolution rates, the evolution of the sizes of an exemplary particle during growth and dissolution is shown.

of the dissolution rates. Possible reasons for this might be that the growth stages span larger temperature intervals for cooling in comparison to those adopted for dissolution through heating, and that in the overall process there are less dissolution steps than growth steps. Furthermore, the effect of different kinetic rates appears more significant when more cycles are carried out, which is to be expected since overall more crystallization and dissolution stages are performed. The effect of a change in growth and dissolution rates reduces when high milling intensities are applied, due to the milling becoming the controlling stage in manipulating the PSSD. These effects are also visible when considering the whole attainable region. The reason for the different types of attainable region obtained lies in how the mass is removed and reprecipitated on the crystals throughout the cycles, as high dissolution rates and low growth rates along L_1 help in achieving a better morphology by reducing the characteristic length and by favoring the growth along the width, while the opposite situation occurs for high G_1/G_2 ratios and low D_1/D_2 ratios. A conceptualization of these effects is illustrated in Figure 5.2 (b), where the blue arrows and the comprised region represent an exemplary evolution of the particle sizes for different G_1/G_2 (black arrow) during cooling, while the red arrows and the region between them represent the evolution of the sizes for different D_1/D_2 (gray arrow) ratios during the dissolution stage.

5.2.3.3 *Effect of varying the seeds characteristics*

To verify how the type of attainable region obtained at the end of the 3-stage process depends on the characteristics of the seeds, we extended the parametric analysis by performing simulations where the mass of seeds and their PSSD are varied. Table 5.4 reports the characteristics of the different seeds used at the beginning of each simulation, while Figure 5.3 shows the attainable regions for the three cases considered. As it is readily observed, the shape of the region obtained for the three cases is the same, with the characteristics of the seeds having an effect on the final average sizes only. This observation is of great relevance, as it demonstrates that the type of attainable region does indeed depend on the intrinsic properties of the compound to which the 3-stage process is applied only and not on the PSSD or on the amount of the seeds used.

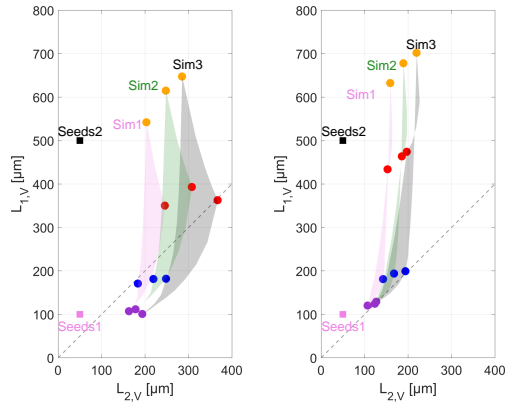


FIGURE 5.3: Results of the analysis performed to investigate the effect of different seed populations and mass thereof on the attainable region of the 3-stage process for two sets of kinetic parameters.

Simulation	Seeds	Seeds properties	Seeds mass m_0
Sim1	Seeds 1	Gaussian $\mu_{L_1} = 100 \mu\text{m}$	1 g kg_w^{-1}
Sim2	Seeds 1	and $\mu_{L_2} = 50 \mu\text{m}$	0.25 g kg_w^{-1}
Sim3	Seeds 2	Gaussian $\mu_{L_1} = 500 \mu\text{m}$	1 g kg_w^{-1}
		and $\mu_{L_2} = 50 \mu\text{m}$	

TABLE 5.4: Seeds used in simulations

5.2.3.4 Factorial design

The results of the parametric analysis are very important, as they have allowed us to identify a smart, robust, and effective experimental screening procedure required to investigate the feasibility and potential of the 3-stage process with neither a thorough characterization of compound specific properties nor system-specific mathematical modeling. This procedure consists in performing four experiments, under operating conditions defined by combining the minimum and maximum applicable milling intensity and number of cycles, and defining the attainable region as the portion of the L_1L_2 -plane enclosed by the average sizes of the corresponding products. Furthermore, the simulations showed that the type of attainable region obtained depends only on the ratio of growth rates G_1/G_2 and dissolution rates D_1/D_2 typical of the compound used.

A few remarks are necessary. The first concerns the quality of the characterization of the process outcome obtained with the factorial design approach. As shown in previous publications,^{34,36} the dependence of the final size and shape of the crystals on the operating conditions is strongly non-linear. Nevertheless, the approximated achievable region, obtained with the approach proposed in this work, still represents a good indication of the process outcome and can be used as a guide throughout the process design stage, where decisions concerning the operating conditions are made.

The second remark concerns the improvement in product properties achieved when the compound exhibits high G_1/G_2 and low D_1/D_2 ratios. The reduced variability in process outcome obtained shows that the final size and morphology of the crystals cannot be significantly improved by increasing the number of cycles performed. Nevertheless, the 3-stage process, due to the repeated milling and dissolution stages, allows to obtain crystals that are more compact than those obtained by simple cooling, as well as a final powder with a reduced presence of fines in comparison to that obtained by simple milling.

The strategy for process characterization developed in this chapter will be assessed with a dedicated experimental campaign using two different compounds, namely β L-Glutamic acid and γ D-Mannitol. For the latter, however, it is necessary to estimate the specific growth rates in order to relate its properties to the type of attainable region obtained. To this aim, the fourteen cooling stages performed belonging to the four factorial experiments can be used. This is of particular interest, given that a deeper insight and characterization of the system can be obtained without performing any other experiments. Therefore, a preliminary in-silico study has been carried out to assess the possibility of using the information of the fourteen cooling stages to estimate growth kinetics.

5.2.4 *Fitting of the kinetic parameters*

In this paper, we estimate the growth kinetics of γ D-Mannitol exploiting the information available from the four experiments performed according to the factorial design approach. The estimation is performed by minimizing the objective function defined as

$$F(\mathbf{p}) = \frac{N_E}{2} \sum_{i=1}^{N_O} \ln \sum_{j=1}^{N_E} w_{ij} \left(\frac{y_{ij} - \hat{y}_{ij}(\mathbf{p})}{y_{ij}} \right)^2 \quad (5.29)$$

Where \mathbf{p} represents the set of growth kinetic parameters to be estimated, N_E is the number of experimental measurements, N_O is the number of fitted outputs (average properties of the measured PSSD), y_i represents any average property of the measured particle size and shape distribution for the i -th experiment that needs to be fitted, $\hat{y}_i(\mathbf{p})$ is the corresponding model estimate based on the set of parameters \mathbf{p} , and w_{ij} is used to weight the contribution of each relative error to the objective function. To identify the minimum of the function $F(\mathbf{p})$, the genetic algorithm provided by the Matlab optimization toolbox is used. The algorithm is seeded using 50 % of the individuals randomly generated using latin hypercube sampling and 50 % from the last population of the previous run. The population size chosen is 60, with a crossover fraction of 0.70.

While on the one hand fitting the whole particle size and shape distribution would be of great interest, on the other hand this would lead to a very high computational burden. Therefore, in this work we aim at fitting the number-weighted average sizes and variances reported in Table 5.1, which allow identifying uniquely the whole distribution of crystals with a reduced simulation effort.

5.2.4.1 Confidence intervals estimation

Along with the kinetic parameters, we also estimate the corresponding confidence intervals by means of the Jacobian analysis.

The diagonal element S_{ii} of the error covariance matrix can be calculated as

$$S_{ii} \approx \sigma_{E,i}^2 = \frac{1}{N_E} \sum_{j=1}^{N_E} (y_j - \hat{y}_j(\mathbf{p}^*))^2 \quad (5.30)$$

By linearizing the model and assuming normally distributed errors, the positive semidefinite covariance matrix \mathbf{V} can be estimated using the corresponding Jacobian matrix as

$$\mathbf{V} \approx (\mathbf{J}^T \mathbf{S} \mathbf{J})^{-1} \quad (5.31)$$

This matrix can be used to determine the hyperellipsoid defined at the confidence level α corresponding to the approximate confidence intervals for the estimated parameter j .

$$C_j = t_{1-\alpha/2}^{N-k} \sqrt{V_{jj}} \quad (5.32)$$

In Equation 5.32, $t_{1-\alpha/2}^{N-k}$ corresponds to the value of the t -statistics with $N - k$ degrees of freedom at the designed confidence level α . The estimated confidence intervals are certainly affected by the uncertainty introduced with the linearization hypothesis, but they provide nevertheless the information required to evaluate the quality of the fitting.

5.2.5 Estimation of growth kinetics from in-silico data

In order to assess the possibility of estimating the growth rate parameters using the information associated to the fourteen cooling stages performed at different operating conditions while carrying out the complete factorial design protocol, the in-silico data generated by the model in the course of the corresponding simulations can be used. In particular, the time-resolved number-weighted average L_1 and L_2 are used and fitted to estimate the value of the kinetic parameters appearing in Equation 5.8 for both crystal dimensions. In order to reproduce the effect of the experimental error and measurement uncertainties on the measured sizes, white Gaussian noise is added to the simulated data, using the in-built Matlab function *awgn*, thus generating in-silico a set of experimental data.

Panel (a) of Figure 5.4 shows the in-silico generated experimental data (red boxes), while the results of the fitting are reported as a blue solid line. For the sake of clarity and brevity, only the results of 3 out of the 14 available cooling stages are shown. The quality of the fitting is satisfactory, with a good quantitative agreement (average absolute error of 10 μm) for both dimensions) between the two sets of data. Panel (b) shows, in the concentration vs. temperature plane, the region explored by the different simulated stages (red area) and the solubility curve (black line): the range of validity of the fitting covers a broad range of temperatures and concentrations. It is worth noting that the region partially lies below the solubility line, which corresponds to the conditions of the solution at the beginning of the cooling stages; this is due to the final conditions of the simulated dissolution stage, as the simulations are stopped at a close-to-equilibrium concentration. Finally, even if for some of the cooling stages the initial and final temperatures are the same, the different particle ensembles suspended, both in terms of number of crystals and sizes of the particles, lead to a different evolution of the concentration throughout the stages, thus making these stages actually different and allowing to effectively exploit all the cooling steps for the estimation of the kinetics.

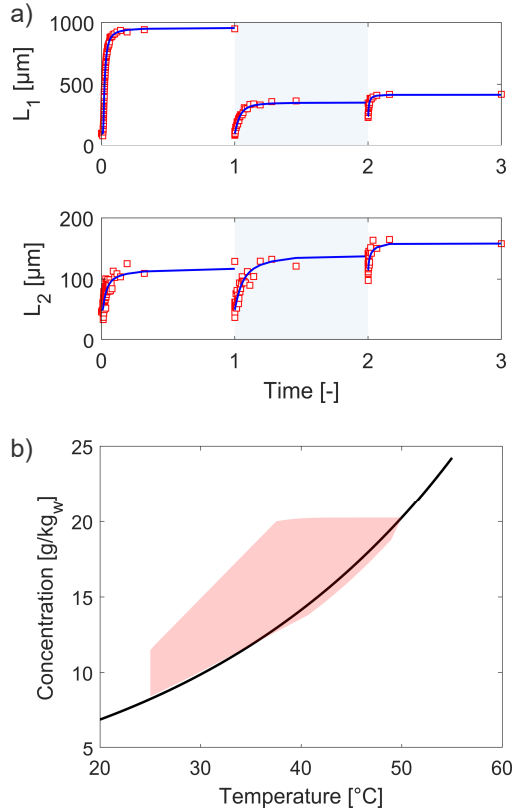


FIGURE 5.4: Results of the in-silico fitting performed to assess the possibility of estimating growth kinetics using the data available when the factorial experiments are performed. In (a) the fitted average sizes are shown, while panel (b) shows the range of concentration and temperatures over which the fitting is performed.

5.3 MATERIALS

The compounds used in this work are D-Mannitol (Sigma-Aldrich, $\geq 98\%$, Switzerland) and L-Glutamic acid, produced by pH-shift precipitation from L-Glutamic acid monosodium monohydrate (Sigma Aldrich $\geq 98\%$, Switzerland) and hydrochloric acid (Fluka, Buchs, 37-38%).

As highlighted by Cornel et al.,¹¹⁸ D-Mannitol exhibits three different polymorphs, whose solubilities in water are reported in panel (a) of Figure 5.5. In this work we focus on the thermodynamically stable polymorph γ , exhibiting a needle-like morphology. However, to reduce the extremely large solubility of D-Mannitol in the solvent and to avoid the formation of bacteria colonies in suspension, the solvent used in the experimental campaign is a mixture of water (Millipore Milli-Q, Zug, Switzerland) and propan-2-ol (Reagent grade, VWR, Germany) which is an antisolvent for D-Mannitol. Therefore, the solubility of γ D-Mannitol is measured according to the experimental procedure described in Section 5.3.2. The seeds used for the factorial experiments described in Section 5.3.3 consist of the fine powder delivered as a raw chemical without further treatment. The corresponding particle size and shape distribution is reported on the right-hand side of Figure 5.6.

L-Glutamic acid has two polymorphic forms, namely the metastable α form and the thermodynamically stable β form, which are monotropically related.⁵⁴ The corresponding solubilities are reported in panel (b) of Figure 5.5. The seeds of β L-Glutamic acid used throughout the experimental campaign were obtained by polymorphic transformation from the α form via pH-shift, and their particle size and shape distribution is shown in the left-hand side of Figure 5.6.

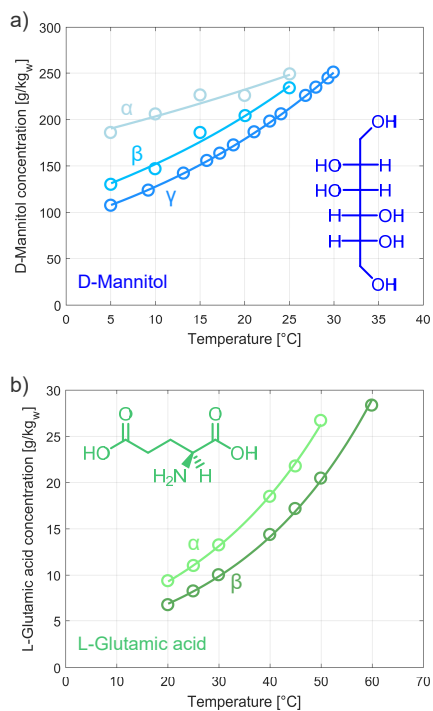


FIGURE 5.5: Solubility of the model compounds and their polymorphs. Panel (a) shows the solubility in water of the three polymorphs of D-Mannitol, the metastable α and β , and the stable γ , as reported by Cornel et al.¹¹⁸ In panel (b) the solubility of α and β L-Glutamic acid from Scholl et al.⁵⁴ are plotted.

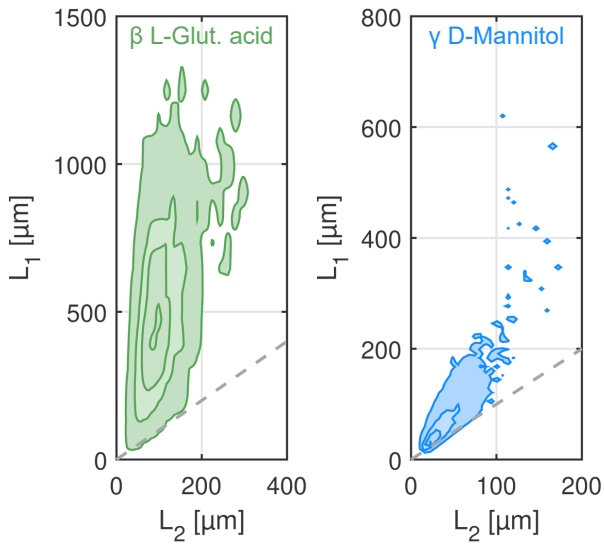


FIGURE 5.6: Volume-weighted average particle size and shape distributions of the seeds of γ D-Mannitol (left) and β L-Glutamic acid (right) used for the factorial experiments.

5.3.1 Experimental setup

In Figure 5.7, a sketch of the laboratory setup is shown. The experimental rig consists of two crystallizers, a continuous rotor-stator wet mill (IKA MagicLab, Module MK), and a peristaltic pump (Ismatec BVP). In order to keep the temperature of the suspension constant during milling, the grinding chamber is jacketed and connected to a thermostat. Moreover, each crystallizer is equipped with a dedicated thermostat for the precise control of the suspension temperature during crystallization and dissolution and with a dedicated ATR-FTIR spectrometer (ReactIR 45m, Mettler Toledo, Switzerland), used to monitor the concentration of D-Mannitol in the liquid phase. An FBRM G400 (Mettler Toledo, Switzerland) is used to monitor possible nucleation and attrition events. This device is used only to detect the formation of fine particles, since the extraction of quantitative information on the size and shape of non-equant particles from FBRM measurements is known to be troublesome.

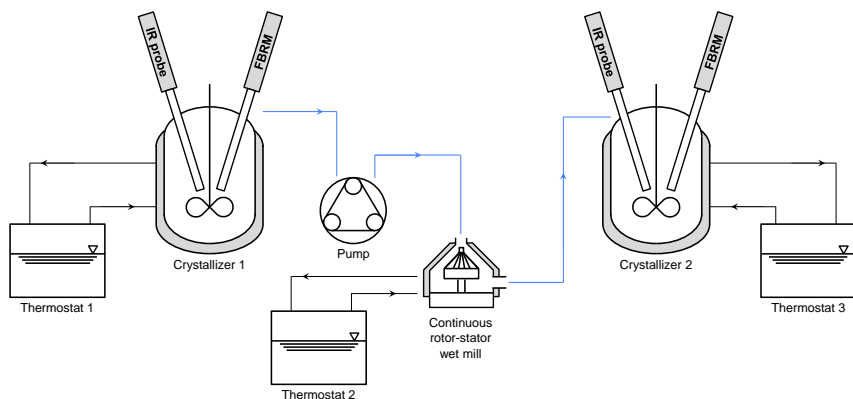


FIGURE 5.7: Scheme of the laboratory setup.

5.3.2 Solubility of γ D-Mannitol

In this work, the solubility of γ D-Mannitol in a 10/90 wt% mixture of propan-2-ol and water is measured in the temperature range 3–30 °C using both a gravimetric method and an ATR-FTIR-based approach.

To perform the gravimetric analysis, a suspension is prepared by adding to 500 g of the propan-2-ol/water mixture, kept at the target temperature

T , an excess of solids. The suspension is then kept at T under stirred conditions for 24 h. Three samples of the liquid phase are then taken and placed on three Petri dishes, which are subsequently left in a ventilated oven at 25 °C for 24 hours. The weights of the empty, full, and dried Petri dishes are recorded, thus allowing to evaluate the solubility.

The solubility is also assessed with chemometrics measurements. To correctly capture both the effect of temperature and concentration on the infrared signal, a first set of calibration experiments has to be performed to fit the concentration to the characteristic peaks. Here, 2 kg of the propan-2-ol/water mixture are prepared at temperature T_0 in a stirred jacketed crystallizer, equipped with an FBRM probe to detect possible nucleation events. γ D-Mannitol is added to produce an undersaturated solution (saturated at T_S), which is then cooled down to the final temperature T_F at a rate of 5 °C h⁻¹.

Exp ID	m_W [g]	m_P [g]	m_M [g]	T_0 [°C]	T_F [°C]	T_S [°C]
Blank	1799.9	200.1	0	30	3	–
Exp1	1800.6	200.9	365.18	40	20	30
Exp2	1799.9	200.7	258.60	30	10	20
Exp3	1800.4	200.9	154.64	15	3	5
Exp4	1799.7	200.2	144.59	15	3	3
Val1	1800.5	200.5	233.30	5	15	n/a
Val2	1799.9	200.0	329.30	15	25	n/a
Val3	1800.2	200.3	391.42	20	30	n/a
Val4	1800.3	201.5	395.04	25	30	n/a

TABLE 5.5: List of the ATR-FTIR calibration and solubility measurements.

The IR spectra are collected until either the final temperature is reached or nucleation is detected. The results of the calibration experiments are used to train a model based on partial least squares regression (PLS), which correlates the intensity of the baseline-corrected spectra to the concentration of the solution characteristic of each experiment at different temperatures. To this aim we used the Matlab function *plsregress* with 10-fold cross vali-

dation and four latent variables. Figure 5.8 shows the set of experiments performed under the conditions reported in Table 5.5 and according to the procedure described above.

The experiments have been repeated twice and allow calibrating robustly the ATR-FTIR over a broad range of concentrations and temperatures. In the upper part of panel (b), the raw spectra collected during the experiments are reported along with that of the solvent mixture (blank experiment). In order to correlate the peak intensity with the concentration of γ D-Mannitol in solution, a single-point baseline correction is applied, using as a reference the intensity at 1127 cm^{-1} wavenumber. The choice is motivated by the fact that the spectrum of propan-2-ol exhibits a maximum at that wavenumber, and its concentration in the solvent mixture remains constant. Hence, its absorbance at a given temperature should be equal at any given solute concentration. This assumption is confirmed by visual inspection of the spectra collected at various conditions, and the choice of the baseline results in consistent spectra among the repetitions of the same experiments. The PLS regression is performed in the wavenumber range 1127 to 999 cm^{-1} , where the characteristic peaks of γ D-Mannitol show the maximum variability upon changes in concentration and are least affected by those of the solvent. The results of the baseline correction are reported in the lower plot of panel (b).

The solubility is estimated by performing four dedicated experiments, where 2 kg of the propan-2-ol/water mixture are prepared at four different initial temperatures. An excess of γ D-Mannitol is added and the system is kept under constant conditions for two hours. The suspension is then heated at a rate of $2\text{ }^{\circ}\text{C h}^{-1}$ until the final temperature is reached. The results of the solubility measurements, carried out under the conditions in Table 5.5, are shown in panel (c) with purple markers. Here, a comparison with the data acquired with gravimetric measurements (represented by the black triangles) is carried out. The good agreement between the results obtained with different techniques assesses the possibility of measuring accurately the solute concentration throughout the experimental campaign.

To check the possible influence of the different solvent on the solid form, an X-ray powder diffraction measurement (XRPD) is performed on the crystals recovered at the end of the experiments. Panel (d) of Figure 5.8 shows the results of the XRPD measurement as obtained by Cornel et al.¹¹⁸ in water and those obtained in this work for γ D-Mannitol in the water/propan-2-ol mixture. Being the two patterns identical, we conclude

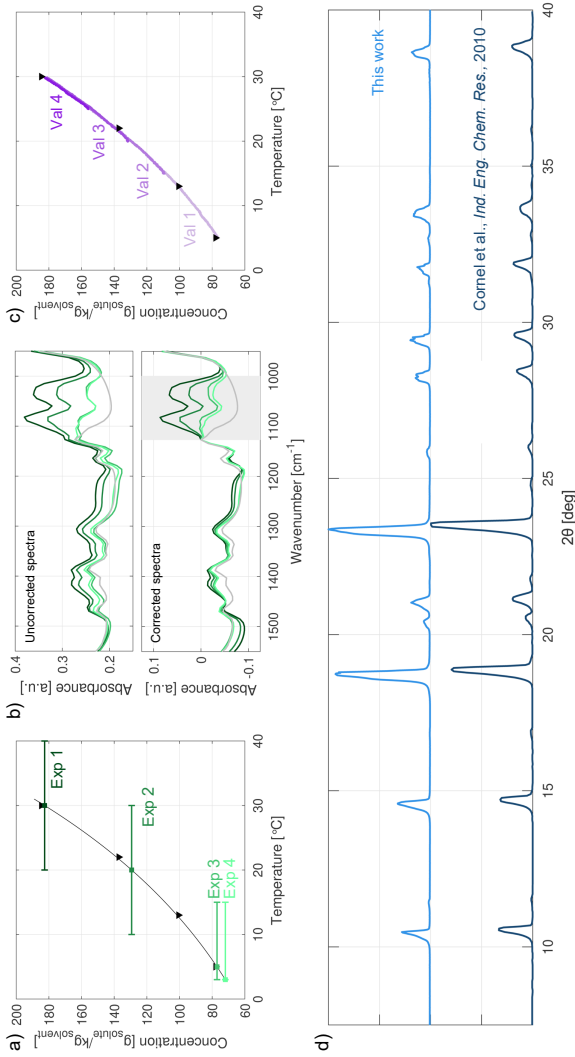


FIGURE 5-8: (a) Range of concentrations and temperatures explored with the calibration experiments. The black triangles correspond to the gravimetric data of solubility which were fitted with an exponential function (black line). (b) In the upper plot, the raw spectra collected for each calibration experiment at saturated conditions according to the gravimetric measurements are reported. The spectrum of the blank experiment in gray was collected at 20 °C. In the lower plot, the same spectra, after applying the baseline correction, are shown and the range of wavenumbers used by the PLS algorithm is highlighted. (c) Concentration profiles of the solubility experiment as estimated from ATR-FTIR measurements compared with the gravimetric data. (d) Comparison between the XRPD pattern obtained by Cornel, Kidambi & Mazzotti [118] for γ -D-Mannitol and that obtained in this work.

that the change of solvent did not impact the solid form produced at the end of the crystallization process.

5.3.3 3-stage process experimental protocol and factorial design

A saturated solution of the specific compound in the corresponding solvent is prepared at the initial temperature $T_{0,C1}$. The required amount of seeds m_0 is added and the system is cooled to the final temperature of the first cooling stage $T_{f,C1}$ at the rate γ_C . The system is kept at constant temperature until equilibrium is approached. The suspension of crystals is pumped at 0.98 L min^{-1} through the continuous rotor-stator wet mill, operated at the desired rotor speed θ . The outcome is collected in a second crystallizer, where it is heated to the temperature $T_{f,H1}$, chosen to ensure that, in the proximity of equilibrium, the fraction of suspended mass m_D will be dissolved. The dissolution step is necessary to eliminate most of the fine particles formed during the milling stage, and the value of m_D has to be carefully chosen so as to accomplish the task without reducing the efficiency of the overall process. The stages are repeated n number of times until the final temperature $T_{f,Cn}$ is reached. Then the crystals are collected, filtered, and washed with pure propan-2-ol to promote displacement of the entrained solution, thus avoiding its crystallization during drying. Finally, the washed filter cake is placed in a ventilated oven at 65°C for 24 h.

5.3.4 PSSD measurement setup and protocol

The PSSD of the products is measured by using the μ -DISCO, a stereoscopic imaging device, described by Rajagopalan et al.⁵¹ It consists of two cameras, equipped with telecentric lenses, arranged in an orthogonal configuration, thus allowing for the reconstruction of the particle shape starting from two orthogonally projected images of the same crystal. Pictures of the particle suspension, flowing in a quartz cell engineered to ensure lowest optical distortion, are collected through bursts with a frame rate of 35 fps. For each measurement, 10 bursts of 800 images each are launched, thus allowing to reconstruct the size and shape of approximately 30,000 particles in a time interval of 15 minutes. Based on the reconstructed geometrical properties, the particles are automatically classified in 5 classes, namely spheres, cuboids, needles, platelets, and non-convex polytopes. In this work, we only consider the needles and cuboids classes, as we believe, based on visual inspection under the optical microscope, that other crystal

shapes occasionally detected are not representative of the crystal population. Because of the high suspension density, reaching 7 wt% in the case of γ D-Mannitol, the measurements are performed off-line on a suspension of crystals in antisolvent.

5.4 RESULTS AND DISCUSSION

5.4.1 *Factorial design for the 3-stage process*

In this section we aim at assessing the strategy described above by applying it experimentally to two different compounds, namely β L-Glutamic acid and γ D-Mannitol, both crystallized from specific aqueous solutions. In particular, for each of them, the four factorial experiments are carried out to identify the corresponding attainable region. To relate the type of attainable region obtained for the two compounds to their specific properties, an estimation of the growth kinetics for γ D-Mannitol is performed and the estimated kinetics are compared to those already available for β L-Glutamic acid. Based on these results and on the process simulations, a general system-dependent strategy to identify heuristic optimal conditions is proposed.

5.4.1.1 *Case study 1: β L-Glutamic acid*

Given that the effectiveness of the 3-stage process in modifying the size and shape of β L-Glutamic acid crystals has already been evaluated both experimentally and in-silico and thoroughly discussed elsewhere,^{34,36} we report here results for this compound as a reference case, aiming at highlighting how the well-known properties of this system can be used to interpret the outcome of the process based on the general trends observed through the simulations presented above.

The 3-stage process is applied according to the operating conditions in Tables 5.6 and 5.7, and the resulting volume-weighted average characteristic dimensions of the final crystal population are shown for each of the factorial experiments together with the full PSSDs in the left-hand side of Figure 5.9. One can readily observe that the number of cycles significantly affects the width L_2 of the crystals, thus leading to a wide attainable region. This is a case where the process we consider is most effective in navigating the space plane by changing the relative dimensions of the crystals, and both the milling intensity and the number of cycles have an evident impact on the final crystal shape.

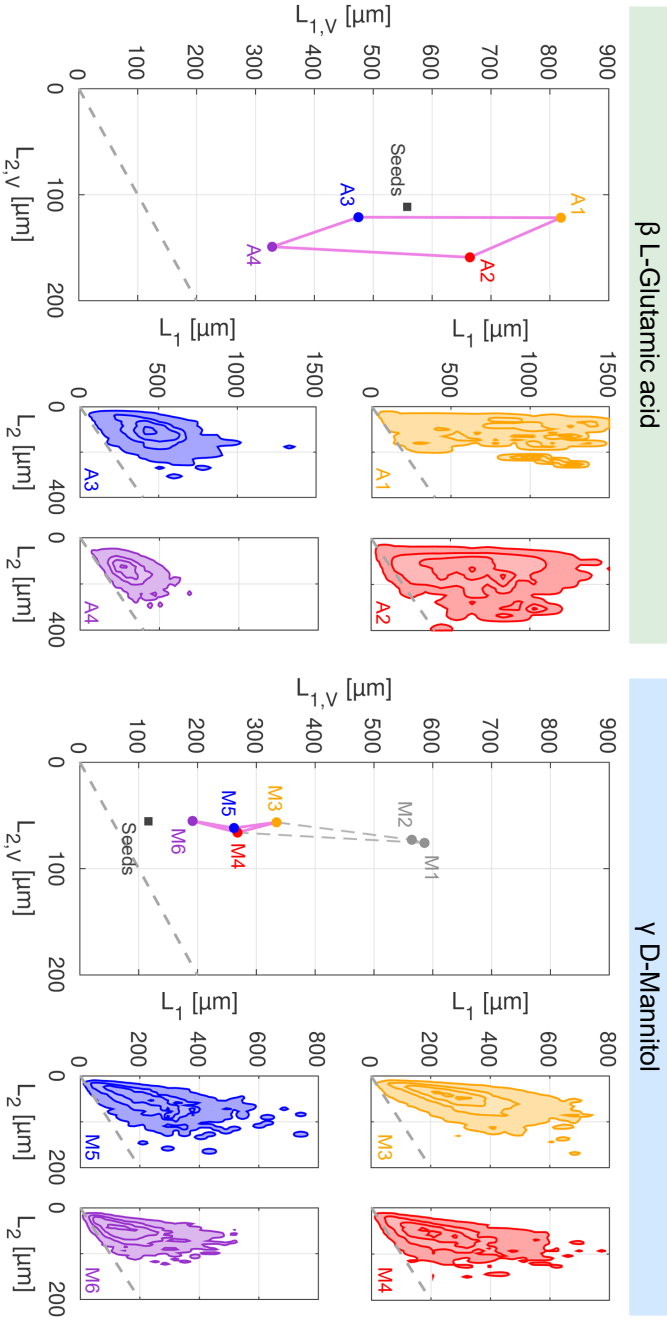


FIGURE 5-9: Results of the factorial design applied to β -L-Glutamic acid and γ -D-Mannitol. For each case, on the left, the volume-weighted average sizes of the products as measured by the μ -D|SCO are shown and the enclosed attainable region is defined by the fuchsia line. The PSSDs for the products of every factorial experiment are reported on the right-hand side of the corresponding plots.

With reference to the simulations illustrated in Figure 5.1, the behavior of β L-Glutamic acid is similar to that corresponding to the three cases at bottom right corner of the figure, i.e. for small values of the ratio G_1/G_2 when the ratio D_1/D_2 is large or intermediate, and for large values of the ratio D_1/D_2 when the ratio G_1/G_2 is small or intermediate.

5.4.1.2 Case study 2: γ D-Mannitol

The results of the six experiments performed according to the operating conditions reported in Tables 5.6 and 5.7 are shown in the right-hand side of Figure 5.9; for each experiment the volume-weighted average length and width of the final population of crystals are plotted along the full PSSDs.

Inspection under the optical microscope of the crystals obtained in experiments M1 and M2, performed at 5,000 rpm, showed the presence of crystals exceeding the millimeter in length together with a considerable amount of fines. This condition is not optimal for sizing with the μ -DISCO, because due to optical constraints the number of larger crystals would likely be underestimated, with a strong bias in the volume-based average $L_{1,v}$ towards fines. For this reason, we have chosen to include these experiments for the characterization of the attainable region, but we have decided not to exploit their information for the estimation of the growth kinetics.

One can observe that in all the experiments considered the process does not lead to a significant variation in the width of the crystals L_2 . With reference to the simulations illustrated in Figure 5.1, the behavior of γ D-Mannitol is similar to that corresponding to the five systems along the diagonal of the G_1/G_2 - D_1/D_2 plane in the figure; this corresponds to where the ratios G_1/G_2 and D_1/D_2 are simultaneously small, intermediate, or large.

5.4.1.3 Discussion

In the case of β L-Glutamic acid the growth and dissolution rates of the different facets is known from the literature; thus the ratio G_1/G_2 can be calculated to be about 4,⁷⁷ whereas the ratio D_1/D_2 is about 12.¹¹⁹ This puts β L-Glutamic acid in the bottom right corner of Figure 5.1, corresponding to systems for which the 3-stage process allows tuning the PSSD by varying the operating conditions. The experimental results presented in Section 5.4.1.1 and illustrated in the left-hand side of Figure 5.9 are perfectly consistent with the prediction from the values of the ratios G_1/G_2 and D_1/D_2 .

Condition	LGA	DM
Process		
Initial temp. $T_{0,C1}$ [°C]	50	25
Final temp. $T_{f,Cn}$ [°C]	25	5
Seeds mass m_0 [g kg _{solv} ⁻¹]	0.1	7.8
N° cycles n_C	varying	
Crystallization		
Temp. drop ΔT_C	$(T_{0,C1} - T_{f,Cn}) / n_C$	
Cooling rate γ_C [°C h ⁻¹]	6	2
Milling		
Residence time τ [s]	5	
Rotor speed θ [rpm]	varying	
Dissolution		
Fraction of mass dissolved m_D	40%	20%
Heating rate γ_D [°C h ⁻¹]	6	2

TABLE 5.6: Operating conditions of the factorial design for β L-Glutamic acid (LGA) and γ D-Mannitol (DM).

	β L-Glutamic acid		γ D-Mannitol		
	θ [rpm]	n_C	θ [rpm]	n_C	
A1	3,000	2	M1	5,000	2
A2	3,000	6	M2	5,000	5
A3	14,000	2	M3	15,000	2
A4	14,000	6	M4	15,000	5
			M5	25,000	2
			M6	25,000	5

TABLE 5.7: Rotor speed and number of cycles of each experiment of the factorial design for the model compounds.

Such ratios are in contrast not known for γ D-Mannitol, for which we have however the outcome of the experiments carried out according to the factorial design (see Section 5.4.1.2 and the right-hand side of Figure 5.9). Such experiments point at a system where both ratios G_1/G_2 and D_1/D_2 are small, or intermediate, or large (in relative terms). In order to confirm this system's property, we should either carry out a full-fledged characterization of growth and dissolution kinetics, i.e. a task beyond the scope of this work, or alternatively use the available cooling steps performed during the factorial design experiments in order to obtain a best estimate of the growth kinetics (as discussed in Sections 5.2.4 and 5.2.5). The latter approach will be pursued in the following.

5.4.1.4 Empirical estimation of γ D-Mannitol growth kinetics

From the experiments reported in Section 5.4.1.2, there are nine cooling stages that can be used for the empirical characterization of the γ D-Mannitol growth rates. For each cooling stage we have measured the solute concentration continuously and the PSSD of the starting and of the final ensemble of crystals. These data are shown in the two panels of Figure 5.10, where the data of the nine cooling stages are concatenated and plotted as function of a rescaled time (horizontal axis), with the actual duration of each step is reported in the upper panel. Both panels show the measured solute concentration in grams of solute per kilogram of solvent (light blue profiles, left vertical axis); the final number-weighted average length of the crystals, $L_{1,N}$, and variance along the L_1 direction, $\sigma_{1,N}$, are also shown in the upper and in the lower panel, respectively (pink circles, referring to the right vertical axis). Figure 5.11 illustrates particle size and shape properties for two exemplary experiments, namely Exp 1 and Exp 2 in Section 5.4.1.2: in the upper part of Figure 5.10 the PSSDs of the crystal ensemble as measured using μ -DISCO before cooling (pink contour lines and shade) and thereafter (gray) are illustrated; in the lower part of the same figure the two final PSSDs are illustrated as blue contour lines.

By inspection of Figure 5.11, it is apparent that the final crystals are more elongated, with a broader distribution in the L_1 direction than the initial crystals. This is confirmed by the initial and final values of $L_{1,N}$ and of $\sigma_{1,N}$ in Figure 5.10: both quantities increase significantly during cooling because of growth, obviously, and because of broadening of the distribution. The latter effect is much less obvious, and might require a more in-depth study for a sound physically based characterization. In the scope of this work, we have decided to describe such effect via a growth model, where the growth

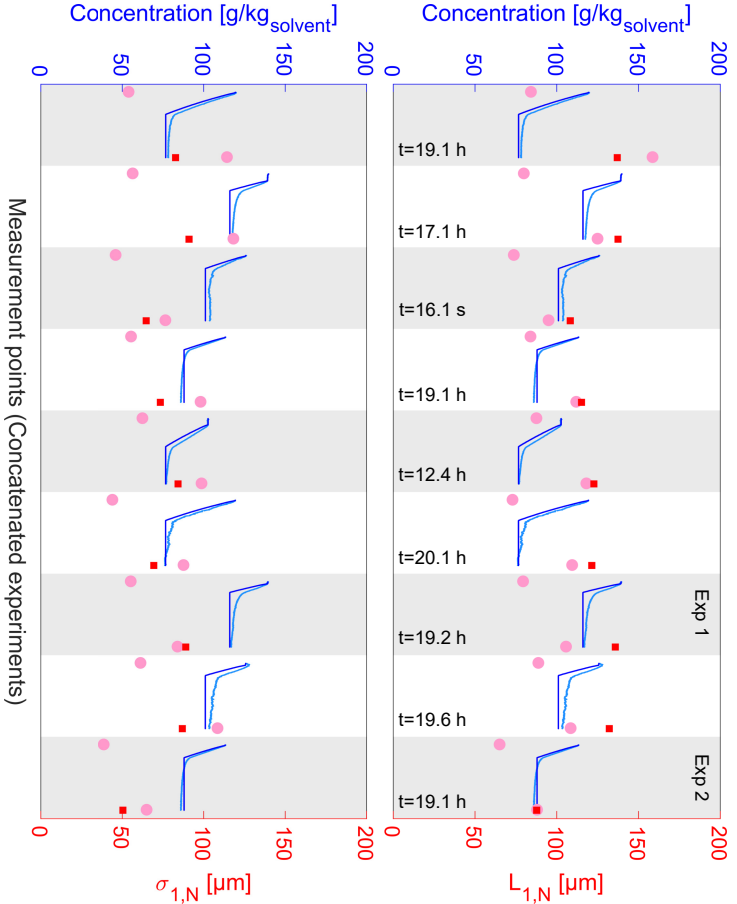


FIGURE 5.10: Results of the fitting aimed at estimating the growth kinetics for γ -D-Mannitol starting from the cooling stages carried out during the factorial experiments. The light blue markers correspond to the measured concentration profile, while the pink circles correspond to the number-weighted average $L_{1,N}$ (upper panel) and $\sigma_{1,N}$ (lower panel) at the beginning and end of each stage. The dark blue line and the red squares represent the fitted concentration and $L_{1,N}$ and $\sigma_{1,N}$ respectively. For each stage, the corresponding duration of the experiment is reported.

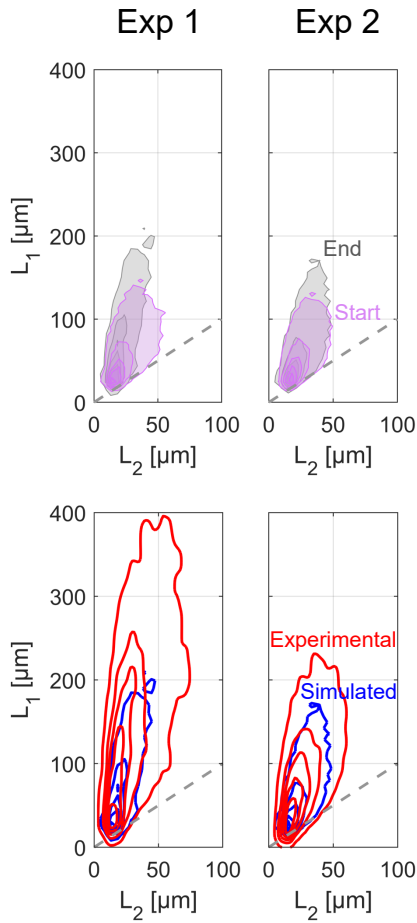


FIGURE 5.11: In the first row, the particle size and shape distributions collected at the beginning (pink) and at the end (gray) of two cooling stages are shown, highlighting the increased broadness of the final PSSD in comparison to the original one. On the second row, a comparison between the PSSD at the end of the cooling stage, both measured (blue) and simulated (red), is carried out, showing the agreement between model and experiments.

rate in the L_1 dimension is size-dependent: the functional form is known to be able to account for a broadening of the distribution (see for instance the characterization of β L-Glutamic growth reported earlier⁷⁷).

In this work we propose the following constitutive equations for the growth rate in the two directions as a function of supersaturation, temperature and dimension L_1 (depending on seven parameters):

$$G_1 = p_{11} \exp\left(-\frac{p_{12}}{T}\right) (S-1)^{p_{13}} \left(1 - \exp\left(-p_{14} \frac{L_1}{L_{\text{ref}}}\right)\right) \quad (5.33)$$

$$G_2 = p_{21} \exp\left(-\frac{p_{22}}{T}\right) (S-1)^{p_{23}} \quad (5.34)$$

It turns out that the nine experiments available are not sufficient to estimate all seven parameters without a strong correlation among them. We have therefore simplified the previous equations: by neglecting the explicit dependence on temperature, i.e. by setting $p_{12} = p_{22} = 0$ (note that the equations are still temperature-dependent through the definition of supersaturation in Equation 5.7); by assuming linear dependence on the supersaturation driving force, i.e. by setting $p_{13} = p_{23} = 1$ and by choosing $L_{\text{ref}} = 1000 \mu\text{m}$. The resulting simplified equations depending only on three parameters, namely p_{11} , p_{14} , and p_{21} , are:

$$G_1 = p_{11}(S-1) \left(1 - \exp\left(-p_{14} \frac{L_1}{L_{\text{ref}}}\right)\right) \quad (5.35)$$

$$G_2 = p_{21}(S-1) \quad (5.36)$$

The three parameters have been estimated by matching simulations and experiments as well as possible in terms of five pieces of information for each cooling stage, namely the concentration profile over time, and the average sizes and variances (in both L_1 and L_2 directions) of the final PSSD (note all simulations have been started with an ensemble of crystals having exactly the same PSSD as that measured). The estimated parameters are reported in Table 5.8, together with their 95% confidence intervals. The simulated results are shown in Figures 5.10 and 5.11 together with the experimental measurements for the sake of comparison: simulated dark blue concentration profiles are plotted in Figure 5.10; red squares represent the final $L_{1,N}$ and $\sigma_{1,N}$ in the upper and lower panel, respectively, of Figure 5.10; the red contour lines in the lower part of Figure 5.10 illustrate the simulated final PSSDs for experiments Exp 1 and Exp 2.

While we are fully aware that the agreement between simulations and measurements is not perfect, we would argue that it is reasonably good

Parameter values and 95% confidence intervals	
Parameter	Estimated value
$p_{11} \left[\frac{\mu\text{m}}{\text{s}} \right]$	30.2 ± 1.5
$p_{14} [-]$	0.81 ± 0.04
$p_{21} \left[\frac{\mu\text{m}}{\text{s}} \right]$	0.20 ± 0.03

TABLE 5.8: Estimated values of the kinetic parameters and their confidence intervals.

(average absolute error of $15 \mu\text{m}$ for L_1 and $5 \mu\text{m}$ for L_2), since all main trends are properly captured. More specifically, we consider the estimated growth rates as sufficient to provide a reasonable estimate of the ratio G_1/G_2 , whose importance in the context of the 3-stage process has been demonstrated above. Considering the size dependence of G_1 and assuming L_1 varying between $100 \mu\text{m}$ and $300 \mu\text{m}$ yield a value of G_1/G_2 from Equations 5.35 and 5.36 between about 15 and about 40. This is a much larger value than in the case of β L-Glutamic acid, which leads to the conjecture that the γ D-Mannitol system behaves similar to the system in the bottom left corner of Figure 5.1, i.e. a system characterized by a large value of both G_1/G_2 and D_1/D_2 .

5.4.2 From the attainable region to process design

Based on the type of attainable region obtained, it is possible to heuristically optimize the operating conditions that should eventually be applied when the 3-stage process is implemented.

In the case of low G_1/G_2 and high D_1/D_2 ratios (bottom right corner of Figure 5.1), as in the case of β L-Glutamic acid, the process can actually lead to a wide variety of sizes and shapes. As shown elsewhere,^{34,36} a good compromise between the improved crystal morphology and the productivity of the process is represented by heuristically optimal conditions, where a moderate milling intensity is combined with a large number of cycles.

On the other hand, for high G_1/G_2 and low D_1/D_2 ratios (top left corner of Figure 5.1), the best operating conditions correspond to the minimum number of cycles and the highest milling intensity. This choice provides a compromise between productivity, number of fines in the product, and morphology of the crystals at the end of the process.

For situations similar to the case of γ D-Mannitol, the heuristically optimal operating conditions correspond to a high milling intensity, with the aim of improving particle morphology, and an intermediate (3 to 4) number of cycles, to remove the fines formed during breakage.

It is important to notice that the strategy proposed is based only on the outcome of the four factorial experiments and does not require any mathematical model, thus reducing the characterization effort to a minimum.

5.4.3 *Exploration of the process design space*

The attainable regions shown for γ D-Mannitol and β L-Glutamic acid have been obtained by varying the rotor speed and the number of cycles. It is clear that this covers only a subset of the whole design space characteristic of the 3-stage process and is therefore necessary to understand if and how varying the other operating conditions can change the type of attainable region obtained.

In particular, another operating parameter that can be varied is the fraction of mass dissolved.^{34,36} In order to investigate its effect on the attainable region for different compounds, some considerations can be made considering the compound-specific properties, as well as the simulation results. We start by considering the case of large D_1/D_2 and small G_1/G_2 ratios (bottom right corner of Figure 5.1). For this type of compounds, increasing the fraction of mass dissolved has a beneficial effect, since more crystal mass would be removed during dissolution, making the particles shorter, and solute would be recovered during cooling by growth along L_2 , thus obtaining more compact crystals (see panel (b) of Figure 5.2). In this case, the shape of the attainable region does not change, but different sizes can be achieved. The same situation occurs for compounds with small D_1/D_2 and large G_1/G_2 ratios (top left corner of Figure 5.1).

Less intuitive are the two remaining cases, that is compounds with small (large) D_1/D_2 and small (large) G_1/G_2 ratios, for which the model can indeed be used to gain a better insight. Figure 5.12 shows the effect of increasing the fraction of mass dissolved for two of these intermediate cases. It is readily observed that changing this operating condition does indeed change the shape of the attainable region, but leads to product particles with a worse morphology. Further, increasing the fraction of mass dissolved leads to particles with a more equant shape only if the change in length L_1 of the crystals during the crystallization step is smaller than its reduction during the dissolution stage.

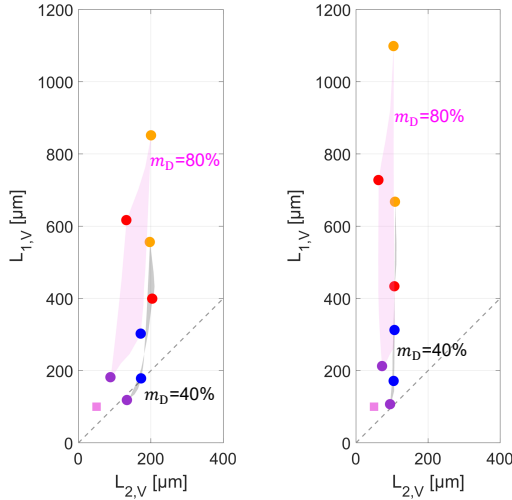


FIGURE 5.12: Simulations aimed at investigating the effect of the fraction mass dissolved on the attainable region of the 3-stage process (left panel: $G_1/G_2=1.5$ and $D_1/D_2=0.2$; right panel: $G_1/G_2=12$ and $D_1/D_2=1.9$).

For a more in-depth investigation of the effect of changing the mass dissolved during the heating steps on the PSSD of the product crystals, one can use the model that we have developed in Section 5.4.1.4 for γ D-Mannitol. Such model would be applied beyond the scope of the experiments used to estimate its model parameters, namely to study the effect of changing m_D based on fitting experiments carried out all with the same value of m_D . In order to check whether this is possible, we have carried out one 3-stage process experiment under the same conditions as run M5 in Table 5.7, but with 50% of mass dissolved during the dissolution stages instead of 20% only. The results of such experiments are illustrated in Figure 5.13, where the left-hand side shows the initial (pink contour lines and shade) and final (gray) PSSDs measured with the μ -DISCO and the right-hand side shows the measured (blue) and the calculated (red) final PSSDs. It is readily observed that the agreement between simulation result and experimental measure is acceptable, i.e. similar to the error observed in the case of the cooling experiments used to estimate the growth model parameters. We consider this result very encouraging, because it demonstrates the possibility of efficiently exploring the design space of the 3-stage process.

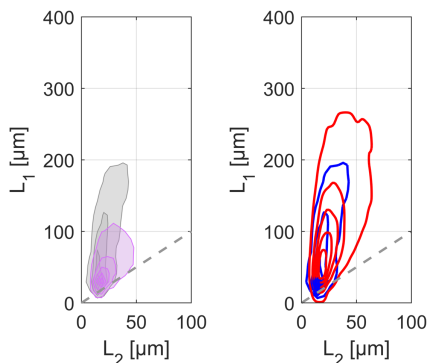


FIGURE 5.13: Results of the experiment performed adopting the operating conditions reported in Tables 5.6 and 5.7 for experiment M5 dissolving 50% of the mass suspended. In the left panel, the particle size and shape distributions collected at the beginning (pink) and at the end (gray) of two cooling stages are shown. In the right panel, the comparison between simulation (red) and experimental (blue) results is reported.

5.5 CONCLUSIONS

The 3-stage process certainly represents a valid approach to manipulate the size and shape of crystals, but its shortcomings, particularly concerning the very broad design space and its characterization when applied to different compounds, question its applicability. In this work we tackled these problems by developing a robust and effective approach to characterize the 3-stage process feasibility and potential for different compounds with a contained characterization effort.

First, we used the model to determine generally valid compound-dependent features. In particular, the attainable region, which is the portion of the L_1L_2 -plane corresponding to all the possible process outcomes, has been identified through process simulations performed with different growth and dissolution kinetics. This analysis allowed to pinpoint, as key characteristics of the system, the growth and dissolution rates ratios, which strongly affect the type and shape of the attainable region. These simulations were used to define a small set of experiments to fully identify the attainable region without performing a comprehensive and time demanding process characterization.

The strategy developed has therefore been applied to experimentally investigate the outcome of the 3-stage process when applied to two different compounds, namely β L-Glutamic acid and γ D-Mannitol. The results validated the observation obtained through simulations and confirmed the developed model-free approach as a valid tool for an efficient process characterization. We then used the experimental data acquired throughout the factorial experiments to estimate the growth kinetics of γ D-Mannitol and compare the behavior of both model compounds.

The experiments have been combined with the information acquired via process simulations in order to define, for each type of attainable region, heuristic optimal conditions granting the best compromise between productivity and crystal shape. Finally, the experimental data are used to tune the model parameters and run simulations to explore the whole design space and predict the properties of the 3-stage process products.

The main strength of the proposed approach lies in its general validity, as it is not necessary to fully characterize the system to quantify the outcome of the 3-stage process, but only a limited set of tests, namely the four factorial experiments, can be used to this aim. This is particularly interesting given the reduced amount of material and effort required to carry out the tests. Analyzing different compounds also allowed to experimentally observe the different attainable region obtained via simulations. Based on the type of attainable region, general heuristic optimal conditions have been defined, which are mainly based on common properties of the final size and shape of the crystals and not on the specific features of the system. This is of great relevance, as it is possible to apply the identified conditions merely according to the type of attainable region obtained, thus saving a time demanding process optimization for each compound investigated. Furthermore, gaining access to the information throughout each stage showed how a deeper insight in different aspects of the 3-stage process and the system can be achieved without further characterization effort, especially when this information is combined with the model. In this case, the effect of different operating conditions, once the kinetics of the system have been estimated, can be investigated *in-silico*, thus leading to the possibility of greatly enlarging and exploring the process design space without performing time-consuming and expensive experiments, a possibility certainly valuable for research and development purposes.

5.6 NOTATION

B	birth term in the PBE	$[\mu\text{m}^{-2} \text{kg}^{-1} \text{s}^{-1}]$
c	solute concentration in the liquid phase	$[\text{g kg}^{-1}]$
c_0	initial solute concentration in the liquid phase	$[\text{g kg}^{-1}]$
c^*	solubility	$[\text{g kg}^{-1}]$
C	number of cycles	$[-]$
D_i	dissolution rate for dimension i	$[\mu\text{m s}^{-1}]$
E	death term in the PBE	$[\mu\text{m}^{-2} \text{kg}^{-1} \text{s}^{-1}]$
F	objective function	$[-]$
g_i	daughter distribution of the fragments along the i -th dimension	$[\mu\text{m}^{-1}]$
\mathbf{G}	vector of rates of change	$[\mu\text{m s}^{-1}]$
G_i	growth rate for dimension i	$[\mu\text{m s}^{-1}]$
J_N	nucleation rate	$[\text{kg}^{-1}\text{s}^{-1}]$
J_S	secondary nucleation rate	$[\text{kg}^{-1}\text{s}^{-1}]$
J_{He}	heterogeneous primary nucleation rate	$[\text{kg}^{-1}\text{s}^{-1}]$
J_{Ho}	homogeneous primary nucleation rate	$[\text{kg}^{-1}\text{s}^{-1}]$
\mathbf{k}_D	vector of dissolution rate parameters	[varies]
\mathbf{k}_G	vector of growth rate parameters	[varies]
\mathbf{k}_{Hom}	vector of homogeneous nucleation rate parameters	[varies]
\mathbf{k}_{Het}	vector of heterogeneous nucleation rate parameters	[varies]
\mathbf{K}_i	vector of breakage frequency parameters	[varies]
k_v	shape factor	$[-]$
K_i	breakage frequency for dimension i	$[\text{s}^{-1}]$

L_i	crystals characteristic dimension i	[μm]
$L_{i,N}$	number-weighted average characteristic dimension i	[μm]
$L_{i,V}$	volume-weighted average characteristic dimension i	[μm]
m_0	mass of seeds per kg of solvents	[g/kg]
m_D	percentage of mass dissolved	[-]
m_M	mass of the rotor	[g]
n	number density function	[$\mu\text{m}^{-2} \text{kg}^{-1}$]
n_0	PSD of seed crystals	[$\mu\text{m}^{-2} \text{kg}^{-1}$]
n_C	number of process cycles	[-]
N_E	total number of experimental observations	[-]
N_O	number of considered outputs	[-]
N_P	power number	[-]
\mathbf{p}	vector of breakage rate parameters	[varies]
\mathbf{q}	vector of estimated growth rate parameters	[varies]
S	supersaturation	[-]
t	time	[s]
T	temperature	[$^{\circ}\text{C}$]
T_0	initial process temperature	[$^{\circ}\text{C}$]
T_F	final process temperature	[$^{\circ}\text{C}$]
x	size of the mother particle during a breakage event	[μm]
y_i	characteristic property of the measured particle size and shape distribution for the i -th experiment	[μm]
γ_C	cooling rate	[$^{\circ}\text{C} \text{min}^{-1}$]
γ_D	heating rate	[$^{\circ}\text{C} \text{min}^{-1}$]
ϵ	power input	[W kg^{-1}]

Φ	aspect ratio	[-]
μ_{ij}	cross moment ij of the PSSD	[varies]
ρ	density of the crystalline phase	[kg m ⁻³]
$\sigma_{1,N}$	number-weighted standard deviation in L_1 direction	[μm]
$\sigma_{2,N}$	number-weighted standard deviation in L_2 direction	[μm]
τ	residence time in the mill	[s]
θ	rotor speed	[rps]

CONCLUDING REMARKS AND OUTLOOK

Given the relevance of industrial crystallization, it only came naturally for academic researchers to delve into every aspect of this separation process. Their interest ranged from the structure of the crystalline lattice to the development of efficient processes and pieces of equipment. To this aim, several measurement tools have been developed, to investigate all the details required for a comprehensive understanding of all the phenomena. A plethora of crystallization processes have also been designed to produce particles with the desired size and shape. Nevertheless, controlling the shape of crystals still remains an open question in the crystallization community, with different branches of research tackling the problem from different perspectives.

In this thesis, the use of mechanical action has been investigated as a possible approach for the selective manipulation of crystal morphology. In particular, a new process integrating a milling and a dissolution step in the crystallization pipeline has been proposed as a novel solution for the selective manipulation of crystal size and shape. The 3-stage process certainly proved to be a viable alternative to attain crystals characterized by a more equant morphology, in comparison to more traditional processes currently exploited in the industry. The comprehensive investigation of the design space characteristic of this process is however inherently difficult, due to the large amount of degrees of freedom corresponding to the plethora of operating variables. Therefore, a bottom-up approach has been used in the beginning to develop a shortcut procedure to fully characterize the system. Nevertheless, as it is currently designed and characterized, the 3-stage process can still experience improvements ranging from the characterization techniques used to the operation itself.

In this chapter, we provide final remarks on the most relevant findings presented in this work, as well as a possible outlook in light of the continued effort put in the development of imaging devices and process design.

6.1 IMAGING TECHNIQUES AND PARTICLE ENSEMBLE MODELING

The use of imaging techniques for the reconstruction of the 3D structure of measured particles is a vital tool for the investigation of the morphology of crystals. Currently, a very limited amount of commercially available devices considers the real habit of crystals when characterizing their size. It is in this framework that the μ -DISCO, presented in Chapter 1, stems out as a unique instrument, capable of providing an insight otherwise not accessible. In particular, it has been shown that this novel instrument, with its improved optics, background removal, and statistical contour matching from stereoscopic images, paves the way towards more accurate characterization of particle size and shape. Thus, this measurement device is the perfect candidate for the quantification of changes in the particle morphology in crystallization processes. Yet, some improvements can be achieved both in the hardware and the software.

First, in order to perform on-line measurements also with very high suspension densities, an automated dilution loop, where the suspension is sampled from the crystallizer, diluted with pure solvent, and subsequently concentrated and sent back to the vessel, is necessary. Concerning the hardware, one or more cameras could be added in order to improve the reconstruction of the visual hull, thus making more accurate the estimation of the sizes of the measured particles. Another possibility could be the use of a different type of camera, with a different magnification and resolution, for the detection and measurement of fine particles, an aspect particularly important for the study of attrition and nucleation. The change made to the optical components, however, would bring only a marginal betterment compared to that achievable by improving the software component of this measurement tool. It is certainly in this area that the μ -DISCO can exploit the algorithms and techniques already applied in machine learning and computer vision. For example, the foreground extraction, the possibility of tracking particle motion for the acquisition of more images of the same crystals are some of the routines that are currently successfully implemented in other fields and of which the μ -DISCO would greatly benefit.

Strictly related to the imaging techniques, the models for crystals should also be updated. Currently, the number of particle shape classes used by the μ -DISCO and the quality of the image collected does not allow for a level of detail such that complex-shaped particle morphologies can be always accurately characterized. This would be of great interest for the development of models capable of predicting specific properties of a tablet,

such as the dissolution rates in the human body, using the quantitative information on the area of each specific facet exposed by the crystals. However, the use of morphological population balance equations faces two major challenges. The first one concerns the development of robust and precise algorithms for the solution of these problems, which is still an on-going topic of research. The second challenge concerns their implementation in the industrial practice, mainly due to the lack of off-the-shelf measurement instruments for product characterization, which can provide the required information on particle size and shape. Nevertheless, these models are still a vital tool, both during the stages of process design and development and for the understanding of the basic phenomena underlying the different unit operations.

6.2 BREAKAGE OF NEEDLE-LIKE PARTICLES

In Chapter 2 a comprehensive characterization of the milling device and stage that is used in the 3-stage process has been presented. In particular, first a mathematical model, whose constitutive equations are based on a combination of the empirical evidence and the underlying physics of the breakage events, has been developed. Therefore, a series of tests have been performed aimed at investigating the repeatability and reproducibility, as well as the effect of different operating conditions on the final products. The kinetic parameters have been fitted to demonstrate the suitability of the model for the quantitative description and prediction of the outcome of a milling process where a continuous rotor-stator wet milling device is used.

The model developed can certainly be improved, by carrying out specific activities aimed at generalizing its formulation and applicability. For example, the terms in its constitutive equations can be recast in order to extend the model to different types of milling devices (i.e. ball mills, roll mills). In particular, the term taking into account the operating conditions should be tailored to consider the mechanics of the breakage event, i.e. how and where the force is applied. Furthermore, indentation hardness tests can be performed on single crystals of different compounds in order to estimate their hardness to deformation and correlate this intrinsic property to the breakage kinetics. Particularly interesting would also be the possibility of developing an experimental protocol for the identification and quantification of the correct functional form for the daughter distribution.

6.3 IMPROVEMENTS FOR THE 3-STAGE PROCESS

In Chapters 3 and 4 the potential of the 3-stage process has been assessed both through simulations and experiments. In particular, first the feasibility of the process through simulations has been shown. Therefore we performed an in-silico sensitivity analysis on process operating conditions to thoroughly characterize their effect on the final properties of the crystals and to identify general, characteristic trends. A set of dedicated experiments has been designed based on the observation collected through simulations to assess the trends simulated. The process proved to effectively manipulate the morphology of the crystals. Hence, we combined the simulated and experimental observation to identify an heuristic optimum experiment, which would allow to obtain products with close-to-optimal properties. The crystals obtained at the end of such experiment have been compared with those obtained at the end of a cooling crystallization step both with and without milling, highlighting the strong improvement achieved in terms of particle size and shape when the 3-stage process is performed. Nevertheless, the process could be further improved in order to overcome some of its drawbacks.

The heating stage, as it is designed now, dissolves indiscriminately the fine particles and the coarser crystals, since the whole suspension is heated in the vessel. This problem can be tackled in different ways. A first solution could be splitting the ground suspension into two parts, each containing a specific percentage of the mass of crystals suspended. The dissolution stage is then performed only on one of the two new suspensions, such that its outcome is a clear solution which is then added to the fraction that was not treated, recovering hence the supersaturation by growth. However, with this approach, fines would still be present and would consequently grow in the suspension that is not treated, potentially leading to products with significant variability in their size. Therefore a second process alternative relies on selectively separate the fines in a dedicated stage, such as an hydrocyclone or by flotation.

From the process point of view, the choice of splitting the temperature drop from the beginning to the end of the process only according to the number of cycles could potentially lead to very high supersaturations in the first cycles, where a small amount of crystal mass is available to recover the excess of solute thus leading to a large number of undesired nucleation events, and low supersaturations in the last cycles, where the opposite situation occurs. Therefore, this parameter should be considered to define

the final temperature of each cooling stage. Furthermore, the choice of keeping all the operating conditions constant throughout the cycles limits the process outcome. For example, the rotor speed could be reduced from cycle to cycle so to avoid extensive breakage along L_2 towards the end of the process, thus improving product morphology. Obviously, removing this constraint would greatly improve the variety of sizes and shapes achievable, but at the price of expanding the design space and requiring a huge effort to investigate experimentally.

6.4 PROCESS CHARACTERIZATION

The identification of the attainable region of the 3-stage process, as investigated in Chapter 5, represents one of the biggest challenges, especially in terms of trade-off between number of experiments performed and information required. In particular, in this chapter it has been shown how, by applying the factorial design approach, it is possible to identify a limited set of experiments which allows to characterize the variety of process outcome under different operating conditions. A sensitivity analysis on the kinetic parameters appearing in the constitutive equations of the model has been performed to investigate in-silico the effect of different compound properties on the 3-stage process outcome. The results have been assessed by carrying out two sets of experiments on two different compounds. Furthermore, it has been proven that, given the amount of information inherently contained in the different cycles, it is possible to further characterize the process, if needed, by estimating also the characteristic kinetics and thus proceed with process optimization.

If on the one hand the approach proposed is robust and extremely helpful, on the other it is clear that non-linear effects can not be quantified based only on the outcome of the four experiments identified with the factorial design. Furthermore, the problem of process characterization becomes harder to tackle when removing some of the assumptions on the operating conditions, thus significantly enlarging the design space and hence the number of experiments required. Using the model reported in Chapter 2 could certainly help, as it would avoid time consuming laboratory experiments for the 3-stage process, but it would need dedicated tests to quantify the kinetic parameters, as they strongly impact the process outcome. A thorough characterization as that performed in Chapter 2 would require a large number of experiments, without giving any insight on the process outcome. Therefore, it would be more useful to gain an understanding

of basic properties, i.e. growth rates and dissolution rates ratios, which are effectively determining the final outcome of the cycles, as shown in Chapter 5, with simple experiments. One idea would be to measure the behavior of single crystals and obtain the quantities of interest from these experiments. Even though the sample might be statistically irrelevant, from growth and dissolution experiments on single crystals a rough estimation of the kinetics is still possible and it would help in clarifying the type of attainable region characteristic of the compound investigated.

The factorial design still represents a valid alternative to identify the set of experiments required for a thorough characterization even when more than two operating conditions have to be explored, but their number exponentially increases with the number of process variables. Therefore, the factorial design approach can be coupled with an optimization algorithm to identify in real-time, based on the previous tests, the set of experiments that should be performed next and simultaneously identify optimal operating conditions. The use of population balance equations in the optimization routine is not advised, due to large effort required by the experiments used to fit the kinetics of the model. A more promising approach is based on black-box models, such as artificial neural networks,^{120,121} where, provided a set of inputs, an output is generated without any knowledge of the nature of the problem. The main advantage is that this type of models does not require a deep understanding of the basic phenomena, but has the drawback of requiring a robust experimental data-set to train the algorithm.

The combination of mathematical modeling and factorial design allows to avoid the investigation of operating conditions leading to products not fulfilling the imposed specifications and therefore to reduce the number of experiments to be performed by ruling out those not providing significant information. Despite not being the optimal approach, this technique certainly represent a good starting point to further develop new alternatives.

6.5 3-STAGE PROCESS CONTROL

In the framework of further improving of the 3-stage process, the possibility of performing path planning to determine the sequence of stages and the corresponding operating conditions necessary to reach the desired target is also of relevant interest. This has been proven to be possible, through simulations, in the case of pure temperature cycles,⁷¹ but its feasibility in laboratory experiments still has to be assessed. Despite the intrinsic difficulty of the problem, the approach has been already successfully been

implemented in the case of more complex processes.^{122,123} While it is clear that a detailed model is required to successfully accomplish these tasks, a sensitivity analysis on the kinetics, similar to that reported in Chapter 5, might be useful to identify generally valid trends based on specific group of properties that holds for different compounds.

Model-free control is also certainly appealing when it comes to its application to the 3-stage process. The main challenge actually lies in controlling the milling stage, given its short characteristic time. A workaround to this problem consists in milling only a small fraction of the suspension, so to measure the resulting products and subsequently adapt the operating conditions to obtain the desired final properties. Concerning the control of the crystallization and dissolution stage, experimental works have been published^{71,90,124-126} showing a successful model-free controller capable of adjusting the operating conditions to achieve the desired shape and sizes. The main difficulty might however lie in performing on-line measurements with the μ -DISCO in its current configuration, unless the dissolution loop mentioned in Section 6.1 is developed and implemented.

6.6 INDUSTRIAL PERSPECTIVE

In light of all the results shown in this thesis, the 3-stage process certainly represents an interesting alternative for the selective manipulation of particle size and shape, especially in the case where no additives or different solvents can be used. Nevertheless, some issues need to be solved in order to eventually implement this process at the industrial scale.

As highlighted in Chapters 3 and 4, the productivity of the active pharmaceutical ingredient, defined as the amount of compound recovered in the solid phase per process time, significantly drops in the case of the 3-stage process. This is due to the introduction of the dissolution and milling stages, which increases the total process time. In this framework, it would be of interest trying to combine the dissolution and the milling stage. Since the characteristic time of dissolution is in the order of minutes, a controlled increment of temperature of the suspension in the mill could be exploited to let dissolution occur during breakage, at least partially. Furthermore, it is necessary to also quantify, for a better estimation of the productivity, the process time of all the downstream unit operations. It is only with this complete picture in mind, that a decision concerning the implementation of the 3-stage process can be made.

According to its current design, the 3-stage process would require two batch crystallizers, a plant configuration that certainly increases the risk of batch-to-batch variability. The problem can be solved by moving towards continuous manufacturing, a topic of current relevance especially in the pharmaceutical industry, with the added benefit of the quality-by-design of the products, but possible drawbacks linked to the difficulties faced when moving from batch to continuous production.^{127,128} Furthermore, in the framework of energy efficient processes, it is necessary to investigate more in detail the energy consumption of the different stages, eventually coupling the dissolution and crystallization stages to recover the largest amount of heat available.

BIBLIOGRAPHY

1. Green, D. W. & Perry, R. H. *Perry's chemical engineers' handbook* 8th ed. (ed Green, D. W.) (McGraw-Hill, 2008).
2. Burt, H. M. & Mitchell, A. G. Effect of habit modification on dissolution rate. *Int. J. Pharm.* **5**, 239 (1980).
3. Chow, K., Go, J., Mehdizadeh, M. & Grant, D. Modification of adipic acid crystals: influence of growth in the presence of fatty acid additives on crystal properties. *Int. J. Pharm.* **20**, 3 (1984).
4. Rasenack, N., Mu, B. W. & Kiel, D. Crystal habit and tableting behavior of paracetamol and Ibuprofen. *Int. J. Pharm.* **244**, 45 (2002).
5. Patel, S., Kaushal, A. M. & Bansal, A. K. Compression Physics in the Formulation Development of Tablets. *Crit. Rev. Ther. Drug Carr. Syst.* **23**, 1 (2006).
6. Acevedo, D., Kamaraju, V. K., Glennon, B. & Nagy, Z. K. Modeling and Characterization of an in Situ Wet Mill Operation. *Org. Process Res. Dev.* **21**, 1069 (2017).
7. Szilágyi, B. & Nagy, Z. K. Population Balance Modeling and Optimization of an Integrated Batch Crystallizer–Wet Mill System for Crystal Size Distribution Control. *Cryst. Growth Des.* acs.cgd.7b01331 (2018).
8. Yang, G., Kubota, N., Sha, Z., Louhi-Kultanen, M. & Wang, J. Crystal shape control by manipulating supersaturation in batch cooling crystallization. *Cryst. Growth Des.* **6**, 2799 (2006).
9. Kwon, J. S.-I., Nayhouse, M., Christofides, P. D. & Orkoulas, G. Droplet microfluidics on a planar surface. *AIChE J.* **59**, 2317 (2013).
10. Yang, Y., Ma, C. Y. & Wang, X. Z. *Optimisation and closed-loop control of crystal shape distribution in seeded cooling crystallisation of L-Glutamic acid PART 1*, 216 (IFAC, 2012).
11. Majumder, A. & Nagy, Z. K. Prediction and control of crystal shape distribution in the presence of crystal growth modifiers. *Chem. Eng. Sci.* **101**, 593 (2013).

12. Constance, E. N., Mohammed, M., Mojibola, A., Egiefameh, M., Daodu, O., Clement, T., Ogundolie, T., Nwawulu, C. & Aslan, K. Effect of Additives on the Crystal Morphology of Amino Acids: A Theoretical and Experimental Study. *J. Phys. Chem. C* **120**, 14749 (2016).
13. Snyder, R. C., Veesler, S. & Doherty, M. F. The evolution of crystal shape during dissolution: Predictions and experiments. *Cryst. Growth Des.* **8**, 1100 (2008).
14. Jiang, M., Zhu, X., Molaro, M. C., Rasche, M. L., Zhang, H., Chadwick, K., Raimondo, D. M., Kim, K. K. K., Zhou, L., Zhu, Z., Wong, M. H., O'Grady, D., Hebrault, D., Tedesco, J. & Braatz, R. D. Modification of crystal shape through deep temperature cycling. *Ind. Eng. Chem. Res.* **53**, 5325 (2014).
15. Wu, Z., Yang, S. & Wu, W. Application of temperature cycling for crystal quality control during crystallization. *CrystEngComm* **18**, 2222 (2016).
16. Simone, E., Klapwijk, A. R., Wilson, C. C. & Nagy, Z. K. Investigation of the Evolution of Crystal Size and Shape during Temperature Cycling and in the Presence of a Polymeric Additive Using Combined Process Analytical Technologies. *Cryst. Growth Des.* **17**, 1695 (2017).
17. Deiner, L. J., Rottmayer, M. A. & Eigenbrodt, B. C. The effect of milling additives on powder properties and sintered body microstructure of NiO. *J. Adv. Ceram.* **4**, 142 (2015).
18. Bartos, C., Szabó-Révész, P., Bartos, C., Katona, G., Jójárt-Laczkovich, O. & Ambrus, R. The Effect of an Optimized Wet Milling Technology on the Crystallinity, Morphology and Dissolution Properties of Micro- and Nanonized Meloxicam. *Molecules* **21** (2016).
19. Smith, L. & Midha, P. Computer simulation of morphology and packing behaviour of irregular particles, for predicting apparent powder densities. *Comput. Mater. Sci.* **7**, 377 (1997).
20. Ma, C. Y., Wang, X. Z. & Roberts, K. J. Droplet microfluidics on a planar surface. *AIChE J.* **54**, 209 (2008).
21. Wan, J., Wang, X. Z. & Ma, C. Y. Particle Shape Manipulation and Optimization in Cooling Crystallization Involving Multiple Crystal Morphological Forms. *AIChE J.* **55**, 2049 (2009).
22. Grof, Z., Schoellhammer, C. M., Rajniak, P. & Stepanek, F. Computational and experimental investigation of needle-shaped crystal breakage. *Int. J. Pharm.* **407**, 12 (2011).

23. Schorsch, S., Ochsenbein, D. R., Vetter, T., Morari, M. & Mazzotti, M. High accuracy online measurement of multidimensional particle size distributions during crystallization. *Chem. Eng. Sci.* **105**, 155 (2014).
24. De Albuquerque, I., Ochsenbein, D. R., Mazzotti, M. & Morari, M. Effect of Needle-Like Crystal Shape on Measured Particle Size Distributions. *AIChE J.* **62**, 2974 (2016).
25. Friedman, N. & Russell, S. Image Segmentation in Video Sequences: A Probabilistic Approach. *Proc. Thirteen. Conf. Uncertain. Artif. Intell.* 175 (1997).
26. Benezeth, Y., Jodoin, P.-M., Emile, B., Laurent, H. & Rosenberger, C. Comparative study of background subtraction algorithms. *J. Electron. Imaging* **19**, 033003 (2010).
27. Haralick, R. M., Sternberg, S. R. & Zhuang, X. Image Analysis Using Mathematical Morphology. *IEEE Trans. Pattern Anal. Mach. Intell.* **9**, 532 (1987).
28. Suzuki, S. & Be, K. A. Topological structural analysis of digitized binary images by border following. *Comput. Vision, Graph. Image Process.* **30**, 32 (1985).
29. Bradski, G. *Learning OpenCV: Computer Vision with the OpenCV Library* 580 (2000).
30. Laurentini, A. The Visual Hull Concept for Silhouette-Based Image Understanding. *IEEE Trans. Pattern Anal. Mach. Intell.* **16**, 150 (1994).
31. Schneider, D. *Visual Hull*
32. Ochsenbein, D. R., Vetter, T., Morari, M. & Mazzotti, M. Agglomeration of Needle-like Crystals in Suspension. II. Modeling. *Cryst. Growth Des.* **15**, 4296 (2015).
33. Schorsch, S., Vetter, T. & Mazzotti, M. Measuring multidimensional particle size distributions during crystallization. *Chem. Eng. Sci.* **77**, 130 (2012).
34. Salvatori, F. & Mazzotti, M. Manipulation of Particle Morphology by Crystallization, Milling, and Heating Cycles - A Mathematical Modeling Approach. *Ind. Eng. Chem. Res.* **56**, 9188 (2017).
35. Salvatori, F. & Mazzotti, M. Experimental characterization and mathematical modeling of breakage of needle-like crystals in a continuous rotor-stator wet mill. *Submitt. Publ.*

36. Salvatori, F. & Mazzotti, M. Manipulation of particle morphology by crystallization, milling, and heating cycles - Experimental characterization. *Submitted*.
37. Salvatori, F., Binel, P. & Mazzotti, M. A robust and efficient strategy for the characterization of combined crystallization, milling, and dissolution stages. *Submitt. Publ.* (2018).
38. Wakeman, R. The influence of particle properties on filtration. *Sep. Purif. Technol.* **58**, 234 (2007).
39. Beck, R., Häkkinen, A., Malthe-Sørenssen, D. & Andreassen, J. P. The effect of crystallization conditions, crystal morphology and size on pressure filtration of L-glutamic acid and an aromatic amine. *Sep. Purif. Technol.* **66**, 549 (2009).
40. Perini, G., Salvatori, F., Ochsenbein, D. R., Mazzotti, M. & Vetter, T. Filterability prediction of needle-like crystals based on particle size and shape distribution data. *Submitted*.
41. Heng, J. Y. Y., Thielmann, F. & Williams, D. R. The effects of milling on the surface properties of form I paracetamol crystals. *Pharm. Res.* **23**, 1918 (2006).
42. Ho, R., Naderi, M., Heng, J. Y. Y., Williams, D. R., Thielmann, F., Bouza, P., Keith, A. R., Thiele, G. & Burnett, D. J. Effect of milling on particle shape and surface energy heterogeneity of needle-shaped crystals. *Pharm. Res.* **29**, 2806 (2012).
43. Hennart, S., Wildeboer, W., van Hee, P. & Meesters, G. Identification of the grinding mechanisms and their origin in a stirred ball mill using population balances. *Chem. Eng. Sci.* **64**, 4123 (2009).
44. Hennart, S., van Hee, P., Drouet, V., Domingues, M., Wildeboer, W. & Meesters, G. Characterization and modeling of a sub-micron milling process limited by agglomeration phenomena. *Chem. Eng. Sci.* **71**, 484 (2012).
45. Ramkrishna, D. *Population balances: Theory and applications to particulate systems in engineering* 355 (Academic press, 2000).
46. Briesen, H. Two-dimensional population balance modeling for shape dependent crystal attrition. *Chem. Eng. Sci.* **64**, 661 (2009).
47. Chakraborty, J. & Ramkrishna, D. Population Balance Modeling of Environment Dependent Breakage: Role of Granular Viscosity, Density and Compaction. Model Formulation and Similarity Analysis. *Ind. Eng. Chem. Res.* **50**, 13116 (2011).

48. Hill, P. J. Statistics of multiple particle breakage accounting for particle shape. *AIChE J.* **50**, 937 (2004).
49. Hill, P. J. Simulation of Spherical Particle Breakage. *Proc. 8th Int. Conf. Found. Comput. Process Des.* **34**, 333 (2014).
50. Borsos, Á. & Lakatos, B. G. Influence of breakage on crystal size distribution in a continuous cooling crystallizer. *Period. Polytech. Chem. Eng.* **56**, 65 (2012).
51. Rajagopalan, A. K., Schneeberger, J., Salvatori, F., Bötschi, S., Ochsenbein, D. R., Oswald, M. R., Pollefeys, M. & Mazzotti, M. A comprehensive shape analysis pipeline for stereoscopic measurements of particulate populations in suspension. *Powder Technol.* **321**, 479 (2017).
52. Doki, N., Yokota, M., Sasaki, S. & Kubota, N. Size Distribution of Needle-Shape Crystals of Monosodium L-Glutamate Obtained by Seeded Batch Cooling Crystallization. *J. Chem. Eng. Japan* **37**, 436 (2004).
53. Kumar, S. & Ramkrishna, D. On the solution of population balance equations by discretization - I. A fixed pivot technique. *Chem. Eng. Sci.* **51**, 1311 (1996).
54. Schöll, J., Bonalumi, D., Vicum, L., Mazzotti, M. & Müller, M. In Situ Monitoring and Modeling of the Solvent-Mediated Polymorphic Transformation of L -Glutamic Acid 2006. *Cryst. Growth Des.* **6**, 881 (2006).
55. Pertzoff, A. Solubility of Glutamic Acid in water and certain organic solvents. *J. Biol. Chem.* **C**, 97 (1932).
56. Cornel, J., Lindenberg, C. & Mazzotti, M. Experimental Characterization and Population Balance Modeling of the Polymorph Transformation of L -Glutamic Acid & DESIGN 2009. *Cryst. Growth Des.* **9**, 243 (2009).
57. Schönert, K. in *Adv. Miner. Process.* (ed Somasundaran, P.) 28 (SME/AIME, 1986).
58. Luciani, C. V., Conder, E. W. & Seibert, K. D. Modeling-aided scale-up of high-shear rotor-stator wet milling for pharmaceutical applications. *Org. Process Res. Dev.* **19**, 582 (2015).
59. Fawcett, T. An introduction to ROC analysis. *Pattern Recognit. Lett.* **27**, 861 (2006).

60. Kelemen, A., Szalay, A., Sovány, T. & Pintye-Hódi, K. Role of the particle size of sorbitol during the compression of common tablets and prediction of mini-tablet compression parameters. *Chem. Eng. Res. Des.* **104**, 814 (2015).
61. Bourcier, D., Féraud, J. P., Colson, D., Mandrick, K., Ode, D., Brackx, E. & Puel, F. Influence of particle size and shape properties on cake resistance and compressibility during pressure filtration. *Chem. Eng. Sci.* **144**, 176 (2016).
62. Horst, J. H., Geertman, R. M., Heijden, A. E. V. D. & Rosmalen, G. M. V. The influence of a solvent on the crystal morphology of RDX. *J. Cryst. Growth* **199**, 773 (1999).
63. Nokhodchi, A., Bolourchian, N. & Dinarvand, R. Crystal modification of phenytoin using different solvents and crystallization conditions. *Int. J. Pharm.* **250**, 85 (2003).
64. Thompson, C., Davies, M. C., Roberts, C. J., Tendler, S. J. B. & Wilkinson, M. J. The effects of additives on the growth and morphology of paracetamol (acetaminophen) crystals. *Int. J. Pharm.* **280**, 137 (2004).
65. Wen, H., Morris, K. R. & Park, K. Synergic effects of polymeric additives on dissolution and crystallization of acetaminophen. *Pharm. Res.* **25**, 349 (2008).
66. Salvalaglio, M., Vetter, T., Mazzotti, M. & Parrinello, M. Controlling and predicting crystal shapes: The case of urea. *Angew. Chemie - Int. Ed.* **52**, 13369 (2013).
67. Lovette, M. a., Muratore, M. & Doherty, M. F. Crystal shape modification through cycles of dissolution and growth: Attainable regions and experimental validation. *AIChE J.* **58**, 1465 (2012).
68. Jiang, M., Zhu, X., Molaro, M. C., Rasche, M. L., Zhang, H., Chadwick, K., Raimondo, D. M., Kim, K.-k. K., Zhou, L., Zhu, Z., Wong, M. H., Grady, D. O., Hebrault, D., Tedesco, J. & Braatz, R. D. Modification of Crystal Shape through Deep Temperature Cycling. *Ind. Eng. Chem. Res.* **53**, 5325 (2014).
69. Borchert, C., Nere, N., Ramkrishna, D., Voigt, A. & Sundmacher, K. On the prediction of crystal shape distributions in a steady-state continuous crystallizer. *Chem. Eng. Sci.* **64**, 686 (2009).
70. Eisenschmidt, H., Bajcinca, N. & Sundmacher, K. Optimal Control of Crystal Shapes in Batch Crystallization Experiments by Growth-Dissolution Cycles. *Cryst. Growth Des.* **16**, 3297 (2016).

71. Bötschi, S., Ochsenbein, D. R., Morari, M. & Mazzotti, M. Multi-Objective Path Planning for Single Crystal Size and Shape Modification. *Cryst. Growth Des.* **4873** (2017).
72. Kovačević, T., Reinhold, A. & Briesen, H. Identifying faceted crystal shape from three-dimensional tomography data. *Cryst. Growth Des.* **14**, 1666 (2014).
73. Ploss, R. & Mersmann, A. A New Model of the Effect of Stirring Intensity on the Rate of Secondary Nucleation. *Chem. Eng. Technol.* **12**, 137 (1989).
74. Kraume, M. *Mischen und Rühren: Grundlagen und moderne Verfahren* 1st (ed Kraume, M.) (Wiley-VCH, 2003).
75. Eisenschmidt, H., Voigt, A. & Sundmacher, K. Face-specific growth and dissolution kinetics of potassium dihydrogen phosphate crystals from batch crystallization experiments. *Cryst. Growth Des.* **15**, 219 (2015).
76. Schöll, J., Vicum, L., Müller, M. & Mazzotti, M. Precipitation of L-Glutamic Acid: Determination of Nucleation Kinetics. *Chem. Eng. Technol.* **29**, 257 (2006).
77. Ochsenbein, D. R., Schorsch, S., Vetter, T., Mazzotti, M. & Morari, M. Growth Rate Estimation of β L-Glutamic Acid from Online Measurements of Multidimensional Particle Size Distributions and Concentration. *Ind. Eng. Chem. Res.* **53**, 9136 (2014).
78. Gunawan, R., Fusman, I. & Braatz, R. D. High resolution algorithms for multidimensional population balance equations. *AIChE J.* **50**, 2738 (2004).
79. LeVeque, R. *Finite Volume Methods for Hyperbolic Problems*. Cambridge Univ. Press **54**, 258 (2002).
80. Pudasaini, N., Upadhyay, P. P., Parker, C. R., Hagen, S. U., Bond, A. D. & Rantanen, J. Downstream Processability of Crystal Habit-Modified Active Pharmaceutical Ingredient. *Org. Process Res. Dev.* **21**, 571 (2017).
81. Rasenack, N. & Müller, B. W. Ibuprofen crystals with optimized properties. *Int. J. Pharm.* **245**, 9 (2002).
82. Cashell, C., Corcoran, D. & Hodnett, B. K. Effect of Amino Acid Additives on the Crystallization of L -Glutamic Acid 2005. *Cryst. Growth Des.* **5**, 593 (2005).

83. Vetter, T., Mazzotti, M. & Brozio, J. Slowing the Growth Rate of Ibuprofen Crystals Using the Polymeric Additive Pluronic F127. *Cryst. Growth Des.* **11**, 3813 (2011).
84. Oucherif, K. A., Raina, S., Taylor, L. S. & Litster, J. D. Quantitative analysis of the inhibitory effect of HPMC on felodipine crystallization kinetics using population balance modeling. *CrystEngComm* **15**, 2165 (2013).
85. Liu, G., Hansen, T. B., Qu, H., Yang, M., Pajander, J. P., Rantanen, J. & Christensen, L. P. Crystallization of Piroxicam Solid Forms and the Effects of Additives. *Chem. Eng. Technol.* **37**, 1297 (2014).
86. Simone, E, Steele, G & Nagy, Z. K. Tailoring crystal shape and polymorphism using combinations of solvents and a structurally related additive. *CrystEngComm* **17**, 9370 (2015).
87. Klapwijk, A. R., Simone, E., Nagy, Z. K. & Wilson, C. C. Tuning Crystal Morphology of Succinic Acid Using a Polymer Additive. *Cryst. Growth Des.* **16**, 4349 (2016).
88. Borsos, A., Majumder, A. & Nagy, Z. K. Multi-Impurity Adsorption Model for Modeling Crystal Purity and Shape Evolution during Crystallization Processes in Impure Media. *Cryst. Growth Des.* **16**, 555 (2016).
89. Simone, E, Cenzato, M. V. & Nagy, Z. K. A study on the effect of the polymeric additive HPMC on morphology and polymorphism of ortho-aminobenzoic acid crystals. *J. Cryst. Growth* **446**, 50 (2016).
90. Eisenschmidt, H., Bajcinca, N. & Sundmacher, K. Optimal Control of Crystal Shapes in Batch Crystallization Experiments by Growth-Dissolution Cycles. *Cryst. Growth Des.* **16**, 3297 (2016).
91. Tanaka, Y., Inkyo, M., Yumoto, R., Nagai, J., Takano, M. & Nagata, S. Nanoparticulation of poorly water soluble drugs using a wet-mill process and physicochemical properties of the nanopowders. *Chem. Pharm. Bull. (Tokyo)*. **57**, 1050 (2009).
92. Patel, C. M., Murthy, Z. & Chakraborty, M. Effects of operating parameters on the production of barium sulfate nanoparticles in stirred media mill. *J. Ind. Eng. Chem.* **18**, 1450 (2012).

93. Kumar, D., Worku, Z. A., Gao, Y., Kamaraju, V. K., Glennon, B., Babu, R. P. & Healy, A. M. Comparison of wet milling and dry milling routes for ibuprofen pharmaceutical crystals and their impact on pharmaceutical and biopharmaceutical properties. *Powder Technol.* **330**, 228 (2018).
94. Kim, S., Wei, C. & Kiang, S. Crystallization Process Development of an Active Pharmaceutical Ingredient and Particle Engineering via the Use of Ultrasonics and Temperature Cycling. *Org. Process Res. Dev.* **7**, 997 (2003).
95. Hentschel, M. L. & Page, N. W. Selection of descriptors for particle shape characterization. *Part. Part. Syst. Charact.* **20**, 25 (2003).
96. Lee, J. R. J., Smith, M. L. & Smith, L. N. A new approach to the three-dimensional quantification of angularity using image analysis of the size and form of coarse aggregates. *Eng. Geol.* **91**, 254 (2007).
97. Gordon, M. S. Process considerations in reducing tablet friability and their effect on in vitro dissolution. *Drug Dev. Ind. Pharm.* **20**, 11 (1994).
98. Sun, C. & Grant, D. J. W. Influence of Crystal Shape on the Tableting Performance of L -Lysine Monohydrochloride Dihydrate. *Pharmacia* **90**, 569 (2001).
99. Nokhodchi, a, Amire, O & Jelvehgari, M. Physico-mechanical and dissolution behaviours of ibuprofen crystals crystallized in the presence of various additives. *J. Fac. Pharmacy, Tehran Univ. Med. Sci.* **18**, 74 (2010).
100. Sun, C. C. Decoding powder tableability: Roles of particle adhesion and plasticity. *J. Adhes. Sci. Technol.* **25**, 483 (2011).
101. Chatterjee, A., Gupta, M. M. & Birendra, S. Spherical crystallization: A technique use to reform solubility and flow property of active pharmaceutical ingredients. *Int. J. Pharm. Investig.* **7**, 4 (2017).
102. Liversidge, G. G. & Cundy, K. C. Particle size reduction for improvement of oral bioavailability of hydrophobic drugs: I. Absolute oral bioavailability of nanocrystalline danazol in beagle dogs. *Int. J. Pharm.* **125**, 91 (1995).
103. Chemburkar, S. R., Bauer, J., Deming, K., Spiwek, H., Patel, K., Morris, J., Henry, R., Spanton, S., Dziki, W., Porter, W., Quick, J., Bauer, P., Donaubaue, J., Narayanan, B. A., Soldani, M., Riley, D. & McFarland, K. Dealing with the impact of ritonavir polymorphs on the late stages of bulk drug process development. *Org. Process Res. Dev.* **4**, 413 (2000).

104. Singhal, D. & Curatolo, W. Drug polymorphism and dosage form design: A practical perspective. *Adv. Drug Deliv. Rev.* **56**, 335 (2004).
105. Bakalis, S., Le Révérend, B. J., Anwar, N. Z. R. & Fryer, P. J. Modelling crystal polymorphisms in chocolate processing. *Procedia Food Sci.* **1**, 340 (2011).
106. Khadka, P., Ro, J., Kim, H., Kim, I., Kim, J. T., Kim, H., Cho, J. M., Yun, G. & Lee, J. Pharmaceutical particle technologies: An approach to improve drug solubility, dissolution and bioavailability. *Asian J. Pharm. Sci.* **9**, 304 (2014).
107. Shangwal, K. *Additives and Crystallization Processes: From Fundamentals to Applications* (John Wiley & Sons, 2007).
108. Van Antwerpen, F. & van Krevelen, D. W. Influence of Crystallization Temperature, Molecular Weight, and Additives on the Crystallization Kinetics of Poly(ethylene Terephthalate). *J. Polym. Sci. Polym. Phys. Ed.* **10**, 2423 (1972).
109. Powell, K. A., Saleemi, A. N., Rielly, C. D. & Nagy, Z. K. Monitoring Continuous Crystallization of Paracetamol in the Presence of an Additive Using an Integrated PAT Array and Multivariate Methods. *Org. Process Res. Dev.* **20**, 626 (2016).
110. Taborga, P., Brito, I. & Graber, T. A. Effect of additives on size and shape of lithium carbonate crystals. *J. Cryst. Growth* **460**, 5 (2017).
111. Gupta, M. K., Vanwert, A. & Bogner, R. H. Formation of physically stable amorphous drugs by milling with neusilin. *J. Pharm. Sci.* **92**, 536 (2003).
112. Lin, S. Y., Hsu, C. H. & Ke, W. T. Solid-state transformation of different gabapentin polymorphs upon milling and co-milling. *Int. J. Pharm.* **396**, 83 (2010).
113. Tien, C., Bai, R. & Ramarao, B. V. Analysis of Effect Cake Growth in of Fine Particle Cake Filtration: Retention. *A.I.Ch.E. J.* **43**, 33 (1996).
114. Borchert, C. & Sundmacher, K. Morphology evolution of crystal populations: Modeling and observation analysis. *Chem. Eng. Sci.* **70**, 87 (2012).
115. Singh, M. R., Chakraborty, J., Nere, N., Tung, H. H., Bordawekar, S. & Ramkrishna, D. Image-analysis-based method for 3D crystal morphology measurement and polymorph identification using confocal microscopy. *Cryst. Growth Des.* **12**, 3735 (2012).

116. Kempkes, M., Vetter, T. & Mazzotti, M. Measurement of 3D particle size distributions by stereoscopic imaging. *Chem. Eng. Sci.* **65**, 1362 (2010).
117. Agimelen, O. S., Svoboda, V., Ahmed, B., Cardona, J., Dziewierz, J., Brown, C. J., McGlone, T., Cleary, A., Tachtatzis, C., Michie, C., Florence, A. J., Andonovic, I., Mulholland, A. J. & Sefcik, J. Multi-sensor inline measurements of crystal size and shape distributions during high shear wet milling of crystal slurries. *Adv. Powder Technol.* **1** (2018).
118. Cornel, J., Kidambi, P. & Mazzotti, M. Precipitation and transformation of the three polymorphs of d-mannitol. *Ind. Eng. Chem. Res.* **49**, 5854 (2010).
119. Bötschi, S., Rajagopalan, A. K., Morari, M. & Mazzotti, M. Estimation of Growth Kinetics for LGA. *Prep.*
120. Hoskins, J. & Himmelblau, D. Artificial neural network models of knowledge representation in chemical engineering. *Comput. Chem. Eng.* **12**, 881 (1988).
121. Murata, N., Yoshizawa, S. & Amari, S. I. Network Information Criterion—Determining the Number of Hidden Units for an Artificial Neural Network Model. *IEEE Trans. Neural Networks* **5**, 865 (1994).
122. Achenie, L. & Biegler, L. A superstructure based approach to chemical reactr network synthesis. *Comput. Chem. Eng.* **14**, 23 (1990).
123. Agarwal, A., Biegler, L. T. & Zitney, S. E. A Superstructure-Based Optimal Synthesis of PSA Cycles for Post-Combustion CO₂ Capture. *A.I.Ch.E. J.* **56**, 1813 (2010).
124. Saleemi, A. N., Rielly, C. D. & Nagy, Z. K. Comparative investigation of supersaturation and automated direct nucleation control of crystal size distributions using ATR-UV/vis spectroscopy and FBRM. *Cryst. Growth Des.* **12**, 1792 (2012).
125. Griffin, D. J., Kawajiri, Y., Rousseau, R. W. & Grover, M. A. Using MC plots for control of paracetamol crystallization. *Chem. Eng. Sci.* **164**, 344 (2017).
126. Rajagopalan, A. K., Bötschi, S., Morari, M. & Mazzotti, M. Feedback Control for the Size and Shape Evolution of Needle-like Crystals in Suspension. II. Cooling Crystallization Experiments. *Cryst. Growth Des.* (2018).

127. Zhang, D., Xu, S., Du, S., Wang, J. & Gong, J. Progress of Pharmaceutical Continuous Crystallization. *Engineering* 3, 354 (2017).
128. Chavan, R. B., Thipparaboina, R., Yadav, B. & Shastri, N. R. Continuous manufacturing of co-crystals : challenges and prospects. *Drug Deliv. Transl. Res.* 1 (2018).

CURRICULUM VITAE

PERSONAL DATA

Name	Fabio Salvatori
Date of Birth	January 5 th , 1989
Place of Birth	Codogno, Italy
Citizen of	Italy

EDUCATION

2013 – 2018	Eidgenössische Technische Hochschule, Zurich, Switzerland Doctoral Studies in the Separation Processes Laboratory
2011 – 2013	Politecnico di Milano, Milano, Italy Master Degree in Chemical Engineering
2008 – 2011	Politecnico di Milano, Milano, Italy Bachelor Degree in Chemical Engineering
2003 – 2008	Liceo Scientifico G. Novello Codogno, Italy High School Diploma (university entrance diploma)

PROFESSIONAL EXPERIENCE

2013 – 2018	Scientific assistant <i>Eidgenössische Technische Hochschule,</i> Zurich, Switzerland
2012 – 2013	Progetto 150 ore (scientific assistant) <i>Politecnico di Milano,</i> Milano, Italy

LIST OF REFEREED JOURNAL PUBLICATIONS

1. Salvatori F., Binel P., Mazzotti M., A robust and efficient strategy for the characterization of combined crystallization, milling, and dissolution stages, *Chemical Engineering Science X*, **2018**, *In press*.
2. Perini G., Salvatori F., Ochsenbein D.R., Mazzotti M., Vetter T., Filterability prediction of needle-like crystals based on particle size and shape distribution data, *Separation and Purification Technology*, **2018**, *211*, 768-781.
3. Salvatori F. and Mazzotti M., Manipulation of particle morphology by crystallization, milling, and heating cycles - Experimental characterization, *Industrial & Engineering Chemistry Research*, **2018**, *57* (45), 15522-15533.
4. Salvatori F. and Mazzotti M., Experimental characterization and mathematical modeling of breakage of needle-like crystals in a continuous rotor-stator wet mill, *Crystal Growth & Design*, **2018**, *18* (10), 5957-5972.
5. Rajagopalan A.K., Schneeberger J., Salvatori F., Bötschi S., Ochsenbein D.R., Oswald M.R., Pollefeys M., Mazzotti M., A comprehensive shape analysis pipeline for stereoscopic measurements of particulate populations in suspension, *Powder Technology*, **2017**, *321*, 479-493.
6. Salvatori F. and Mazzotti M., Manipulation of particle morphology by crystallization, milling, and heating cycles - A mathematical modeling approach, *Industrial & Engineering Chemistry Research*, **2017**, *56* (32), 9188-9201.
7. Ochsenbein D.R., Schorsch S., Salvatori F., Vetter T., Morari M., Mazzotti M., Modeling the facet growth rate dispersion of β l-glutamic acid — Combining single crystal experiments with nD particle size distribution data, *Chemical Engineering Science*, **2015**, *133*, 30-43.